Journal
International I J of Modern
M E
Engineering
ISSN: 1930-6628
www.ijme.us

INTERNATIONAL JOURNAL OF MODERN ENGINEERING

Fall/Winter 2017
Volume 18, No. 1

The Leading Journal of Engineering, Applied Science and Technology

Industrial

Electronics

Biomedical

Civil

Aerospace

Computer

Electrical

Chemical

Mechanical

ENGINEERING

THE LEADING JOURNAL OF ENGINEERING, APPLIED SCIENCE, AND TECHNOLOGY

Print ISSN: 2157-8052
Online ISSN: 1930-6628

www.ijme.us

www.iajc.org

INTERNATIONAL JOURNAL OF MODERN ENGINEERING

ABOUT IJME:

- IJME was established in 2000 and is the first and official flagship journal of the International Association of Journal and Conferences (IAJC).
- IJME is a high-quality, independent journal steered by a distinguished board of directors and supported by an international review board representing many well-known universities, colleges and corporations in the U.S. and abroad.
- IJME has an impact factor of **3.00**, placing it among the top 100 engineering journals worldwide, and is the #1 visited engineering journal website (according to the National Science Digital Library).

OTHER IAJC JOURNALS:

- The International Journal of Engineering Research and Innovation (IJERI)
  For more information visit www.ijeri.org
- The Technology Interface International Journal (TIIJ).
  For more information visit www.tiij.org

IJME SUBMISSIONS:

- Manuscripts should be sent electronically to the manuscript editor, Dr. Philip Weinsier, at philipw@bgsu.edu.

  For submission guidelines visit
  www.ijme.us/submissions

TO JOIN THE REVIEW BOARD:

- Contact the chair of the International Review Board, Dr. Philip Weinsier, at philipw@bgsu.edu.

  For more information visit
  www.ijme.us/ijme_editorial.htm

INDEXING ORGANIZATIONS:

- IJME is currently indexed by 22 agencies. For a complete listing, please visit us at www.ijme.us.

Contact us:

Mark Rajai, Ph.D.

Editor-in-Chief
California State University-Northridge
College of Engineering and Computer Science
Room: JD 4510
Northridge, CA 91330
Office: (818) 677-5003
Email: mrajai@csun.edu

www.tiij.org

www.ijeri.org

INTERNATIONAL JOURNAL OF MODERN ENGINEERING

The INTERNATIONAL JOURNAL OF MODERN ENGINEERING (IJME) is an independent, not-for-profit publication, which aims to provide the engineering community with a resource and forum for scholarly expression and reflection.

IJME is published twice annually (fall and spring issues) and includes peer-reviewed research articles, editorials, and commentary that contribute to our understanding of the issues, problems, and research associated with engineering and related fields. The journal encourages the submission of manuscripts from private, public, and academic sectors. The views expressed are those of the authors and do not necessarily reflect the opinions of the IJME editors.

EDITORIAL OFFICE:

Mark Rajai, Ph.D.
Editor-in-Chief
Office: (818) 677-2167
Email: ijmeeditor@iajc.org
Dept. of Manufacturing Systems Engineering & Management
California State University-Northridge
18111Nordhoff Street
Northridge, CA 91330-8332

THE INTERNATIONAL JOURNAL OF MODERN ENGINEERING EDITORS

TABLE OF CONTENTS

6TH IAJC INTERNATIONAL CONFERENCE

OCTOBER 11-14, 2018 – ORLANDO, FLORIDA

The leading indexed high-impact-factor conference on engineering and related technologies.

Our Hotel—Embassy Suites

Our 2018 Tour Plan—Disney Underground

Our Previous Tour—NASA's Kennedy Space Center

Editorial Review Board Members

PRELIMINARY DESIGN OF A DIAGRID TALL BUILDING

Mohammad T Bhuiyan, West Virginia State University; Roberto Leon, Virginia Tech

Abstract

A triangulated exoskeleton structural system, or diagrid, has emerged as a structurally efficient and architecturally valid solution for tall buildings. The diagrid creates a highly efficient and redundant tube structure by providing a structural network allowing multiple load paths. The diagrid system has higher inherent torsional rigidity than most other structural systems. The objective of this paper is to present the preliminary design methodology for a diagrid structural system for tall buildings. Three buildings with different heights (82, 64, and 38 stories with heights of 287m, 224m, and 133m, respectively) and footprints (with plan dimensions of 48m x 48m, 52m x 35.5m, and 33m x 33m, respectively) were selected for this study. The preliminary design and optimization follows an iterative approach by satisfying drift and acceleration limits, while reducing section sizes and changing the structural system geometry. Equations derived in the study were used to obtain the preliminary member sizes of the buildings. These preliminary member sizes were checked for suitability under earthquake and wind loads at the preliminary design stage. After a few iterations, preliminary structures were obtained.

Introduction

"The structural design of a tall building involves several stages, including the conceptual design, approximate analysis, preliminary design and optimization, followed by detailed and final design" [1]. The main design criteria are strength, serviceability and human comfort. The aim of the structural engineer is to arrive at suitable structural schemes to satisfy these criteria and assess their relative economy. At the conceptual design stage, for a very tall building design, several structural systems are examined using approximate or simplified analyses to come up with a preliminary structural system for the building. The objective of this paper is to present the preliminary design methodology for a diagrid structural system for tall buildings.

Optimal Angle of Diagrid Members

With some approximate calculations, Moon et al. [2] found that: a) the optimal angle of the diagonals necessary to achieve maximum shear rigidity for a diagrid system is about 35° and b) the optimal angle of the diagonals necessary to achieve maximum bending rigidity is 90°. Here, angle refers to the inclination of the diagonal member with respect to the horizontal plane (see Figure 1). As a real structure needs to resist both shear force and bending moment, it is expected that the optimal angle of the diagonal members of a diagrid structure will fall between these two angles. Short buildings with a low aspect ratio (height/ width) behave like shear beams, and tall buildings with a high aspect ratio tend to behave like bending beams. Thus, it is expected that as the building height-to-base width increases, the optimal angle also increases. Studies of 60-story structures, shown in Figure 1 with different diagonal angles (34°, 53°, 63°, 69°, 76°, 82°, and 90°), reveal that the buildings with a diagonal angle of 69° produce the minimum horizontal displacement at the top story [2]. Figure 1 used a constant inclination of braces along the entire height of the structure. In contrast, other studies showed that better performance for a diagrid structure with high aspect ratio can be achieved through a change in diagonal angles along the height of the structure.

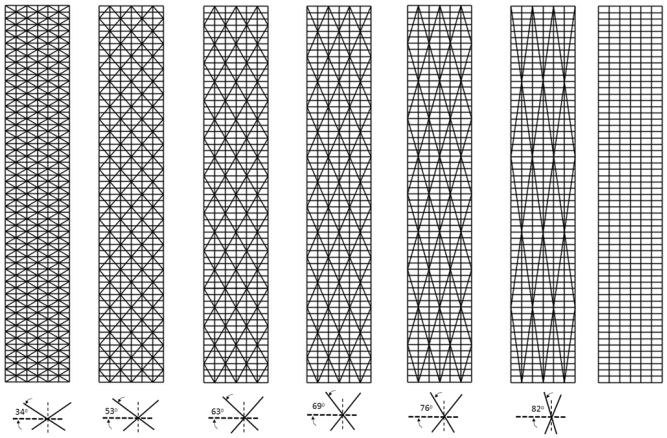

Figure 1. Sixty-Story Structures with Various Diagonal Angles for Finding the Optimal Angle

***Note*. From "Diagrid Structural systems for tall buildings: Characteristics and methodology for preliminary design," by Moon et al. (2007), *The Structural design of tall and Special buildings, 16, 205-230*. Reprinted with permission.**

Shear Stiffness and Bending Stiffness of a Diagrid Structure Module

The working principle of a diagrid system is to convert global building moment, shear and torsion into "axial action" in the diagonal brace elements. This may be visualized as in Figure 2, where an eight-story diagrid structure mod-

ule is shown. Note in this figure the definition of flange and web planes, as they relate to the direction of loading. A stiffness-based approach [3] was followed in this section to study the shear and bending stiffness of a diagrid module.

The building was modeled as a column, and subdivided longitudinally into modules, according to the repetitive diagrid pattern selected. Each module was defined by a single set of diagrids that extend over *n* stories. Figure 2 illustrates the case of an eight-story module. For this approach, diagonal braces are predominantly undergoing axial action; the contributions of bending and torsional forces to deformations are not significant. Therefore, it was assumed that axial deformation of braces would be the primary contributor to the total building deformation and, consequently, bending, shear and torsional deformation of braces were neglected in this preliminary analysis.

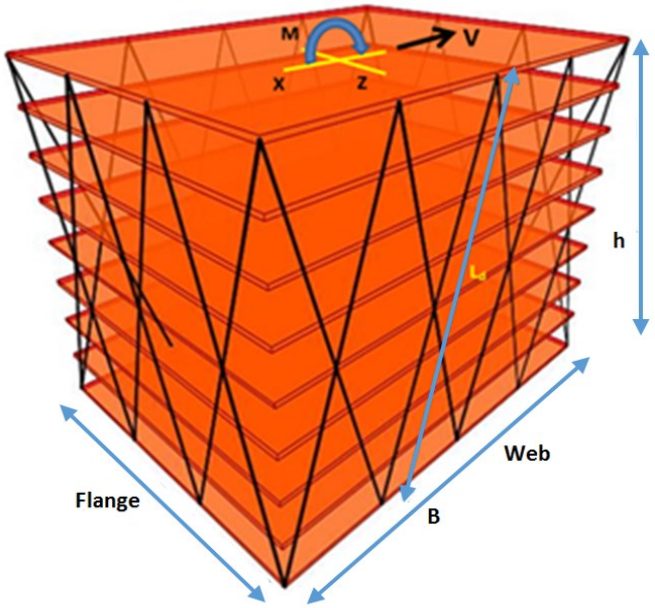

Figure 2. Eight-Story Diagrid Structure Module

Shear Stiffness

Figure 3(a) shows only two diagonal braces from the module shown in Figure 2: a shearing force of v_2 contributes to a horizontal displacement of Δu. This can easily be shown by Equation (1):

$$v_2 = 2\left(\frac{A_d E_d}{L_d}\cos^2\theta\right)\Delta u \qquad (1)$$

where, θ is the inclination of the diagonal; A_d is the cross-sectional area of diagonals; E_d is Young's modulus of the diagonal material; and L_d is the length of the diagonal.

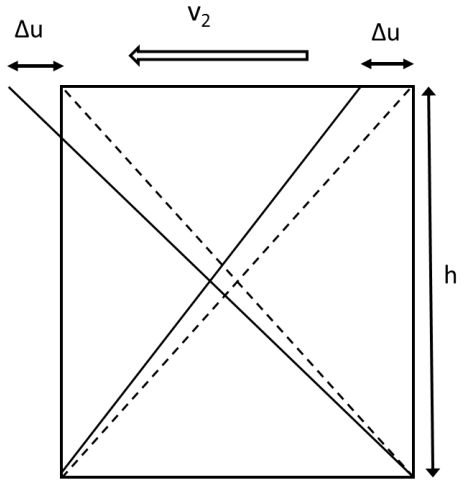

(a) Shear Deformation of the Module (see Figure 2): A Portion of the Web Plane is Shown

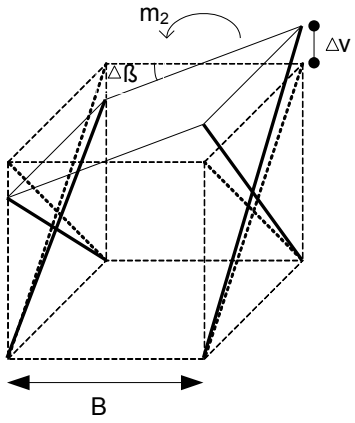

(b) Bending Deformation of the Module (see Figure 2): A Portion of the Flange Plane is Shown

Figure 3. Deformation of the Module under Different Loads

Total module shear, V, can be determined using Equations (2) and (3) (see also Figure 2):

$$V = 2N_w\left(\frac{A_{d,w}E_d}{L_d}\cos^2\theta\right)\Delta u \qquad (2)$$

$$V = K_T \cdot \Delta u \qquad (3)$$

where, N_w is the number of diagonals in one web plane of a module and the equivalent shear stiffness, K_T, can be determined using Equation (4):

$$K_T = 2N_w\left(\frac{A_{d,w}E_d}{L_d}\cos^2\theta\right) \qquad (4)$$

The relationship between K_T and the equivalent average module transverse shearing strain, γ, is can be found using Equation (5):

$$\gamma = \frac{\Delta u}{h} = \frac{V}{K_T h} \tag{5}$$

Bending Stiffness

Figure 3(b) shows only two diagonal braces from each flange plane of the module shown in Figure 2. The bending moment of m_2 that contributes to a rotation of $\Delta\beta$ to the overall deformation of the module can be found using Equation (6):

$$m_2 = 2\left[\frac{B^2 A_d E_d}{2L_d}\sin^2\theta\right]\Delta\beta \tag{6}$$

The total moment of the module, M, can be determined using Equations (7) and (8):

$$M = N_f\left[\frac{B^2 A_{d,f} E_d}{2L_d}\sin^2\theta\right]\Delta\beta \tag{7}$$

$$M = K_B \cdot \Delta\beta \tag{8}$$

where, N_f is the number of diagonals in one flange plane of the module (see again Figure 2).

Bending stiffness, K_B, can be found from Equation (9):

$$K_B = N_f\left[\frac{B^2 A_{d,f} E_d}{2L_d}\sin^2\theta\right] \tag{9}$$

If bending strain is constant over the height of the module, then $\chi = \frac{\Delta\beta}{h}$ is the contribution of bending strain to the overall deformation.

Specifying the Shear and Bending Deformation

Moon et al. [2] stated that optimal design from a motion perspective corresponds to a state of uniform shear and bending strain (deformation) along the height of the structure under the design loading. Such a distribution is possible as the bending and shear stiffness of the module correspond to those of a truss, where such a distribution is made possible by artful distribution of member sizes. They applied the principle of uniform shear and bending deformation along the height of the structure, as shown in Figure 4(a), for all of the preliminary studies. At the beginning, this study utilized the strain distribution in Figure 4(a) for preliminary sizing of the lateral load resisting system. However, studies discussed on the later parts of this paper reveal that a preliminary design based on a triangular bending and uniform shear strain distribution [see Figure 4(b)], combined with a variation of diagonal angles along the height of the structure, yields much better performance.

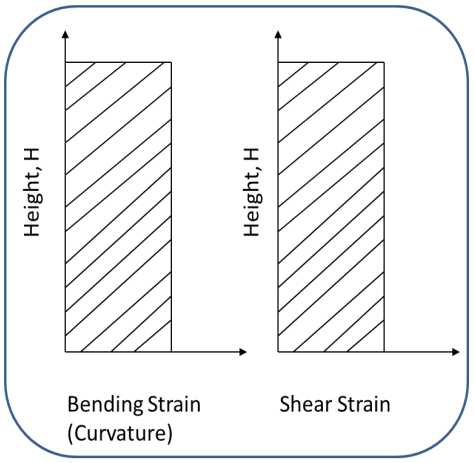

(a) Uniform Curvature and Shear Strain Distribution

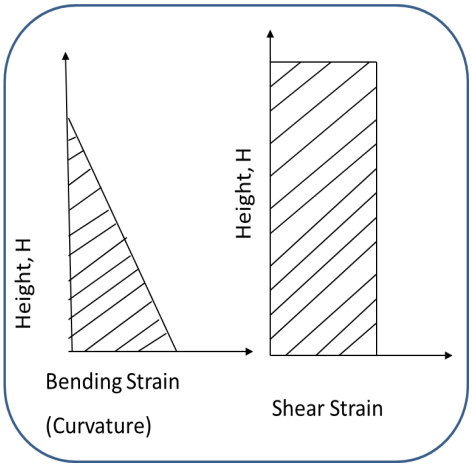

(b) Triangular Curvature Distribution and Uniform Shear Strain Distribution

Figure 4. Shear and Bending Strain Distribution along the Height of the Structure

Uniform Bending and Shear Strain Distribution

If the members of the lateral load resisting system are proportioned to achieve a uniform bending and shear strain distribution along the height of the building [see Figure 4

(a)], and assuming the diagrid structure is modeled as a cantilever beam, the deflection at the roof level of the structure is given by Equation (10):

$$u(H) = \gamma H + \frac{\chi H^2}{2} \tag{10}$$

where, γH is the contribution from shear deformation; $\frac{\chi H^2}{2}$ is the contribution from bending; γ is the uniform shear strain; and, χ is the uniform bending strain (curvature) along the height of the structure.

In order to specify the relative contribution of shear versus bending deformation, a dimensionless factor S is introduced, which is equal to the ratio of the displacement at the top of the structure, due to bending and the displacement due to shear, and which can be determined from Equation (11):

$$s = \frac{\frac{\chi H^2}{2}}{\gamma H} = \frac{H\chi}{2\gamma} \tag{11}$$

The maximum allowable displacement is usually expressed as a fraction of the total building height, $u(H)=H/\alpha$, where typical values range from H/500 to H/400. Combining Equation (10) and (11), this allowable displacement can be found using Equations (12)-(14):

$$u(H) = (1+s)\gamma H = H/\alpha \tag{12}$$

$$\gamma = \frac{1}{(1+s)\alpha} \tag{13}$$

$$\chi = \frac{2s}{H(1+s)\alpha} \tag{14}$$

From these, a parametric study can be carried out to find the optimum value of S. Equations (13) and (14), then, will yield the design values for γ, and the rotation ($\Delta\beta$) at the top of each module [see Figure 3(b)] can be obtained by summing the curvature along the height of the module. If χ is the uniform curvature then, $\Delta\beta=\chi.h$ is the rotation at the top of the module.

Inputting the value of γ into Equations (4) and (5), and the $\Delta\beta$ value into equation (7), the member sizes (cross-sectional area) of the module can be computed from Equations (15) and (16):

$$A_{d,w} = \frac{VL_d}{2N_w Eh\gamma\cos^2\theta} \tag{15}$$

$$A_{d,f} = \frac{2ML_d}{N_f B^2 Eh\chi\sin^2\theta} \tag{16}$$

where, $A_{d,w}$ is the required cross-sectional area of the diagonal members of the web plane (see Figure 2) to resist the module shear force of V; and $A_{d,f}$ is the required cross-sectional area of the diagonal members in the flange plane (see Figure 2) to resist the module bending moment of M.

Triangular Bending and Uniform Shear Strain Distribution

If the members of the lateral load resisting system are proportioned to achieve a triangular bending and uniform shear strain distribution along the height of the building, as shown in Figure 4(b), and assuming the diagrid structure is modelled as a cantilever beam, the deflection at the roof level of the structure can be given by Equation (17):

$$u(H) = \gamma H + \frac{1}{3}\phi H^2 \tag{17}$$

where, γH is the contribution from shear deformation; $\frac{1}{3}\phi H^2$ is the contribution from bending; γ is the uniform shear strain; and, ϕ is the bending strain (curvature) at the base of the structure—whereas curvature at the top of the structure is zero, as shown in Figure 4(b).

In order to specify the relative contribution of shear versus bending deformation, a dimensionless factor, s', is introduced, which is equal to the ratio of the displacement at the top of the structure, due to bending and the displacement due to shear. The value of s' can be found using Equation (18):

$$s' = \frac{\frac{1}{3}\varphi H^2}{\gamma H} = \frac{\varphi H}{3\gamma} \tag{18}$$

Assuming an allowable displacement, and combining Equations (17) and (18), the deflection at the roof level of the structure is given by Equations (19)-(21):

$$u(H) = (1+s')\gamma H = H/\alpha \tag{19}$$

$$\gamma = \frac{1}{(1+s')\alpha} \tag{20}$$

$$\chi = \frac{3s'}{H(1+s')\alpha} \tag{21}$$

Again, a parametric study was carried out to find an optimum value of s', at which point Equations (20) and (21) will yield γ and χ, respectively. Inputting the value of γ into Equations (4) and (5) and the value of $\Delta\beta$ into Equation (7), the member sizes (cross-sectional area) for this strain distribution can be computed using Equations (22) and (23):

$$A_{d,w} = \frac{VL_d}{2N_w Eh\gamma \cos^2\theta} \quad (22)$$

$$A_{d,f} = \frac{2ML_d}{N_f B^2 E \cdot \Delta\beta \cdot \sin^2\theta} \quad (23)$$

Preliminary Design Studies for the 64-Story Building

The methodology presented in the previous sections was are applied to the 64-story diagrid structure. Several iterations were carried out to determine the optimal preliminary member sizes and configuration of the diagrid structure so that it could resist both earthquake and wind action efficiently. Although several iterations were carried out, only two iteration steps are presented here.

Iteration 1

The design assumptions used for this iteration are: (i) uniform bending and shear strain distribution along the height of the structure [see Figure 4(a)]; (ii) constant inclination of braces along the entire height of the structure (see Figure 1); and, (iii) member sizes are proportioned in such a way that a wind drift of H/500 is achieved. The first step is to divide the structure into appropriate structural modules. As indicated earlier, an inclination of about 69° was suitable the selected eight-story module (see again Figure 2). The inclination of the diagonals on the long face (LF) of the module was 64.9°, and for the short face (SF) was 67.4°, which are well within optimal limits. Eight 8-story modules, then, produce the 64-story structure.

The shear forces and bending moments for each module were calculated based on equivalent static wind loads [4]. Following the calculation steps presented earlier, the member sizes of all the stories were calculated in order to satisfy both shear and bending requirements [4]. Table 1 presents the preliminary choices of pipe sections for all of the diagonals of the building. The structure having the preliminary design of Table 1 was analysed with SAP2000 for modal properties. Figure 5(a) shows the mode shapes in the two translational directions. It is evident from the figure that the mode shape lines are not smooth enough, especially in the upper part of the structure. The fundamental periods in the two translational directions were T_{1Z} = 4.76 sec and T_{1X} = 3.61 sec and, in the torsional direction, T_{1Y} = 1.42 sec. The inter-story drift plot [see Figure 6(a)] due to wind shows that the lower part of the structure is extremely stiff and the upper part of the structure is very soft and overall the response of the structure is not satisfactory.

For a quick and very crude estimate of the structure's response to earthquake loads, a non-linear model of this preliminary structure was developed in SAP2000 using an axial link element. The axial link element used can have non-linear hysteretic deformation in the axial direction of the diagonal braces. A bi-linear force-deformation relationship was used for all of the braces. The Kobe earthquake motion at Takarazu station was used to perform a 3D nonlinear time history analysis. Figure 7(a) shows the inter-story drift of the structure; it is evident that the overall response of the structure was not satisfactory, as the top part of the structure was again very flexible when compared to the bottom part of the structure.

Table 1. Preliminary Member Sizes for the 64-Story Diagrid Structure (Iteration 1)

Story	Pipe section for long face members	Pipe section for short face members
1st – 8th	900mm dia, 100mm thickness	750mm dia, 60mm thickness
9th – 16th	830mm dia, 90mm thickness	750mm dia, 57.5mm thickness
17th – 24th	750mm dia, 75mm thickness	750mm dia, 55mm thickness
25th – 32nd	750mm dia, 55mm thickness	750mm dia, 50mm thickness
33rd – 40th	650mm dia, 45mm thickness	700mm dia, 50mm thickness
41st – 48th	550mm dia, 35mm thickness	650mm dia, 42.5mm thickness
49th – 56nd	500mm dia, 25mm thickness	600mm dia, 35mm thickness
57th – 64th	500mm dia, 15mm thickness	550mm dia, 25mm thickness

Iteration 2

The design assumptions used for this iteration were: (i) a triangular bending and uniform shear strain distribution along the height of the structure [see Figure 4(b)]; (ii) a variation of angle of inclination of the braces along the height of the structure [see Figure 8(a)]; and, (iii) the member sizes were proportioned in such a way that a wind drift of H/450 was achieved. Five 8-story modules (see again Figure 2), two 6-story modules and three 4-story modules were used to construct the 64-story structure shown in Figure 8(a). Thus, the inclination of the diagonals was decreased along the height of the structure. Table 2 presents the preliminary

choices of pipe sections for all of the diagonals of the building. Figure 5(b) shows the mode shape in the two translational directions. The mode shapes indicate better behaviour of the building. The fundamental periods in the two translational directions were T_{IZ}= 5.2 sec and T_{IX}= 3.8 sec and, in the torsional direction, T_{IY}= 1.41 sec. A plot of inter-story drifts due to wind is shown in Figure 6(b). Inspection of the figure shows that the response of the structure appears satisfactory. The maximum acceleration at the roof level was found to be 22.7 milli-g and the RMS acceleration was 6.1 milli-g; both were below the acceptable limits.

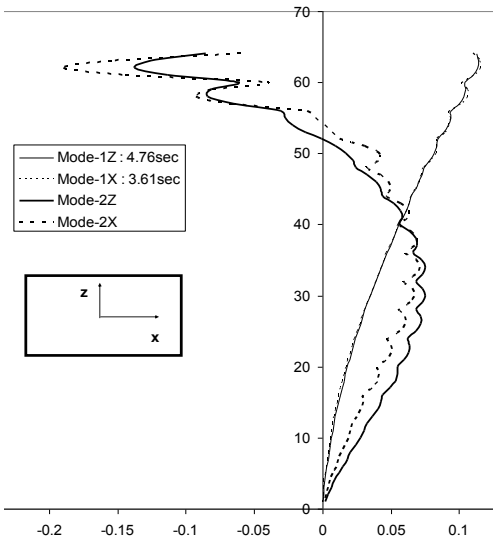

(a) Iteration-1

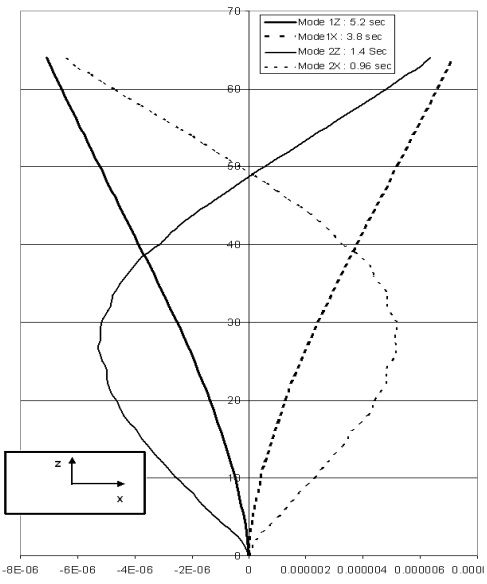

(b) Iteration-2

Figure 5. Mode Shape of the 64-Story Preliminary Structure

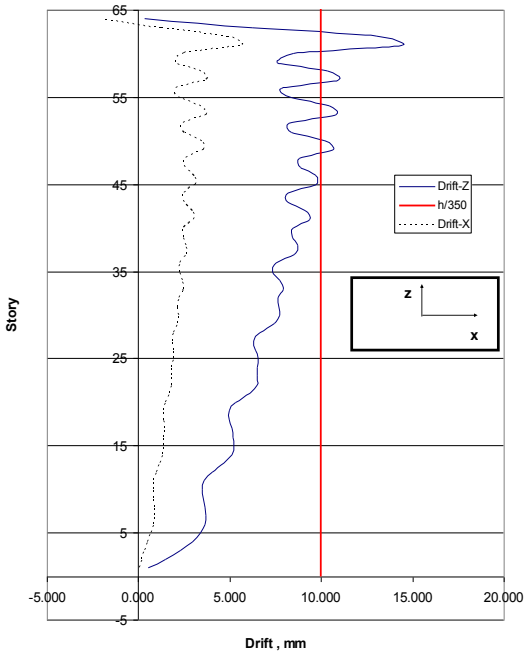

(a) Iteration-1

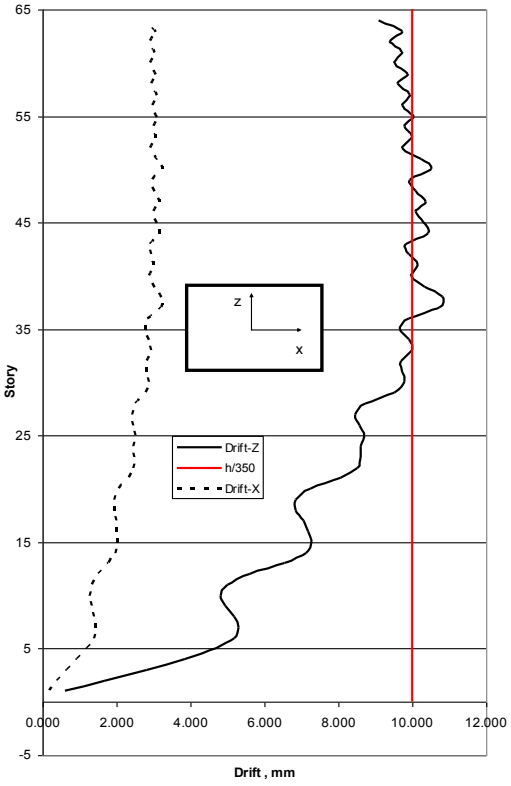

(b) Iteration-2

Figure 6. Inter-Story Drift of the 64-Story Structure due to Wind

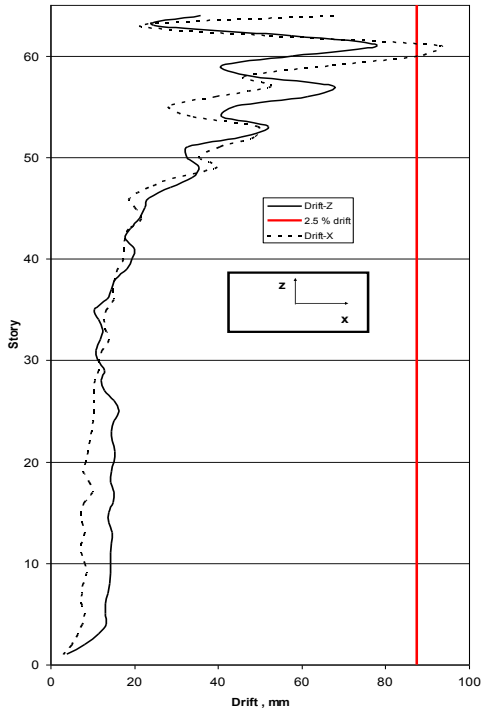

(a) Iteration-1

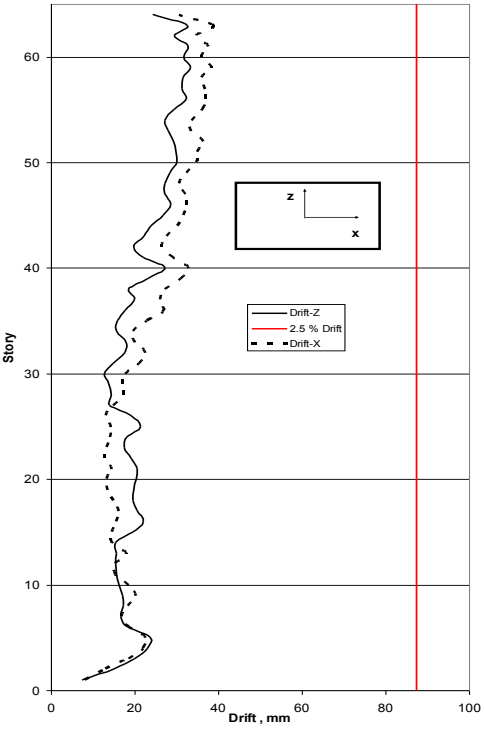

(b) Iteration-2

Figure 7. Inter-Story Drift of the 64-Story Structure due to Kobe Earthquake

Similar to Iteration 1, The Kobe earthquake motion at Takarazu station was used to perform a 3D nonlinear time history analysis. Figure 7(b) shows the inter-story drift of the structure; it is evident that overall response of the structure was much better compared to the building of Iteration 1.

Table 2. Preliminary Member Sizes for the 64-Story Diagrid Structure (Iteration 2)

Story	Pipe section for long face members	Pipe section for short face members
1st – 8th	750mm dia, 70mm thickness	750mm dia, 50mm thickness
9th – 16th	750mm dia, 70mm thickness	750mm dia, 50mm thickness
17th – 24th	750mm dia, 65mm thickness	750mm dia, 50mm thickness
25th – 32nd	750mm dia, 57.5mm thickness	700mm dia, 47.5mm thickness
33rd – 40th	750mm dia, 50mm thickness	700mm dia, 40mm thickness
41st – 48th	700mm dia, 45mm thickness	650mm dia, 35mm thickness
49th – 56nd	700mm dia, 45mm thickness	650mm dia, 35mm thickness
57th – 64th	650mm dia, 40mm thickness	600mm dia, 30mm thickness

Preliminary Design Studies for the 82-Story Building

Similar to the 64-story structure, the same methodology was applied to the 82-story diagrid structure [see Figure 8(b)]. As the earlier design assumptions yielded better performance for the 64-story structure, the same were used for this 82-story structure. The first step was to divide the structure into appropriate structural modules. Six 8-story modules (see again Figure 2), three 6-story modules and four 4-story modules were used to construct the 82-story structure shown in Figure 8(b). Thus, the inclination of the diagonals was decreased along the height of the structure. Table 3 presents the preliminary choices of pipe sections for all of the diagonals of the building.

Figure 9(a) shows the mode shape in the translational direction. The mode shapes indicate that the behaviour of

the building was acceptable. The fundamental periods in the two translational directions were T_{1Z} = 5.567 sec and T_{1X} = 5.567 sec and, in the torsional direction, T_{1Y} = 1.558 sec. A plot of deflection of the structure due to wind is shown in Figure 9(b). The roof displacement was found to be 0.534m in the cross-wind direction and 0.471m in the along-wind direction, which was a little less than H/450. The maximum acceleration at the roof level was found to be 31.9 milli-g and 21.9 milli-g in the cross-wind and along-wind directions, respectively; the RMS acceleration was 8.6 milli-g and 6 milli-g in the cross-wind and along-wind directions, respectively. It is important to note that the cross-wind displacement and acceleration dominated the design, as was the case with a typical tall building. The limit for maximum acceleration was 25 milli-g and that for RMS acceleration was 9 milli-g. As can be seen, controlling the acceleration and displacement for wind was the main concern during the preliminary design stage of this structure.

Preliminary Design Studies for the 38-Story Building

Similar to the other two structures, the methodology was applied to the 38-story diagrid structure [see Figure 8(c)]. Previous design assumptions were used for this 38-story structure. Five 6-story modules and two 4-story modules were used to construct the 38-story structure as shown in Figure 8(c). Thus, the inclination of the diagonals was decreased along the height of the structure. Table 4 shows preliminary member sizes. Figure 10 shows the mode shape in the translational direction. The mode shapes indicate that the behaviour of the building was acceptable. The roof displacement was found to be 0.144m, which was less than H/450, and the maximum acceleration at roof level was 15.5 milli-g due to wind. Behaviour of the structure due to seismic action was given much consideration, while selecting the preliminary member sizes.

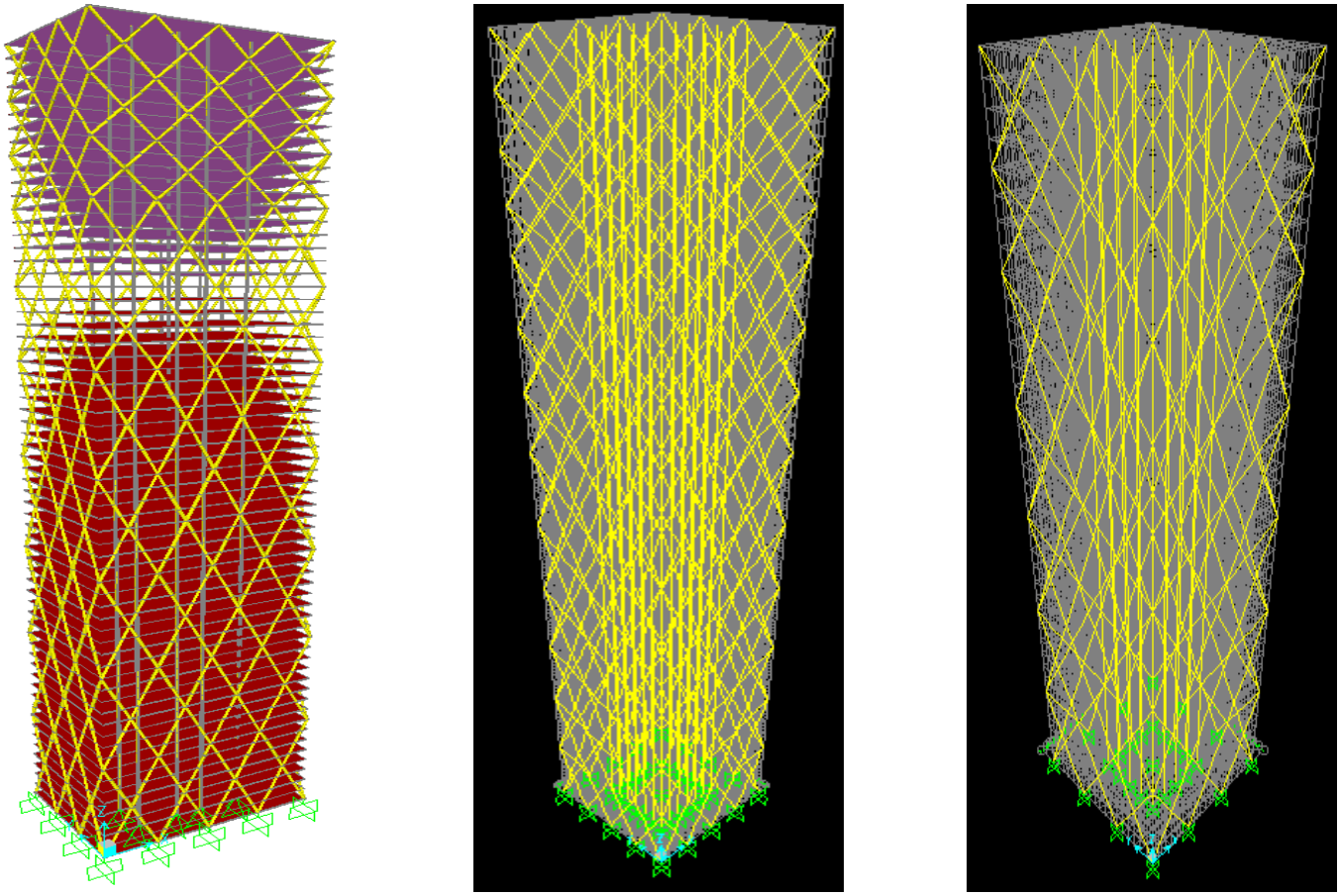

(a) 64-Story **(b) 82-Story** **(c) 38-Story**

Figure 8. 3D View of the Diagrid Structure

Table 3. Preliminary Member Sizes for the 82-Story Diagrid Structure

Story	Pipe section
1st – 8th	800mm dia, 80mm thickness
9th – 16th	800mm dia, 80mm thickness
17th – 24th	800mm dia, 75mm thickness
25th – 32nd	750mm dia, 75mm thickness
33rd – 40th	750mm dia, 70mm thickness
41st – 48th	750mm dia, 65mm thickness
49th – 54th	750mm dia, 65mm thickness
55th – 60th	700mm dia, 60mm thickness
61st – 66th	700mm dia, 55mm thickness
67th – 70th	700mm dia, 55mm thickness
71st – 74th	650mm dia, 55mm thickness
75th – 78th	650mm dia, 50mm thickness
57th – 64th	650mm dia, 40mm thickness

Table 4. Preliminary Member Sizes for the 38-Story Diagrid Structure

Story	Pipe section
1st – 6th	450mm dia, 30mm thickness
7th – 12th	450mm dia, 30mm thickness
13th – 18th	500mm dia, 30mm thickness
19th – 24nd	475mm dia, 30mm thickness
25rd – 30th	450mm dia, 30mm thickness
31st – 34th	425mm dia, 25mm thickness
35th – 38th	425mm dia, 25mm thickness

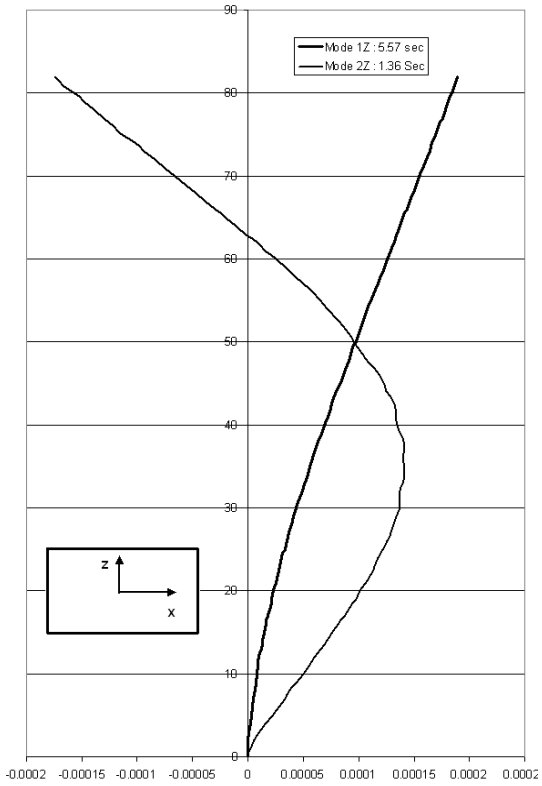

(a) 1st and 2nd Translational Mode

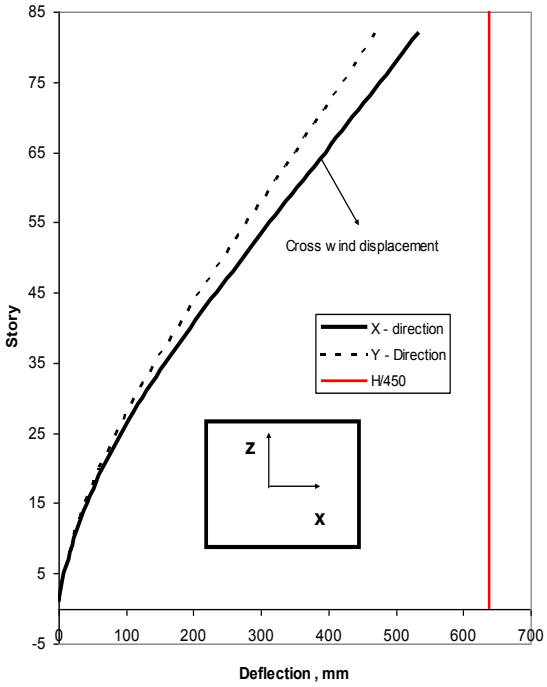

(b) Deflection due to wind

Figure 9. Performance of 82-Story Preliminary Structure

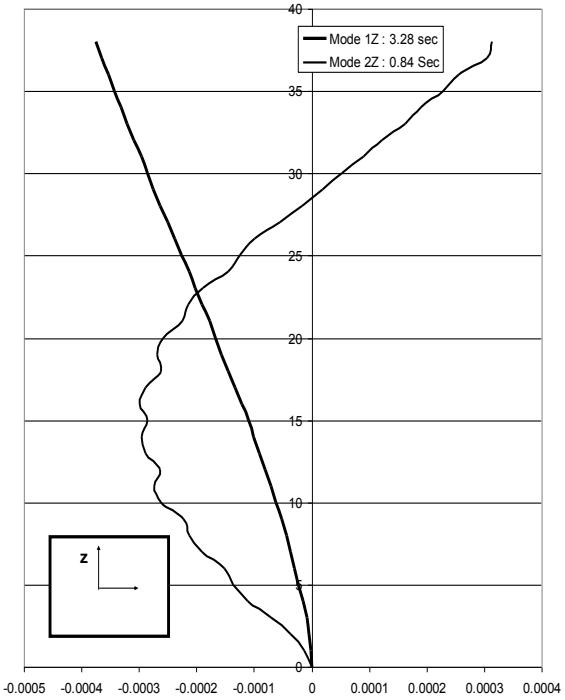

Figure 10. 1st and 2nd Translational Mode of the 38-Story Building

Conclusion

Preliminary design and optimization for a diagrid structural system was presented in this paper. Case studies of three buildings with different heights (82, 64, and 38 stories) and footprint are presented. Following the methodology presented here, the preliminary structure of all of the buildings satisfied the requirements: (a) H/450 limit on top floor displacement; (b) h/350 inter-story drift limit for wind; (c) 9 milli-g RMS acceleration limit, etc. The study showed that better dynamic behaviour of a tall diagrid structure can be obtained by changing the diagonals' angle of inclination along the building height and by assuming a philosophy of constant shear strain distribution combined with a triangular flexural strain distribution along building height. This more effectively forces most of the nonlinearity to occur in the lower portion of the structure during an earthquake and resulted in a better inter-story drift distribution along the height of the building for a wind event.

References

[1] Jayachandran, P. (2009). Design of Tall Buildings: Preliminary Design and Optimization. *National Workshop on High-rise and Tall Buildings*, Hyderabad, India.

[2] Moon, K., Connor, J., & Fernandez, J. (2007). Diagrid Structural systems for tall buildings: Characteristics and methodology for preliminary design. *The Structural design of tall and Special buildings*, *16*, 205-230.

[3] Connor, J. (2003). *Introduction to Structural Motion Control*. Prentice-Hall: Englewood Cliffs, NJ.

[4] Bhuiyan, M.T.R. (2011). *Response of diagrid tall building to wind and earthquake actions*. (Unpublished doctoral dissertation), ROSE School, Pavia, Italy.

Biographies

MOHAMMAD T BHUIYAN is an assistant professor of civil engineering at West Virginia State University (WVSU). He earned his BSc in Civil Engineering from Bangladesh University of Engineering & Technology, Dhaka; an MSc in Earthquake Engineering jointly from Universite Joseph Fourier, France and ROSE School, Italy; and a Ph.D in Earthquake Engineering from ROSE School with joint program at Georgia Tech. His research interest include tall buildings, earthquake engineering, soil-structure interaction, etc. Dr. Bhuiyan may be reached at towhid@wvstateu.edu

ROBERTO LEON is a D.H. Burrows Professor in the department of Civil and Environmental Engineering at Virginia Tech. He is a nationally and internationally recognized faculty member for his research, teaching, and service. He is acknowledged to be one of the leading researchers in the field of steel-concrete composite structures and earthquake engineering. His work has affected numerous national and international design codes. He was president of the Consortium of Universities for Research in Earthquake Engineering (CUREE) and president of the Network for Earthquake Engineering Simulation (NEES). He also served as president of the Board of Governors of the Structural Engineering Institute (SEI) of ASCE. Dr. Leon may be reached at rleon@vt.edu

THE VALUE OF ELECTRICITY STORAGE IN THE PRESENCE OF RENEWABLE ENERGY SOURCES IN THE OPERATION OF MULTI-VECTOR ENERGY SYSTEMS

Hossein Ameli, Imperial College London, UK; Meysam Qadrdan, University of Cardiff, UK; Goran Strbac, Imperial College London, UK;
Ali Ameli, University of Paderborn, Germany; Mohammad Taghi Ameli, Shahid Beheshti University, Iran;
Saeid Moslehpour, Hartford University

Abstract

In the near future, our ability to meet the world's the electricity demand becomes more challenging, as the share of wind generation would be increased. Gas-fired power plants as a link between gas and electricity networks could manage the variable nature of wind. Thus, these networks would be more interdependent in the future. In this study, the authors investigated the value of electricity storage in order to address the challenges of balancing our energy resources. An operational model of gas and electricity networks as a coupled multi-vector energy system was used to minimize the operational costs of both networks simultaneously. A further set of case studies on Great Britain's gas and electricity networks in 2030 was derived to evaluate the performance of electricity storage. The results of this study validate the performance of electrical storage in the presence of significant amounts of wind in improving the operation of gas and electricity networks. It was shown that up to £23.1M could be achieved when electricity storage facilities are employed in the system.

Introduction

The variable nature of wind could cause important operational challenges, as the share of wind in Great Britain (GB) will be increased in the near future [1]. Due to zero operational costs, as well as environmentally friendly features of wind, so using wind in order to meet the electricity demand has been given priority. In order to compensate for the variability of wind and other types of generation technologies such as nuclear, carbon and capture storage (CCS) equipped coal, and gas-fired power plants (gas plants) should be employed. Gas plants link electricity and gas networks. In the electricity network, gas plants supply electricity, while, in the gas network, these plants are gas-demand, as they consume gas for electricity generation. Hence, wind variability is reflected as variable gas-demand in the gas network. The role of flexible options for dealing with energy-balancing challenges of power systems in the presence of renewable energy sources (RES) has been presented in several studies [2-4]. Flexibility is defined as the ability of a system to deal with generation and demand variability, given that an acceptable reliability is maintained [2]. In a study by Ma et al. [3], the authors illustrated that in order to supply 80% of the electricity from variable RES in an isolated power system such as ERCOT, in Texas, there is a need to enhance generation flexibility and virtually eliminate minimum generation constraints imposed through must-run baseload generators. In this current study, then, the author proposed replacing conventional regulation and spinning reserves with a combination of demand-side response, energy storage, and use of curtailed variable generations. Pudjianto et al. [4] studied the value of electrical storage in terms of costs and duration work in GB's electricity system. The proposed model optimizes the investment side by taking into account the security and reserve constraints. The results demonstrated the role of electricity storage in the reduction of the required investment in system reinforcement as well as transmission congestion management [4]. In the mentioned research, the gas supply constraints were not considered.

Few studies looked at the impact of wind generation on gas network operation in detail [5-8]. Therefore, in this current study, the value of electricity storage as a flexible option in order to address the balancing challenges of supply and demand in the operation of electricity network as well as gas network is studied. Electricity storage could facilitate the accommodation of RES into the system. In order to validate the role of electricity storage, a set of case studies on the GB gas and electricity networks in 2030 was derived. The objective was to minimize the operational costs of the gas and electricity networks simultaneously.

Modeling Methodology

The updated version of the combined gas and electricity networks (CGEN) model [5] as an optimization tool for detailed analysis of operation of coupled gas and electricity networks was used. The model was able to minimize the operational costs of both networks simultaneously. The costs of power generation, gas supplies, electrical and gas load shedding, emission penalties, storage operations, and negative changes in line-pack were considered, and are given in Equations (1)-(3). The objective function was to mini-

mize the operational costs of both network, simultaneously. It is worth mentioning that line-pack is the amount of gas stored in the pipelines in order to deal with fast demand changes in the gas network.

$$M^{\text{elec}} = \sum_t \left\{ \left(\sum_l \left(C_l^{\text{fuel}} + C_l^{\text{var}} \right) P_{l.t} + \sum_b C^{\text{es}} P_{b.t}^{\text{es}} + \sum_g \left(C_g^{\text{ur}} P_{g.t}^{\text{ur}} \right) + C_{g.t}^{\text{su}} + C_{g.t}^{\text{sd}} + C_{g.t}^{\text{em}} \right) \right\} \quad (1)$$

$$M^{\text{gas}} = \sum_t \left\{ \left(\sum_y C_y^{\text{gas}} Q_{i.t}^{\text{gsu}} + \sum_s (C_s^{\text{in}} - C_s^{\text{ab}}) Q_{s.t}^{\text{gst}} + \sum_m C^{\text{gas}} \partial LP_{m.t} + \sum_n C^{\text{gsh}} Q_{n.t}^{\text{gsh}} \right) \right\} \quad (2)$$

$$M^{\text{tot}} \left(£ \right) = M^{\text{elec}} + M^{\text{gas}} \quad (3)$$

In the electricity network, the following constraints for each time step were taken into account: power balance between supply and demand; the physical limitations of the generators; transmission line capacity; generator characteristics, such as minimum up/down time; and, available spinning reserve. The electricity storage at each busbar of the electricity network and each time step can be modeled using Equations (4)-(7):

$$E_{t,b}^{\text{stor}} = E_{t-1,b}^{\text{stor}} + E_{t,b}^{\text{ab}} * \zeta - E_{t,b}^{\text{in}} \quad (4)$$

$$P_{t,b}^{\text{ab}} \le P_b^{\text{abmax}} \quad (5)$$

$$P_{t,b}^{\text{in}} \le P_b^{\text{inmax}} \quad (6)$$

$$E_{t,b}^{\text{stor}} \le E_b^{\text{stormax}} \quad (7)$$

where, $E_{t,b}^{\text{ab}}$ and $E_{t,b}^{\text{in}}$ are limited by the rated output power capacity of the storage.

Moreover, the energy capacity of the storage restricts $E_{t,b}^{\text{stor}}$. A round-trip efficacy of 70%, and six hours of work [4], were assumed for the electricity storage. The gas flow through the pipelines was calculated by the Panhandle A equation, introduced by Osiadacz [9]. Constraints of the gas network include gas flow balance, pressure constraints, gas terminal and storage facility limitations, and gas compressor operation limits. All constraints of the gas and electricity network have to be met simultaneously. Constraints of the gas and electricity networks operation can be found in the studies by Qadrdan et al. [7] and Ameli et al. [8]. The model was implemented using the FICO Xpress optimization tool. The Xpress-mmxnlp solver for MINLP (Mixed Integer Non-Linear Programming) was applied in order to minimize the objective function over the studied time.

Case Studies

Great Britain's coupled gas and electricity system operation was modeled out to 2030. Performance of electricity storage with a 5-GW output power capacity, 15-GWh energy capacity (5-GW case), and 10-GW/30-GWh capacity (10-GW case) was modeled in order to evaluate and compare electricity balancing challenges with the reference case (*Ref*). In the *Ref* case, no special flexibility was considered for mitigating the consequences of integration of a large capacity of wind generation onto the grid. The impact of employing electricity storage with different capacities on the operation of the gas network (i.e., compressor power) was also investigated. Table 1 presents the generation mix used in this study.

Table 1. Power Generation Mix in 2030 [1]

Generation Technology	Capacity (GW)
Wind	52
Gas	33
Interconnector	11.5
Nuclear	9
Coal with CCS	4.5
Pumped storage	2.7
Other	2.3

Figure 1 shows the GB gas national transmission system (NTS) as well as 29-Busbar electricity transmission networks layout. The electricity demand and the gas demand data are elaborated from published data [1] and a study by Osiadacz [10].

Numerical Results

Unit Commitment of Thermal Generating Plants

Figure 2 shows that a number of committed gas plants store less in comparison to the *Ref* case. The reason is that, in storage cases, the need for gas generation to meet demand is decreased as storage is part of energy balancing. Therefore, these plants operate less frequently. In a comparison of the 5-GW and 10-GW cases, as more storage is available, so is there less of a need for gas plants and, therefore, the num-

ber of committed gas plant units to the electricity network is reduced.

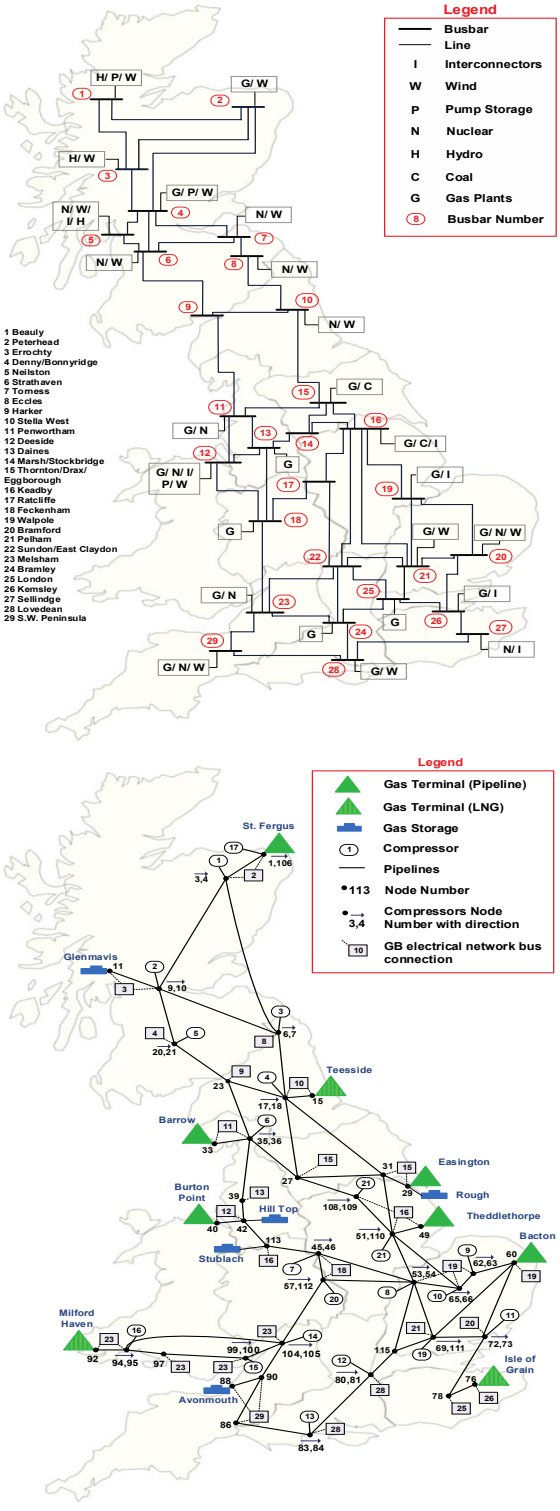

Figure 1. GB 29-busbar Electricity Transmission System—GB Gas National Transmission System [8]

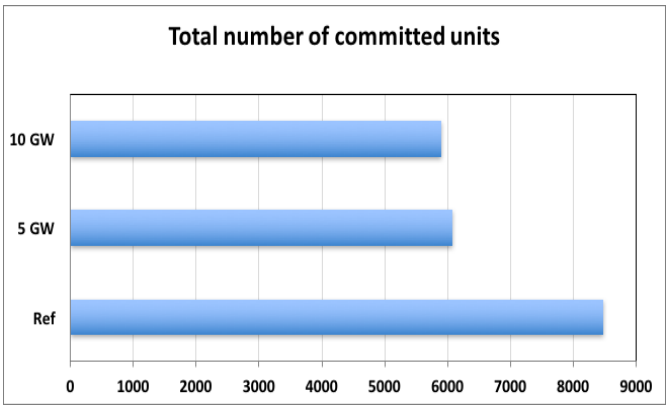

Figure 2. Total Number of Committed Gas Plant Units in Different Cases

Power Generation Mix

In Figure 3, changes in the electricity generated by different types of technologies with respect to the *Ref* case are presented. Electricity generated by nuclear changes slightly in different cases. In the 5-GW case, electricity generated through gas plants over the week was reduced by over 110 GWh. This reduction is compensated mainly by an increase in electricity generated by wind. In the 10-GW case, because of more available storage capacity, absorption of more wind generation reduces the output from gas plants (130 GWh). In addition, importing electricity through interconnectors is approximately 30 GWh less in storage cases. Through the electricity storage option, it can be shown that the need for gas plants to deal with wind generation has been decreased. Consequently, less variable gas demand for electricity generation in the gas network is required.

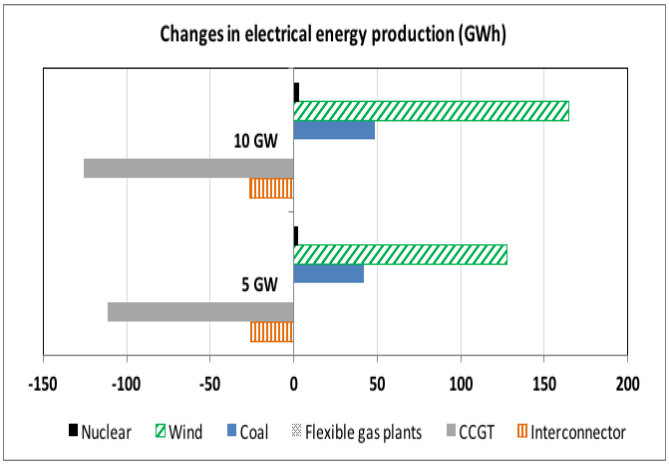

Figure 3. Changes in Electricity Generation from Various Types of Technologies, Compared to the *Ref* Case

Wind Curtailment

Figure 4 shows curtailed wind over the modeling time horizon for different cases. It can be seen that employment of electricity storage reduced the curtailed wind as part of the excess wind power absorbed by electricity storage. Electricity storage reduced the wind curtailment by almost 33% and 42% (compared with the *Ref* case) in the 5-GW and 10-GW cases, respectively. Nevertheless, at some periods the total electricity generated through wind and must-run technologies is more than demand and, due to the limitation of electricity storage capacity, a portion of wind generation is curtailed. In these cases, about 255 GWh and 210 GWh of wind was curtailed, especially during high-wind periods.

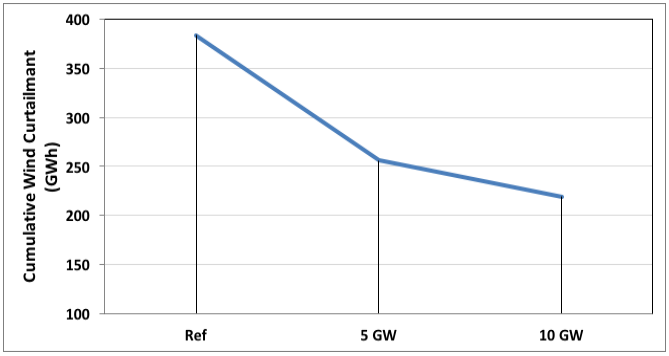

Figure 4. Wind Curtailment in Different Case Studies

Gas Compressor Operation

Gas pressure will be lost in the gas network, due to the friction of the pipelines. So, the installation of compressors was considered [9]. The role of the compressor is to maintain the gas flow pressure in an acceptable range. Table 2 presents the compressor consumption power for the different cases. It can be concluded that, in storage cases, the gas pressure in the pipelines is higher, as the prime mover consumption power of the compressors in order to increase the pressure is lower than the *Ref* case.

Table 2. Compressor Power Consumption (MWh)

Case Study	Power Consumption
Ref	1538.2
5 GW	1415.7
10 GW	1386.8

Operational Costs

Table 3 shows the operational costs of the gas and electricity networks over a typical winter week in the presence of different electricity storage capacities. The lowest operational cost was achieved through the 10-GW case, due to the fact that more storage capacity is available for injecting and absorbing the required power to the network. The operational cost of electricity storage is assumed to be zero. A significant cost reduction in the electricity network is related to the fact that in the economic dispatch of power generation, storage as a cheaper option is employed more than the gas plants and interconnectors. As a result, the gas consumption for power generation is decreased, and so the gas network operational cost has been reduced as well. The considerable cost savings (£22.12M and £23.08M) over the week in electricity storage cases indicates the value of this flexible option.

Table 3. Gas and Electricity Networks Operational Costs over the Week in £M

Case Study	Electricity Network	Gas Network	Total
Ref case	69.80	801.13	870.93
5 GW case	53.56	795.24	848.81
10 GW case	53.37	794.47	847.84

Conclusions

An optimization model for operation of the Great Britain (GB) coupled gas and electricity system was implemented in order to address the supply and demand balancing challenges of renewable energy sources (RES) integration onto the network. That is, the performance of employing different capacities of electricity storage in the presence of wind were studied. Also, the impacts of this flexibility option on operation of the GB gas network, such as compressor consumption power, were analyzed. Utilizing electricity storage indicated the reduction of wind curtailment from 33% in the case of 5-GW/15-GWh storage capacity to 42% in the case of 10-GW/30-GWh storage capacity. Better management of gas network operation was presented through power consumption of the gas compressors.

In addition, electricity storage contributed to a considerable decrease in the operational cost of the GB gas and electricity supply systems. The reason for this performance of electricity storage is due to the fast reaction of storage in the storing and injecting of electricity, acceptable efficiency, and zero-operational cost feature of this device. For the next step of this research, the investment perspectives of employing electricity storage should be taken into account.

Nomenclature

Superscripts

em	Emission
es	Electrical load shedding
gs	Gas load shedding
gst	Gas flow of storage facility
gsu	Gas flow from supply
in	Injection
tot	Total
ur	Unserved reserve
var	Variable
ab	Absorption
stor	Storage

Subscripts

b	Buses
g	Thermal generators
l	Generation units
p	Pump units
s	Storage
t	Time (h)
y	Terminal

Variables and Parameters

C	Cost (£)
M	Operational costs (£M)
P	Power generation of units (MW)
Q	Volumetric gas flow rate(m^3/s)
∂LP	Rate of change of gas linepack (m^3/s)
ζ	Efficiency
E	Energy (MWh)

References

[1] National Grid (2014). UK future energy scenarios. Retrieved from https://www.nationalgrid.com/uk/publications/future-energy-scenarios-fes

[2] Ma, J., Member, S., Silva, V., Belhomme, R., Kirschen, D., & Ochoa, L. (2013). Evaluating and planning flexibility in sustainable power systems. *IEEE Transactions on Power Systems*, *4*(1), 200–209.

[3] Denholm, P., & Hand, M. (2011). Grid flexibility and storage required to achieve very high penetration of variable renewable electricity. *Energy Policy*, *39*(3), 1817-1830.

[4] Pudjianto, D., Aunedi, M., Djapic, P., & Strbac, G. (2014). Whole-systems assessment of the value of energy storage in low-carbon electricity systems. *IEEE Transaction on Smart Grid*, *5*(2), 1098-1109.

[5] Qadrdan, M., Chaudry, M., Wu, J., Jenkins, N., & Ekanayake, J. (2010). Impact of a large penetration of wind generation on the GB gas network. *Energy Policy, 38*, 5684-5695.

[6] Martinez-Mares, A., & Fuetre-Esquivel, C. (2012). A unified gas and power flow analysis in natural gas and electricity coupled networks. *IEEE Transaction on Power Systems, 27*(4), 2156-2166.

[7] Qadrdan, M., Ameli, H., Strbac, G., & Jenkins, N. (2017). Efficacy of options to address balancing challenges: Integrated gas and electricity perspectives. *Journal of Applied Energy, 190*, 181-190.

[8] Ameli, H., Qadrdan, M., & Strbac, G. (2017). Value of gas network infrastructure flexibility in supporting cost effective operation of power systems. *Journal of Applied Energy, 202*, 571-580.

[9] Osiadacz, A. (1987). *Simulation and Analysis of Gas Networks*. Gulf Publishing Company.

[10] UK Infrastructure Transitions Research Consortium. (2014). National infrastructure assessment: Analysis of Options for Infrastructure provision in Great Britain. Retrieved from http://www.itrc.org.uk/national-infrastructure-assessment-analysis-of-options-for-infrastructure-provision-in-great-britain-interim-results/#.WlKSKE2Ww5s

Biographies

HOSSEIN AMELI received his BSc and MSc degrees in electrical engineering from Amir Kabir University, Iran, and the Technical University of Berlin, Germany, respectively. He is currently a PhD student at Imperial College London, UK. His research interests include modeling, opti-

mization, planning, and operation of energy systems. Mr. Ameli may be reached at h.ameli14@imperial.ac.uk

MEYSAM QADRDAN is a lecturer in energy networks and systems at the Institute of Energy, Cardiff University, UK. His research interests include multi-vector energy system modeling and optimization, operational and expansion planning of combined gas and electricity networks. Mr. Qadrdan may be reached at qadrdanm@cardiff.ac.uk

GORAN STRBAC is a professor of energy systems at Imperial College London, UK, with research interests in advanced modeling and analysis of operation, planning, security, and economics of low-carbon energy systems. Dr. Strbac may be reached at g.strbac@imperial.ac.uk

ALI AMELI received his MSc degree in electrical engineering from Shahid Beheshti University, Abbaspoor Technical Campus, and started his PhD in 2012 at the University of Paderborn in Germany in the field of electric vehicles. He has published several papers regarding his research so far. His interests include renewable energies, smart grids, micro-grids, and grid management. Mr. Ameli may be reached at aameli@campus.uni-paderborn.de

MOHAMMAD TAGHI AMELI received his BSc in electrical engineering from the Technical College of Osnabrueck, Germany, in 1988, and his MSc and PhD degrees from the Technical University of Berlin, Germany, in 1992 and 1997, respectively. He is a professor on the EE faculty of Shahid Beheshti University, Tehran, Iran. He was the general director of the Iran Research and Technology Institute for Electric Machines for three years. His research interests include power system simulation, operation, planning and control of power systems, renewable energy in power systems, and smart grids. Dr. Ameli may be reached at m_ameli@sbu.ac.ir

SAEID MOSLEHPOUR is a full professor and department chair in the Electrical and Computer Engineering Department in the College of Engineering, Technology, and Architecture at the University of Hartford. He holds a PhD (1993) from Iowa State University and Bachelor of Science (1989) and Master of Science (1990) degrees from the University of Central Missouri. His research interests include failure analysis, logic design, CPLDs, FPGAs, embedded electronic system testing, and distance learning. Dr. Moslehpour may be reached at moslehpou@hartford.edu

A New Model for Foam Flow in Pipes and its Application in Drilling Processes

Y. Wang, Louisiana State University; C. Thiberville, Louisiana State University; S.I. Kam, Louisiana State University

Abstract

In this study, the authors developed a new foam model based on both dry-foam and wet-foam rheological properties across a wide range of gas and liquid velocities. The first is referred to as a high-quality regime, where the steady-state pressure drop decreases with increasing gas velocity, due to reduced bubble stability; the second is referred to as a low-quality regime, where the steady-state pressure drop increases with increasing gas velocity near the finest foam texture. Both regimes involved fixed liquid-velocity experiments. Further developing the previous foam model prototype, this new model with nine model parameters captures two distinct flow regimes independently with a smooth transition in between. When the model was applied to a foam-assisted drilling process, it clearly showed advantages over the existing models in the literature, in terms of predicting bottom hole pressure, foam quality, flow velocity, and foam density. This study also showed how to obtain other key variables and parameters for the analysis of foam flow, such as foam viscosity, liquid film thickness, friction factor, and Reynolds number in a wide range of gas and liquid velocities, using the format of contour plots.

Introduction

Foams are two-phase mixtures in which gas bubbles (the internal phase) are separated by interconnecting thin films of liquid (the external phase). Surface-active agents (surfactants, or commonly called foaming agents) are designed to trap the gas phase for a desired period of time. Gas fraction in the entire foam mixture, referred to as foam quality, defines how much foam is dry or wet. With a sufficient amount of liquid, wet foams tend to have spherical bubbles with relatively large Plateau borders (the liquid-accumulated areas between gas bubbles) at low capillary pressure, while dry foams have polyhedral bubbles with very thin foam films and tiny Plateau borders at high capillary pressure. Foam quality affects bubble size and shape and, thus, the resulting interactions between individual bubbles, between bubbles and pipe wall, and between bubbles and the surrounding liquid. Bubble size distribution in a foam mixture is defined as foam texture; if the mixture is dominated by a large population of well-developed tiny bubbles, it is called fine-textured foam, otherwise it is called coarse-textured foam.

Foam flow in pipe has been regarded as a challenging topic, due to its complex structure and stability issues [1-3]. Although foam has been widely used in numerous applications, such as improved and enhanced oil recovery (I/EOR), drilling, cementing, liquid and solid removal, fracturing, and so on, there is still much room to improve the modeling, simulation, and analysis of relevant applications.

Foam Rheology Fundamentals

Experimental investigation of foam rheology can be classified into three main categories: using capillaries, rotational viscometers, and pipes. Although foam consists of two phases, some of the simple early-day approaches often considered it a homogeneous mixture with pre-specified density and viscosity based on experimental data. Foam viscosity slowly increases with foam quality, when foam quality increases up to roughly 70% (i.e., more bubbles means a higher possibility of bubble-to-bubble and bubble-to-wall interactions to increase foam viscosity). For foam quality roughly between 70% and 85%, foam viscosity dramatically increases with foam quality (i.e., not much space is available to avoid interactions any longer). For foam quality higher than a certain threshold value, around 86-92%, foam viscosity dramatically decreases with foam quality. Of course, these intervals are case- and material-specific, depending on pipe inclination, pipe diameter, roughness, injection pressure or flow rate, fluid properties, and so on [4, 5], but the general trend still seems valid. An accurate modeling of foams allows the reliable prediction of pressure drops, which is essential to proper facilities and pipeline design.

A good number of experimental studies show that foam can be modeled as a power-law fluid reasonably well, if the rheology at low shear rates is not of interest. For example, Sanghani and Ikoku [6] conducted foam flow experiments in the annulus with drill pipe (OD 1.5 in.) and casing (ID 4.5 in.), both about 28.5 ft long. The range of foam quality tested was from 0.65 to 0.95, and the shear rates ranged from 150 to 1000 sec^{-1}. The calculated foam effective viscosity was in the range of 60 to 500 cp. They formulated empirical equations for the effective foam viscosity as a function of foam quality by using a power-law model with parameters K and n. Foam flow characteristics also strongly depend on pipe diameter and the interaction between the pipe wall and flowing foam mixture. By conducting experiments in small pipes and capillary tubes, Mooney [7] found

that the presence of a wall significantly influences the flow behavior and, as a result, such a wall effect should not be neglected. Furthermore, they observed that a thin liquid layer forming at the pipe wall acts as a lubricant such that a relatively uniform foam core can slide on the liquid layer at the wall. This results in a lower-than-expected shear stress at a given shear rate, which, in turn, yields a lower-than-expected foam viscosity, due to wall slippage. Deshpande and Barigou [1] showed that the wall slip effect is more pronounced in small-diameter pipes/capillaries, where bubble size is comparable to the conduit diameter, and diminishes with pipe diameter. Sherif et al. [8] performed experiments in three 4-m parallel transparent pipe sections to investigate oil-based foam rheology with varying foam quality from 34%-68%. The base liquid was prepared by mixing mineral oil with diesel. Their results confirmed that the lubricating effect observed in aqueous foams was found to be consistent with oil-based foams.

Recent Approach with Two Flow Regimes

Recent experiments by Bogdanovic et al. [9] were conducted with two different pipe sizes (0.36 in. and 0.957 in. inner diameters, and lengths of about 12 ft) with nitrogen and various surfactants commonly used in drilling and completion. The pressure measurements along the pipe showed two different foam flow behaviors at fixed liquid velocity—a low-quality regime in which the pressure drop increases with increasing gas velocity, and a high-quality regime in which the pressure drop decreases with increasing gas velocity. Figure 1 shows similar experimental results obtained by Edrisi and Kam [10], where the threshold value of foam quality necessary to separate the two flow regimes was defined as f_g*. Gajbhiye and Kam [11, 12] further extended the experiments with visual cells in horizontal and inclined directions (i.e., 0^o, 45^o, and 90^o, both upward and downward). In addition to the size of bubbles in flowing foams, they visualized that the high-quality regime would show a slug flow pattern (i.e., repetition of free gas and fine-textured foams), and the low-quality regime shows plug flow pattern with homogeneous foam mixtures.

Edrisi et al. [13] conducted similar experiments to investigate the effects of oil and polymers. Although foam stability in the presence of oil and polymers added more complexity to the analysis, the presence of two distinct flow regimes was consistently confirmed. The threshold value of foam quality, f_g*, was shown to go down by adding oils, due to lower foam stability, and go up in the presence of polymers, due to higher water density and improved foam stability. Following those experimental studies that showed two distinct flow regimes, Edrisi and Kam [10] proposed a foam rheological model to capture the trend in the high-quality and low-quality regimes, as shown in Figures 2(a) and 2(b).

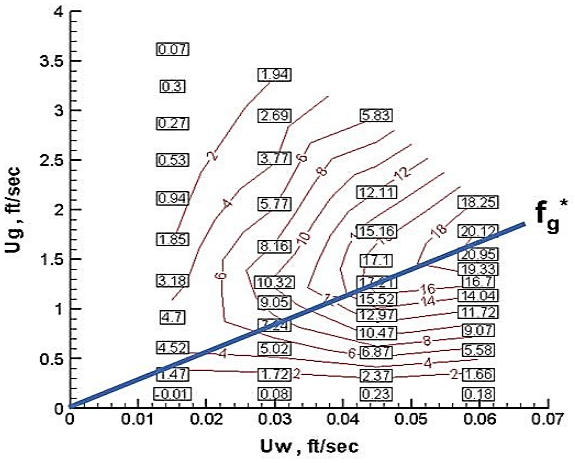

Figure 1. Experimental Data from Surfactant Foam Flow (0.5 wt% Stepanform and Nitrogen) Showing Two Flow Regimes Based on Pressure Drop Contours [10]

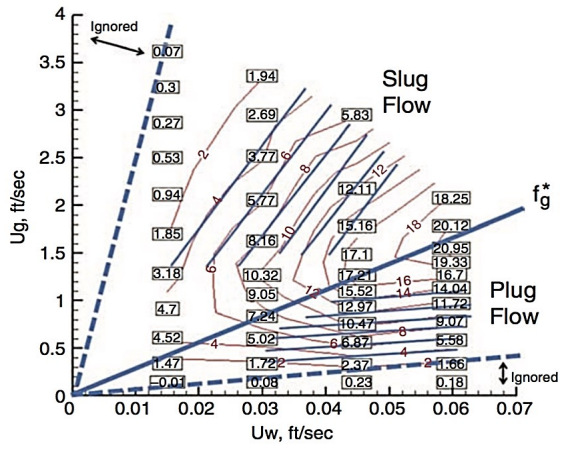

(a) Pressure Contours on the Original Data

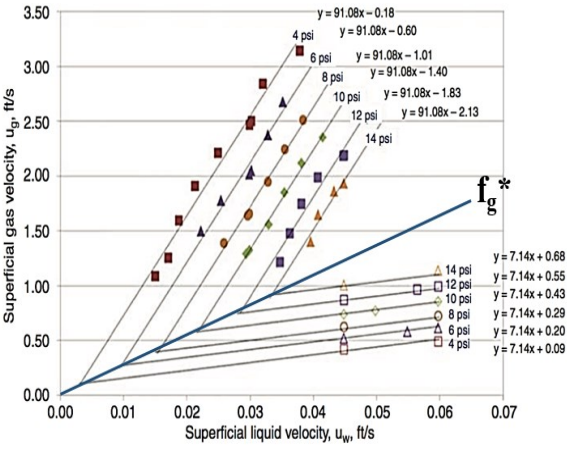

(b) Pressure Contour Map Reconstructed from the Model

Figure 2. Model Fit to Experimental Data [10]

As a first step, the model employed the power-law model along the f_g* line that required the consistency index, K, and power-law exponent, n, which can be determined based on the gap between pressure contours. The two representative slopes of the pressure contours in both regimes then defined how sensitive the pressure drop was to the liquid and gas velocities. These two families of parallel lines intersected at the f_g* line and, as a result the pressure contour map was approximated.

Motivation and Objectives

Although the previous modeling effort [10] captured the trend of pressure contours in both regimes, it left some significant shortcomings, as shown in Figure 3(a): (i) by defining foam rheology along the f_g* line, the model has essentially one type of foam rheology that is shared by both high-quality and low-quality regimes; (ii) for those pressure contours with relatively low values of pressure drops (for example, 2 psi), the model may crash with negative velocity values near the f_g* line; and (iii) the modeled pressure contours did not mimic the smooth transition between the two regimes, which is typically shown in the lab data.

The objective of this study was to develop a new foam model by improving the previous foam model of Edrisi and Kam [10] such that: (i) the model would have the ability to exhibit two different types of foam rheology independently in both regimes, and (ii) the model could handle a wide range of pressure and velocity conditions. The schematic of Figure 3(b) shows how these goals were achieved by introducing a reference point (u_{wRef}, u_{gRef}) in the pressure contour plot such that: (i) two types of foam rheology were defined separately along each of the lines (u_{wRef} = 0 and u_{gRef} = 0), and (ii) the smooth transition was made by interpolation to connect the contours of the two flow regimes. After showing the procedure for model fit, the authors also present how to extract other valuable properties during foam flow, such as foam viscosity, liquid-layer thickness at the wall, and friction factor to determine the frictional pressure loss during foam flow. As a final step, the robustness of this model is demonstrated from an example of a foam-assisted drilling process.

Methodology

Fundamentals of Foam Flow in Pipes

For a two-phase flow of water and gas (including foam), the total pressure drop, ΔP_t, consisted of three major components, as given in Equation (1):

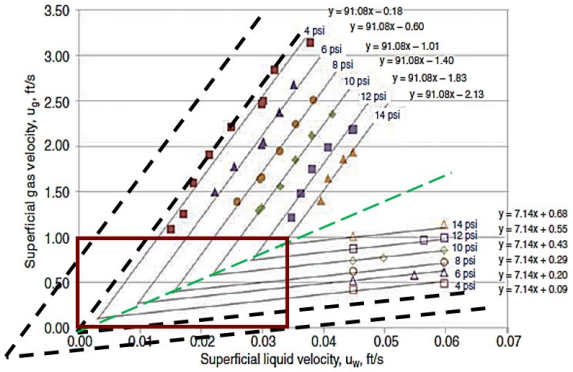

(a) Shortcomings of the Previous Work

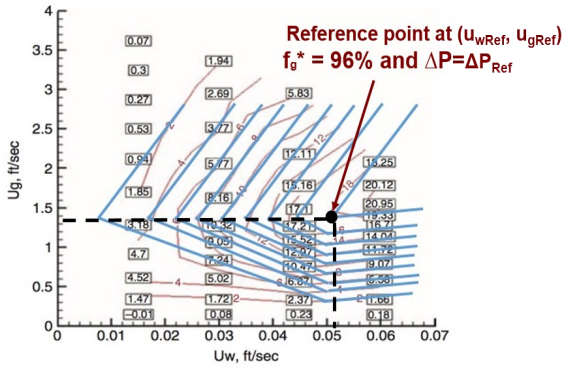

(b) Improved Model Introduced in This Study

Figure 3. Schematic Figures Comparing the Previous Model [10] and the New Model

$$\Delta P_t = \Delta P_h + \Delta P_a + \Delta P_f \quad (1)$$

where, ΔP_t is the total pressure loss; ΔP_h is the hydrostatic pressure loss; ΔP_a is the pressure loss due to acceleration; and ΔP_f is the frictional pressure loss.

The pressure drop due to acceleration is often neglected unless the cross-sectional area changes dramatically or the fluid is reactive. The hydrostatic pressure loss, ΔP_h (psi), can be expressed using Equation (2).

$$\Delta P_h = 0.052 \rho_m \quad (2)$$

where, ρ_m is the density of mixture (i.e., foams) [ppg].

The mixture density is commonly calculated using Equations (3) and (4):

$$\rho_m = \rho_g \left(\frac{Q_g}{Q_t} \right) + \rho_L \left(\frac{Q_L}{Q_t} \right) = \rho_g (f_g) + \rho_L (f_L) \quad (3)$$

$$Q_t = Q_g + Q_L \tag{4}$$

where, ρ_g, ρ_L are gas and liquid densities (ppg); f_g and f_L are gas and liquid flowing fractions; Q_t is the total flow rate (gpm); and Q_g and Q_L represent gas and liquid flow rates (gpm), respectively.

Unlike liquid density, the density of a highly compressible gas phase is a strong function of pressure and temperature, as shown by Equation (5):

$$\rho_g = \frac{PM}{ZRT} \tag{5}$$

where, P and T are pressure (psia) and temperature (R); M is the molecular weight (g/mol); R is the universal gas constant (J/mol.K); and Z is the compressibility factor.

The compressibility factor, Z, is also a function of pressure, temperature, and composition. The expression for the frictional pressure loss, ΔP_f, depends on flow rheology [14]. For Newtonian fluid in two-phase flow, Equation (6) is used if it is laminar flow, and Equation (7) if it is turbulent flow:

$$\Delta P_f = \frac{\mu_m v_m}{1{,}500 d^2} \tag{6}$$

$$\Delta P_f = \frac{f \rho_m v_m^{\ 2}}{25.8 d} \tag{7}$$

where, ρ_m and μ_m are mixture density (ppg) and viscosity (cp), respectively; d is pipe internal diameter (inches); v_m is the mean flow velocity (ft/sec); and f is dimensionless Fanning friction factor.

Note that for laminar flow, the Fanning friction factor is given by Equation (8):

$$f = \frac{16}{\mathrm{Re}} \tag{8}$$

For turbulent flow (smooth pipe), empirical Equations (9) and (10) can be used:

$$f = \frac{0.0791}{\mathrm{Re}^{0.25}} \tag{9}$$

$$\mathrm{Re} = \frac{928 \rho_m v_m d}{\mu_m} \tag{10}$$

where, Re is the dimensionless Reynolds number.

Note that the mixture viscosity, μ_m (cp) can be replaced by apparent foam viscosity, μ_{app} (cp) for non-Newtonian fluid, as shown in Equation (11):

$$\mu_{app} = 47900 \frac{\tau_w}{\dot{\gamma}_w} \tag{11}$$

where, τ_w is the wall shear stress [lbf/ft^2] and $\dot{\gamma}_w$ is wall shear rate (s^{-1}).

By using the hold-up of each of the phases (H_g and H_L for gas and liquid hold-up, respectively), the mean fluid velocity (v_m [ft/sec]) for flow in a pipe, which is simply total superficial velocity (u_t [ft/sec]), is expressed by Equation (12):

$$v_m = u_t = u_w + u_g = \frac{Q_t}{2.448 d^2} \tag{12}$$

where, u_g and u_w are superficial gas and liquid velocities (ft/s) and u_t is the total superficial velocity (ft/s).

Note that the wall shear stress, τ_w (lbf/ft^2), and wall shear rate, $\dot{\gamma}_w$ (s^{-1}), on the conduit walls can be expressed by Equations (13) and (14), respectively:

$$\tau_w = 3d \frac{\Delta P_t}{L} \tag{13}$$

$$\dot{\gamma}_w = \frac{96 u_t}{d} \tag{14}$$

where, L is the conduit length (ft).

Flow can be modeled by the power-law model, which was the case for this study; thus, the previous equations can be written as shown in Equations (15)-(17) (all units are the same as defined previously):

$$\tau_w = K \dot{\gamma}_w^{\,n} \tag{15}$$

$$\mu_{app} = K \dot{\gamma}_w^{\,n-1} \tag{16}$$

$$\Delta P_f = \frac{K v_m^n}{144000 d^{1+n}} \left(\frac{3 + 1/n}{0.0416} \right)^n \tag{17}$$

where, K is the consistency index and n is the power-law exponent.

Note that both K and n should be identified from experimental data. Fine-textured foam flowing in a pipe can be approximated by plug flow; that is, a foam core located at the center of the pipe and sliding on a lubricating thin liquid layer at the wall. Briceno and Joseph [2] suggested a simplified method for analyzing the system—as shown in Equation (18), from force balance in SI units:

$$\Delta P A = \tau_{wL} L S \tag{18}$$

where, ΔP is the pressure loss term; τ_{wL} is the shear stress within the liquid film; A is the cross-sectional area of the pipe; L is the length of the pipe (or, segment of interest); S is the perimeter of cylindrical foam core (that is concentric to the pipe); and LS represents the surface area of foam core over the length of L.

If the thickness of the liquid layer at the wall (δ_L) is very thin then the velocity gradient, dv/dy, or the equivalent shear rate, $\dot{\gamma}$, can be approximated by Newtonian flow using Equation (19):

$$\dot{\gamma} = \frac{\partial v}{\partial y} \approx \frac{u_t}{\delta_L} \tag{19}$$

where, Δv is velocity at the foam-liquid interface (i.e., velocity at the wall); Δy is distance to the foam-liquid interface, (i.e. distance to the wall); u_t is the velocity of foam core; and δ_L is the thickness of water film at the wall.

The shear stress in the liquid film (τ_{wL}) can be expressed by Equation (20):

$$\tau_{wL} = \mu_L \frac{u_t}{\delta_L} \tag{20}$$

where, μ_L is the liquid viscosity.

The liquid layer thickness, δ_L, can be written as shown in Equation (21):

$$\delta_L = \frac{S\mu_L u_t}{A\left(-\frac{\Delta P}{L}\right)} \tag{21}$$

For the friction factor of foam flow in a pipe, Equations (22)-(23) are used:

$$f = \frac{\tau_w}{\frac{1}{2}\rho_L u_t^2} \tag{22}$$

$$\tau_w = \frac{A\Delta P}{LS} \tag{23}$$

Note that the friction factor, f, is dimensionless, which later can be related to a dimensionless Reynolds number, as given in Equation (24):

$$\mathrm{Re} = \frac{\rho_L u_t A}{\mu_L S} \tag{24}$$

New Foam Model Proposed in This Study

Figure 4 shows the new foam model in this study has nine model parameters for capturing the flow behavior presented in the pressure contours constructed from laboratory flow tests in a wide range of gas and liquid velocities. There are three parameters for defining the reference point (i.e., u_{wRef}, u_{gRef}, ΔP_{Ref}), two parameters for capturing the trend of the linear slopes in the pressure contour lines in both high-quality and low-quality regimes (m_H and m_L), and two power-law model parameters for each of the two flow regimes (K_H, n_H; K_L, n_L). Note that the boundary between the high-quality and low-quality regimes, f_g*, is simply determined by other model parameters (i.e., $f_g^* = u_{gRef}/(u_{wRef}+u_{gRef})$.

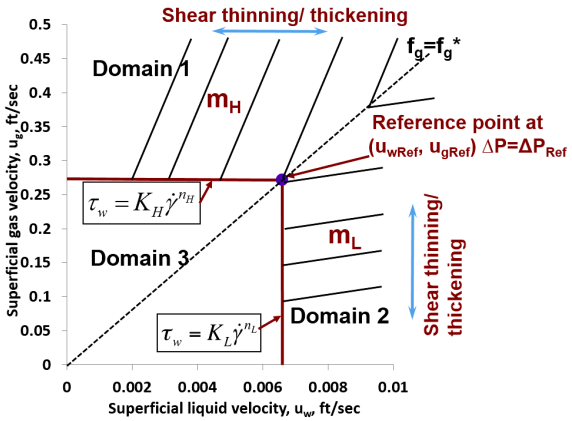

Figure 4. A Schematic Figure Showing Nine Parameters in This New Model (u_{wReg}, u_{gRef}, ΔP_{Ref}, m_H, m_L, K_H, n_H, K_L, n_L)

Suppose a series of laboratory flow tests are plotted in a form of pressure contours [see Figure 3(b)]. As a first step, a reference point, (u_{wRef}, u_{gRef}), is selected such that: (i) the rectangular area connecting (0, 0), (u_{wRef}, 0), (0, u_{gRef}), and (u_{wRef}, u_{gRef}) covers the range of the pressure contour map that needs to be treated by a smooth transition (this transition is named Domain 3 in Figure 4); and (ii) the point sits on the boundary between the two flow regimes [i.e., $f_g^* = u_{gRef}/(u_{gRef}+u_{wRef})$]. Note that the pressure contour corresponding to (u_{wRef}, u_{gRef}) is given by ΔP_{Ref}. The second step is to capture the trend of the linear pressure contours outside of Domain 3 in the high-quality regime (Domain 1 in Figure 4) and in the low-quality regime (Domain 2 in Figure 4). The pressure contours based on the original data [see Figure 3(b)] can be captured by a series of straight lines with average slopes; that is, m_H and m_L, the average slopes in the high-quality regime and low-quality regimes, respectively. Note that m_H is much larger than m_L, meaning that the pressure drop is sensitive to both gas and liquid velocities in the high-quality regime, while sensitive only to gas velocity in the low-quality regime.

The final step is to determine the foam rheology in each regime by using the power-law rheology model, which in some sense defines how a family of pressure contours are separated graphically in the contour plot; for example, if they are equally spaced, it implies that the rheology is near-Newtonian with an n value of around 1, while if the gaps between pressure contours grow or diminish with total velocity, u_t, the rheology is shear-thickening with an n greater than 1, or shear-thinning with an n less than 1, respectively. Among various possible options, this study used the horizontal line from (0, u_{gRef}) to (u_{wRef}, u_{gRef}) to determine the foam rheology in the high-quality regime [i.e., K_H and n_H

from Equation (15)], and the vertical line from (u_{wRef}, 0) to (u_{wRef}, u_{gRef}) to determine the foam rheology in the low-quality regime [i.e., K_L and n_L from Equation (15)]. The selection of these lines was somewhat arbitrary, but the use of the aforementioned lines helped maintain a small number of model parameters. It should be noted that, outside Domain 3, the boundary between the two regimes is primarily determined by n_H and n_L values—if they are the same, the line separating the two flow regimes tends to be straight; however, if one is greater than the other, the line is curved towards that domain.

As a result, this new model captured three domains (Domain 1, Domain 2, and Domain 3 for the high-quality regime, low-quality regime, and transition between the two, respectively) with a total of nine model parameters (u_{wRef}, u_{gRef}, ΔP_{Ref}, m_H, m_L, K_H, n_H, K_L, and n_L).

Model Fit to Pressure Contour Map

In order to demonstrate the procedure required for model fit, this study used experimental data from Edrisi and Kam [10]—see Figure 2(a) as an example—in which nitrogen and 0.5 wt% Stepanform surfactant solutions were injected into 0.38'' ID and 8.5 ft long stainless steel horizontal pipe. Figure 4 shows a schematic drawing to define and extract all nine model parameters.

First, the reference point (u_{wRef}, u_{gRef}) = (0.034 ft/sec, 0.93 ft/sec), and providing f_g* = 96.5%, was selected at ΔP_{Ref} = 14 psi, which allowed the rectangular box for Domain 3 to be determined. Then, a series of parallel pressure contours in both the high-quality and low-quality regimes were drawn from ΔP = 2 to 14 psi with the interval of 4 psi. The average slopes of these straight pressure contours were determined to be 90.0 and 7.0 for m_H and m_L, respectively. One may choose different pressure contours with different intervals, but it does not for this holistic approach. Figure 5 shows the results up to this point. As a next step, the power-law model parameters can be calculated from the relationship between the pressure drop and total velocity [K_H and n_H in Figure 6(a) for the high-quality regime along (0, u_{gRef}) to (u_{wRef}, u_{gRef}); K_L and n_L in Figure 6(b) for the low-quality regime along (u_{wRef}, 0) to (u_{wRef}, u_{gRef})].

The curve fit for the high-quality regime shows the following:

$$K_H = 0.1349 \frac{dyne - s^{1.2202}}{cm^2}$$

and

$$n_H = 1.2202$$

The curve fit for the low-quality regime shows the following:

$$K_L = 0.0027 \frac{dyne - s^{1.2074}}{cm^2}$$

and

$$n_L = 1.2074$$

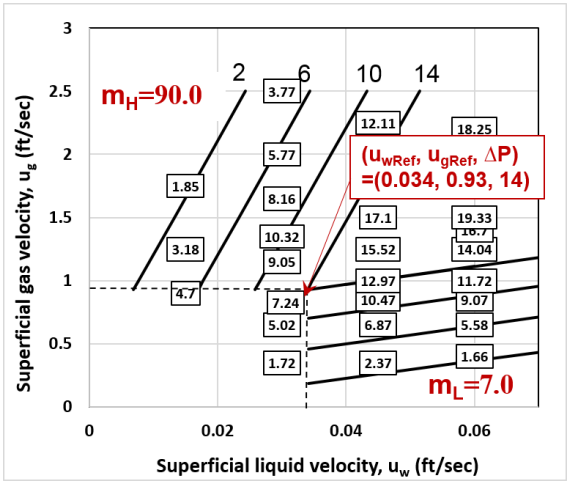

Figure 5. Schematic Showing the Model Parameters for the Reference Point, and the Average Slopes in the High-Quality and Low-Quality Regimes (1 ft/sec = 0.3048 m/s, 1 psi = 6894.7 Pa)

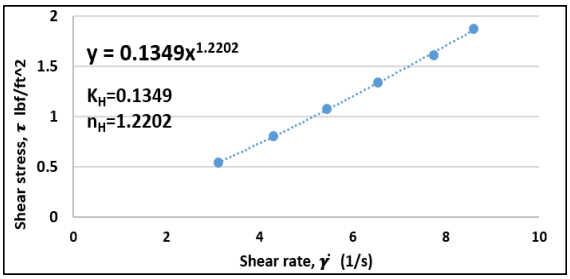

(a) K_H and n_H in the High-Quality Regime

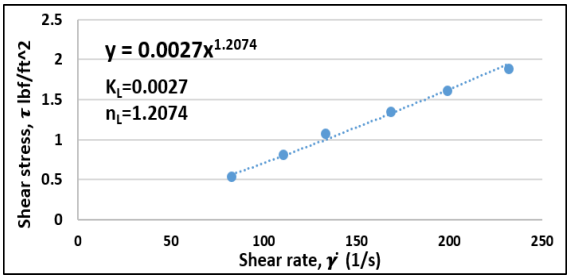

(b) K_L and n_L in the Low-Quality Regime

Figure 6. Rheograms Showing the Relationship between Shear Stress, τ, and Shear Rate, $\dot{\gamma}$ (1 lbf/ft^2 = 47.88 Pa)

Finally, Figure 7 shows Domain 3, where the transition can be completed by connecting pressure contours exhibiting the same values from both regimes. The figure also shows the boundary between the two flow regimes and one pressure contour beyond the reference point (ΔP = 18 psi). Table 1 shows a summary of all nine model parameters.

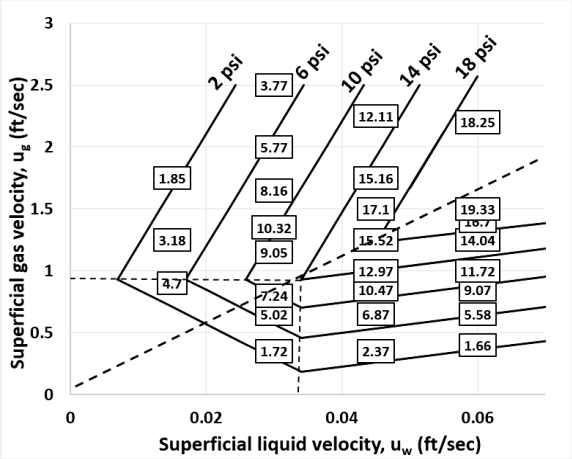

Figure 7. Schematic of a Complete Pressure Contour Map Showing Two Flow Regimes and a Transition Between Them (1 ft/sec = 0.3048 m/s, 1 psi = 6894.7 Pa)

Table 1. Summary of Nine Foam Model Parameters Determined in this Study to Fit Existing Laboratory Flow Test Data of Edrisi and Kam [10] (1 ft/sec = 0.3048 m/sec, 1 dyne/cm^2 = 0.1 Pa)

Parameters		Units	
u_{wRef}	Superficial liquid velocity at the reference point	0.034	ft/sec
u_{gRef}	Superficial gas velocity at the reference point	0.93	ft/sec
ΔP_{Ref}	Pressure drop at the reference point	14	Dimensionless
m_H	Average slope in the high-quality regime	90	Dimensionless
m_L	Average slope in the low-quality regime	7	Dimensionless
K_H	Consistency index in the high-quality regime	0.1349	$\frac{dyne-s^{1.2202}}{cm^2}$
n_H	Power-Law Exponent in the high-quality regime	1.2202	Dimensionless
K_L	Consistency index in the low-quality regime	0.0027	$\frac{dyne-s^{1.2074}}{cm^2}$
n_L	Power-Law Exponent in the low-quality regime	1.2074	Dimensionless

Implication of the Model for Other Flow Characteristics

Although this study first constructed pressure contours as a function of gas and liquid velocities, and then turned them into foam rheology using rheograms, some previous studies in the literature preferred using apparent foam viscosity for more practical purposes. By using Equations (12)-(16), one can plot apparent viscosity contours calculated by the power-law model, the results of which are shown in Figure 8. The filled square symbols represent the points at which actual pressure measurements are collected from the experiments and apparent foam viscosities are calculated. The position of the reference point is also shown by the filled circle.

Once the viscosity contours, ranging from 200 to 2200 cp, are constructed over a wide range of gas and liquid velocities of interest (see Figure 8), one may apply the map in order to estimate how foam viscosity varies during certain applications. For example, in foam drilling applications the process has relatively constant liquid velocities with gas velocities varying significantly due to compressibility. For three superficial liquid velocities in such an application (as shown by the vertical dotted lines for u_w = 0.02, 0.035, and 0.05 ft/sec in Figure 8), Figure 9 shows the apparent foam viscosities as a function of foam quality (i.e., varying u_g at fixed u_w). One may notice that the results from viscosity contours resemble the trend reported by previous studies—the foam mixture becomes more viscous with u_g for relatively wet foams, while less viscous with u_g for relatively dry foams. For foam stability, adding more gas to an already stable wet foam increases viscosity due to increasing bubble-to-bubble interactions during shear flow, while adding more gas to unstable dry foams decreases viscosity due to more active bubble coalescence.

For foams in the low-quality regime, the flow of a relatively homogeneous foam mixture allows the thickness of the liquid film at the wall to be determined using Equation (21) under the influence of a lubricating effect. In order to analyze how liquid-film thickness changes, 12 data points in the low-quality regime were selected, as shown in the contour map of Figure 10: four u_g values (u_g = 0.184, 0.46, 0.70, and 0.93 ft/sec) at each of three u_w values (u_w = 0.0341, 0.045, and 0.06 ft/sec), and with the reference point being point 1. Figure 11 shows how the liquid layer thickness corresponding to each point in Figure 10 is calculated by Equation (21). As expected, (i) at a fixed liquid velocity (u_w), the thickness of the liquid layer at the wall (δ_L) becomes thicker, as gas velocity decreases (or, as foam becomes wetter), and (ii) at a fixed gas velocity (u_g), the thickness of the liquid layer becomes thicker, as liquid velocity increases (or, as foam becomes wetter). It is interest-

ing to note that the reference point (point 1 in Figure 10) has the minimum δ_L, and the change in δ_L can be significant as foam becomes wetter (for example, δ_L increases from 0.001319 to 0.426 inches, an increase of almost 320 times, comparing point 1 to point 12).

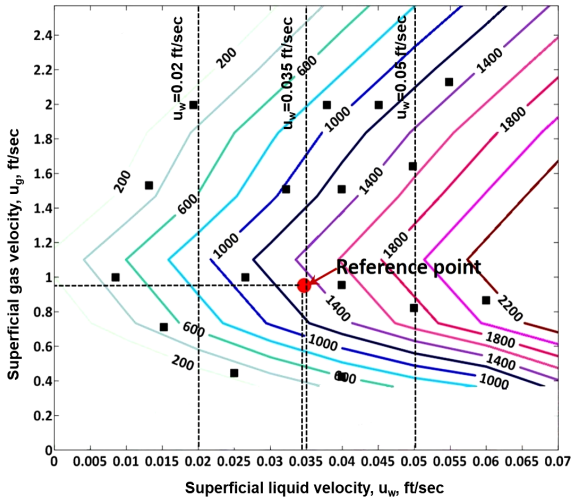

Figure 8. Conversion of Pressure Contours into Apparent Foam Viscosity Contours in cp as a Function of Gas and Liquid Velocities (1 ft/sec = 0.3048 m/s, 1 cp = 0.001 Pa s)

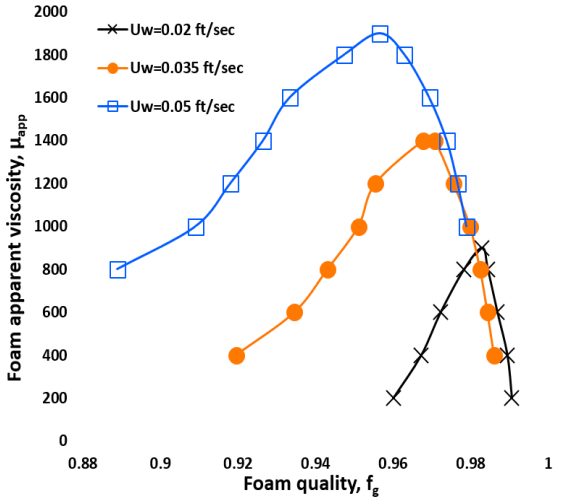

Figure 9. Apparent Foam Viscosity in cp Obtained at Fixed Superficial Liquid Rates with a Wide Range of Foam Qualities from 0.88 to 0.98, Following Figure. 8. (1 ft/sec = 0.3048 m/s, 1 cp = 0.001 Pa s)

In addition to pressure drop and apparent viscosity, the use of friction factor is sometimes handy for quantifying the flow of non-Newtonian fluids. The frictional pressure loss through the pipe depends on a number of parameters such as pipe diameter, density of fluid, viscosity of fluid, and average flow velocity, which are often grouped into a dimensionless Reynolds number [see Equations (22)-(24)]. For the 10 points from Figure 10 (excluding points 1 and 12), the frictional factor, f, for foams in the low-quality regime is plotted as a function of Reynolds number, Re, as shown in Figure 12. More specifically, the best-fit straight line equation in the log-log plot shows a relationship, determined by Equation (25):

$$f = \frac{0.1408}{\mathrm{Re}_L^{0.584}} \tag{25}$$

where, f is the foam friction factor and Re_L is the Reynolds number for low-quality foam.

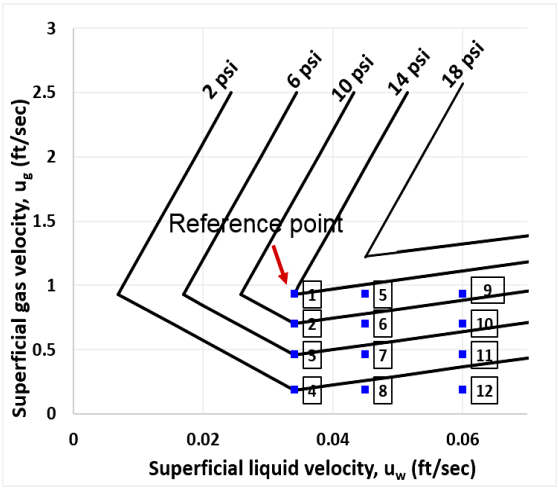

Figure 10. Schematic Showing 12 Data Points of Interest in the Low-Quality Regime at Three Fixed Liquid Flow Rates of 0.0341 ft/sec, 0.045 ft/sec, and 0.06 ft/sec (1 ft/sec = 0.3048 m/s, 1 psi =6894.7 Pa)

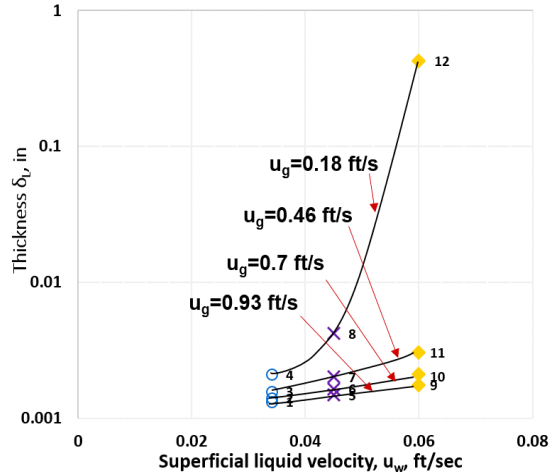

Figure 11. Liquid Layer Thickness at Three Different Liquid Injection Rates, 0.0341 ft/sec, 0.045 ft/sec, 0.06 ft/sec, and also Gas Injection Rates are 0.18 ft/sec, 0.46 ft/sec, 0.7 ft/sec, and 0.93 ft/sec, respectively (1 ft/sec = 0.3048 m/s; 1 in = 0.0254m)

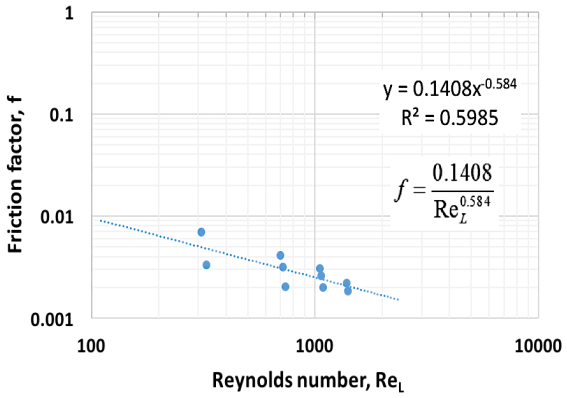

Figure 12. Relationship between Friction Factor and Reynolds Number for the Low-Quality-Regime Foams, Following Figure 10

It is interesting to note that the exponent is 0.584 [data points all in the laminar flow regime (Re_L < 2400), due to the high-viscosity foam mixture], which can be contrasted with 0.25 and 1 for turbulent and laminar flow of Newtonian fluid, respectively [see Equations (8)-(9)]. This deviation from the Newtonian fluid indirectly describes the complexity of foam flow behavior.

Application to the Foam Drilling Process

As an example application of this new model, a hydraulic foam drilling simulator was developed for this study. In the literature, there exist a few underbalanced hydraulic drilling simulators developed from steady-state to transient simulators. For comparison, this study used correlations from Chen et al. [15-16], who developed homogeneous foam rheology for polymer-stabilized foams, for the low-quality-regime foams, and it used correlations from Edrisi and Kam [17] for the high-quality-regime foams. Figure 13 shows a schematic of the drilling process with a U-tube concept for a 10,000 ft vertical well (i.e., drill string in the left-hand column and annulus in the right-hand column, both connected through bit nozzles at the bottom). The wellbore diameter was 8.5" (0.2159m), and the drill string outer diameter was 5" (0.127m). At the bottom hole, the bit was assembled using three nozzles with a diameter of 0.375" (0.009525m).

The direction of calculation is from the wellhead downward to the bottom hole for drill pipe flow, and then upward from the bottom hole to the top of the annulus for annulus flow. For calculation purposes, the wall roughness was assumed to be negligible, the surface temperature 80°F, the wellbore and fluid temperatures the same as the formation temperature (which had a gradient of 1.5°F/100 ft), the liquid-phase water, and the gas-phase nitrogen. The overall iterative calculations were carried out assuming a drilling pipe pressure (i.e., the pressure at the 1st node) that would satisfy the specified backpressure (i.e., the pressure at the 2Nth node, or 100 psia) at the given gas and liquid circulation rates (Q_g = 1300 scfm and Q_L = 40 gpm). The basic procedure is described as follows:

1. Figure 13 shows the construction of the computational U-tube domain for 2N cells for the drill string and annulus, with each node representing the center of each cell.
2. Specify the boundary conditions—the outlet pressure as well as gas and liquid rates.
3. Assume an inlet pressure at the 1st node.
4. For each cell in the drilling string, compute ΔP_a, ΔP_h, and ΔP_f, and then the total pressure drop, ΔP_t, in order to determine the pressure at the next node.
5. Between the N^{th} and $(N+1)^{th}$ nodes, there was a pressure drop through the drill bit, which is given by Equation (26):

$$\Delta P_{bit} = \frac{8.311\times10^{-5}\rho_m Q_t^2}{(0.95A)^2} \tag{26}$$

where, ρ_m is the mixture density (ppg); Q_t is the total flow rate (gpm); A is the total nozzle area (in^2); and, ΔP_{bit} is the pressure drop through nozzles (psig).

6. Similarly, continue the calculations upwards along the annulus for each node until the last node, 2Nth, is reached at the outlet.
7. Evaluate if the calculated pressure at the last node is close enough to the pre-specified backpressure. If not, go to step 3 with a new assumed value of inlet pressure and repeat the calculations; otherwise, accept it as a final solution.

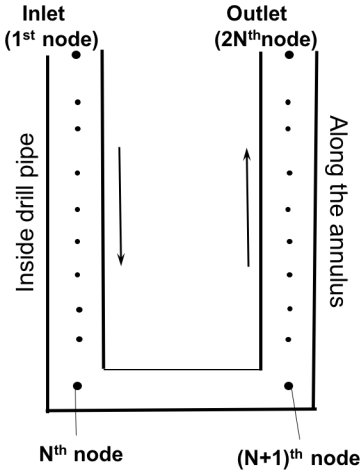

Figure 13. Schematic of the Foam Drilling Process Using the U-Tube Concept

Figure 14 shows the results of the foam drilling simulations in terms of pressure profile, foam quality, foam density, and total velocity for three different methods of modeling. First of all, it should be noted that Edrisi and Kam's model [10] cannot be used for low-circulation rates (see the discussion in Figure 3), due to the absence of a smooth transition. This is why relatively high Q_g and Q_L values were used for this simulation. Second, in all three methods, the pressure profile [see Figure 14(a)] shows the same back-pressure values of 100 psia (as an input) that corresponds to 0.97 of foam quality at the surface in the foam-quality profile [see Figure 14(b)], which determines foam density and total velocity along the hole [see Figures 14(c) and 14(d)]. Third, the results are in general consistent as expected. For example, foam quality decreases as pressure increases; foam density increases as depth increases; total velocity decreases as depth increases; etc. These results are primarily due to the compressibility of the gas.

Figure 14 reveals that: (i) the model based only on the low-quality-regime foams (referred to as "Chen et al." in dashed green lines) deviates significantly by missing unstable foam flow characteristics for dry foams, and (ii) even the model with two flow regimes (referred to as "Edrisi and Kam" in solid orange lines) shows the level of error that cannot be neglected by not incorporating the transition

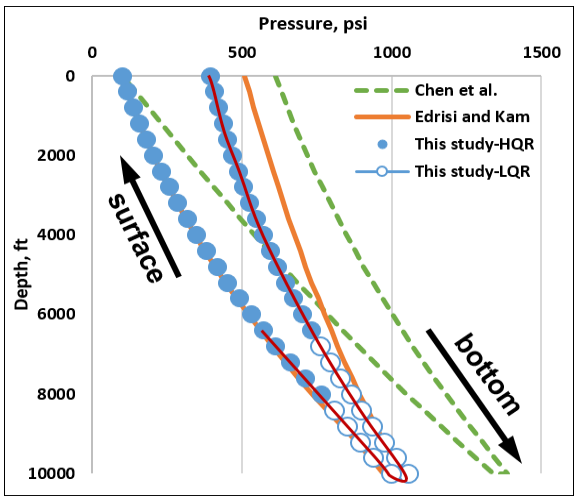

(a) Pressure

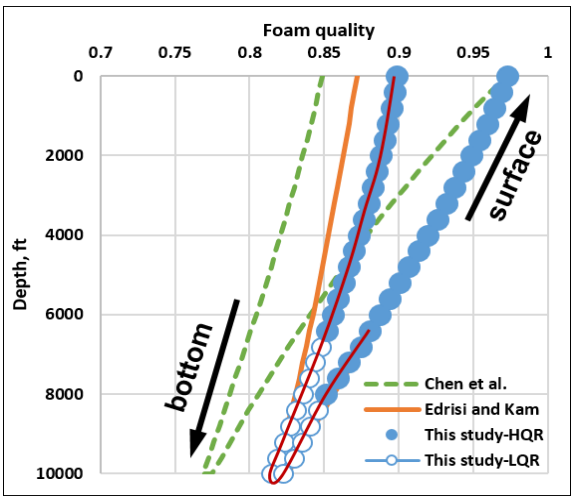

(b) Foam Quality

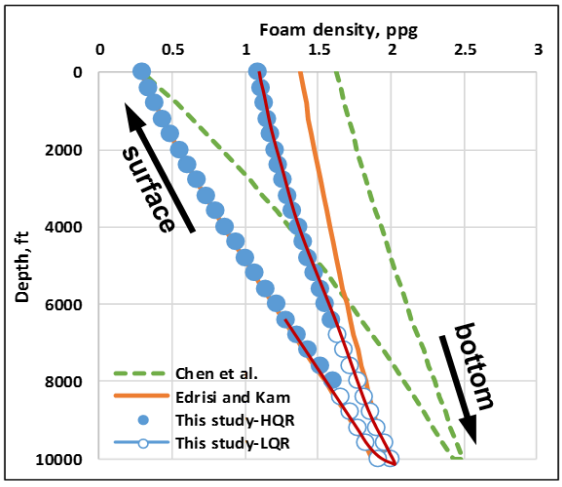

(c) Foam Density

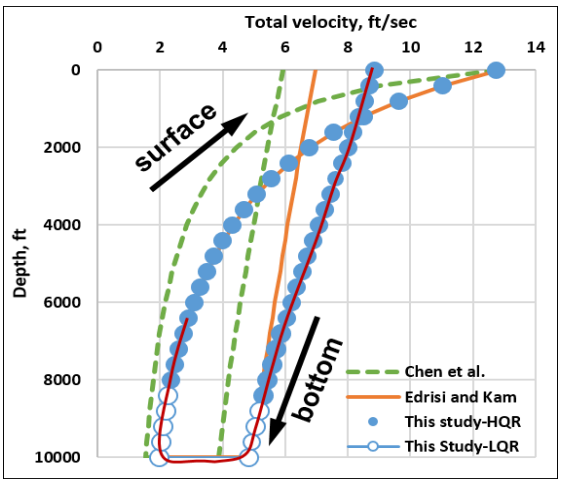

(d) Total Velocity

Figure 14. Steady-State Simulation Results for Foam Circulation without Formation Fluid Influx: (a) Pressure, (b) Foam Quality, (c) Foam Density, and (d) Total Velocity (The Portion with Dotted Lines on the Top of Circles Represents the Data Points Falling in Domain 3 (Transition)) (1 ft = 0.3048 m, 1 psi = 6894.7 Pa, 1 ppg = 119.8 kg/m^3)

(500 versus 400 psia at the inlet, 1.4 vs. 1.05 ppg foam density, and so on). Note that the results from the new model in this study are referred to as "This study" and represented by circles (i.e., open circles for $f_g > f_g^*$ and filled circles for $f_g < f_g^*$) and the dotted red lines on the top represent the portion of the graph in the transition (Domain 3). Table 2 summarizes the comparison of three different methods in terms of bottom hole pressure (BHP), bottom hole foam quality, bottom hole density, bottom hole total velocity, and injection pressure. The relative errors are shown as well.

Table 2. Comparison of Three Different Foam Simulation Methods (Chen et al. Only with Low-Quality-Regime Foams, Edrisi and Kam with Both Regimes but with no Transition, and This Model with Two Regimes as well as the Transition)

	This model	Chen et al.	Edrisi and Kam
BHP (psi)	996	1341 (26%)	973 (2%)
BH Foam Quality (%)	82	77 (6%)	83 (1%)
Inlet Pressure (psi)	395	611 (35%)	509 (22%)
BH Density (ppg)	1.91	2.43 (21%)	1.88 (2%)
BH Total Velocity (ft/s)	1.95	1.54 (26%)	1.99 (2%)

Conclusions

A new foam model was established in this study to characterize foam flow in pipes. The model incorporates unstable slug-flow-pattern dry foam rheology (referred to as the high-quality regime), stable plug-flow-pattern wet foam rheology (referred to as the low-quality regime), and a transition between the two. This study can be concluded with the following major outcomes. This new foam model overcomes the limitations in the previous model by: (i) allowing two separate and independent foam rheological properties in the high-quality and low-quality regimes, and (ii) introducing a smooth transition between the two regimes to capture experimental data more realistically. The model requires nine model parameters—three (u_{wRef}, $u_{gRef,}$ and ΔP_{Ref}) to define the transition region, four to capture power-law rheology in both high-quality and low-quality regimes (K_H, n_H, K_L, and n_L), and two to describe the sensitivity of steady-state pressure drops as a function of gas and liquid velocities in both regimes (m_H and m_L).

This study also demonstrates how some of the key parameters for foam flow in pipes can be decided. For example, how apparent foam viscosity can be mapped out in a wide range of gas and liquid velocities, how the thickness of water film at the wall (as an origin of lubricating effect) varies with changes in gas and liquid contents, and how the dimensionless friction factor, required for frictional pressure-loss calculations, can be calculated as a function of experimental conditions (which can be grouped into a Reynolds number). This new model was applied to foam drilling applications and compared with two other models from the literature—one was only based on low-quality regime foams, while the other was based on both high-quality and low-quality regime foams. The error analysis shows that there is a unique benefit of using the model presented in this study in predicting responses such as pressure, foam quality, foam densities, and total velocity. A more detailed analysis in a wide range of drilling scenarios remains as a future study.

References

[1] Deshpande, N. S., & Barigou, M. (2000). The flow of gas liquid foams in vertical pipes. *Chemical Engineering Science, 55*(19), 4297–4309.

[2] Briceno, M. I., & Joseph, D. D. (2003). Self-lubricated transport of aqueous foams in horizontal conduits. *International Journal of Multiphase Flow, 29*(2003), 1817-1831.

[3] Wang, J., Nguyen, A. V., & Farrokhpay, S. (2016). A critical review of the growth, drainage and collapse of foams. *Advances in Colloid and Interface Science, 228*(2016), 55-70.

[4] Xia, G., & Chai, L. (2012). Influence of surfactant on two-phase flow regime and pressure drop in upward inclined pipes. *Journal of Hydrodynamics, 24*(1), 39-49.

[5] Saxena, A., Pathak, A. K., Ojha, K., & Sharma, S. (2016). Experimental and modeling hydraulic studies of foam drilling fluid flowing through vertical smooth pipes. *Egyptian Journal of Petroleum, 26* (2017), 279-290.

[6] Sanghani, V., & Ikoku, C. U. (1983). Rheology of foam and implications in drilling and cleanout operations. *Journal of Energy Resource Technology, 105* (3), 362-371.

[7] Mooney, M. (1931). Explicit formulas for slip and fluidity. *Journal of Rheology, 2*(02), 210-222.

[8] Sherif, T., Ahmed, R., Shah, S., & Amani, M. (2015). Rheological behavior of oil-Based drilling Foams. *Journal of Natural Gas Science and Engineering, 26* (2015), 873-882.

[9] Bogdanovic, M., Gajbhiye, R. N., & Kam, S. I. (2009). Experimental study of foam flow in horizontal pipes: Two flow regimes and its implications. *Colloids and Surfaces A: Physicochemical and Engi-*

neering Aspects, 344(1), 56–71.
[10] Edrisi, A., & Kam, S. I. (2013). A new foam model in pipes for drilling and fracturing applications. SPE-162709-PA. *SPE Journal*, *19*(04), 576-585.
[11] Gajbhiye, R. N., & Kam, S. I. (2011). Characterization of foam flow in horizontal pipe by using two flow regime concept. *Chemical Engineering Science*, *66*(8), 1536–1549.
[12] Gajbhiye, R. N., & Kam, S. I. (2012). The effect of inclination angles on foam rheology in pipes. *Journal of Petroleum Science and Engineering, 86-87*(2012), 246-256.
[13] Edrisi, A., Gajbhiye, R. N., & Kam S. I. (2014). Experimental study of polymer-free and polymer-added foams for underbalanced drilling: Are two foam-flow regimes still there? SPE-162712-PA. *SPE Journal*, *19* (01), 55-68.
[14] Bourgoyne, Jr. A. T., Millheim, K., Chenevert, M. E., & Young, Jr. F. S. (1986). *Applied Drilling Engineering*. TX: Society of Petroleum Engineers.
[15] Chen, Z., Ahmed, R. M., Miska, S. Z., Takach, N. E., Yu, M., & Pickell, M. B. (2007). Rheology and Hydraulics of Polymer (HEC)-Based Drilling Foams at Ambient Temperature Conditions. SPE-94273-PA. *SPE Drilling & Completion*, *12*(01), 100–107.
[16] Chen, Z., Duan, M., Miska, S. Z., Yu, M., Ahmed, R. M., & Hallman, J. (2009). Hydraulic predictions for polymer thickened foam flow in horizontal and directional wells. *SPE Drilling & Completion, 24*(01), 40-49. SPE-105583-PA.
[17] Edrisi, A., & Kam, S. I. (2015). New foam drilling hydraulics calculations by using two foam flow regimes. SPE-174769-MS. SPE Annual Technical Conference and Exhibition, 28-30 September, Houston, Texas, U.S.A.

Biographies

YANFANG WANG is a PhD candidate in the Craft and Hawkins Department of Petroleum Engineering at Louisiana State University. She received her BS (2012) and MS (2014) degrees from the China University of Petroleum (Beijing) and the University of Louisiana Lafayette, respectively, both specialized in Petroleum Engineering. Her research interests include foam rheology behavior, underbalanced drilling, and liquid unloading simulations. Ms. Wang may be reached at ywan168@lsu.edu

CAITLYN THIBERVILLE is a doctoral candidate and research assistant in the Craft and Hawkins Department of Petroleum Engineering at Louisiana State University. She received her BS in Geology from the University of New Orleans in 2010, and, following her baccalaureate study, she gained professional experience primarily in the Marcellus and Eagle Ford Shale regions. Her research interests include subsea pipeline leak detection and multiphase flow in pipes. Ms. Thiberville may be reached at cthibe5@lsu.edu

SEUNG IHL KAM is the Donald W. and Gayle A. Keller Distinguished Professor in the Craft and Hawkins Department of Petroleum Engineering at Louisiana State University. He obtained his BS (1992) and MS (1994) degrees from Seoul National University in Energy Resources Engineering, and PhD degree (1998) from the University of Texas at Austin in Petroleum Engineering. His research interests include multiphase flow in porous media and pipes. Dr. Kam may be reached at kam@lsu.edu

A METHOD FOR PREDICTING THE RESULTS OF ACCELERATED ENGINE AIR FILTER TESTS BASED ON LIMITED DATA SETS

Kevin M. Hubbard, Missouri State University; Nebil Buyurgan, Missouri State University; Martin P. Jones, Missouri State University

Abstract

Accelerated filter life tests are expensive and time consuming. The goal of this study was to predict the results of these tests based on fewer data points. Pressure-drop data during accelerated life testing was collected on eight heavy duty engine air filters. The results of accelerated filter life tests may be predicted with sufficient certainty using third-order polynomials upon the collection of approximately 48% of the data required to perform the entire test at the maximum rated volumetric flow, when a test uncertainty ratio of 10:1 is required. If a test uncertainty ratio of 4:1 is required, a reduction of approximately 28% of data collection time may be achieved using third-order polynomials at the filter's maximum rated volumetric flow. The primary utility of the prediction method described in this paper lies in the area of new filter design.

Introduction

Engine air filters are classified as light duty or heavy duty. Light duty engine air filters are designed for use on internal combustion engines that produce low brake power (i.e., engine output power measured at the crankshaft). These filters experience a relatively low volumetric flow rate of air at the engine intake manifold, operate in relatively clean (i.e., on-road) environments, and are exposed to relatively fine dust contaminant particles. Heavy duty engine air filters are designed for use on engines that produce high brake power. These filters experience a relatively high volumetric flow rate of intake air and operate in relatively contaminated (i.e., off-road) environments in which they are exposed to coarse dust contaminant particles. Engine air filters are determined to have reached the end of their useful life when the pressure drop across the filter element exceeds some maximum value, as specified by the engine original equipment manufacturer (OEM). The period over which this occurs in service is typically measured in months of calendar time or hundreds of engine operation hours. For design and quality assurance purposes, the life of the filter is determined using an accelerated life test. These tests are conducted in accordance with the ISO 5011 standard: Inlet Air Cleaning for Internal Combustion Engines and Compressors—Performance Testing [1].

Accelerated life tests simulate the conditions experienced by the filter in service. Air flow, as measured by volumetric flow rate, is cycled at several levels between the maximum rated value and some minimum value, which is typically on the order of 20% of the rated air flow. As the air flow is varied, test dust is fed into the air upstream of the filter element. The rate at which the dust is fed is varied in order to maintain a constant dust contaminant concentration in the air stream [1]. The test dust is required to be in conformance with the ISO 5011 standard in terms of chemical composition and particle size distribution. At intervals during the test, the static pressure in the moving air stream is measured both upstream and downstream of the filter element being tested. The difference between the upstream and downstream static pressure measurements is known as "pressure drop." As dust is embedded in the filter medium and accumulates/agglomerates on the exterior surface of the filter medium, a "dust cake" is formed. As the mass of this dust cake increases, the pressure drop across the filter increases as well [2].

Accelerated filter life tests are expensive and time consuming. It is not uncommon to incur a cost of more than $10,000 per test. Testing times (to the end of filter life) are specified by the OEM and are often 20 to 30 hours or more. The calendar time consumed in conducting a 20-hour test, however, may be on the order of one week. The noise levels in the testing area are extremely high, resulting in operator fatigue. In addition, testing must be halted when temperature levels, relative humidity levels, or ambient barometric pressure levels become too high [1]. Temperature levels often increase in the testing area due to the operation of the equipment required to conduct the test. Design factors that influence the life of filters include the composition of the medium from which the filter is fabricated, the number, size, and distribution of pores in the filter medium, thickness of the medium, and geometry (height and spacing) of the pleats [3]. During initial filter design, the time required to vary one or more of these factors, produce a new prototype filter, and conduct an accelerated life test to determine the viability of the new design may be months.

Because of these considerations, large time and cost reductions may be achieved if the results of an accelerated filter life test can be predicted after a shorter period of test-

ing time. In this paper, the authors present a method for predicting the results of an accelerated filter life test using a limited data set.

Pressure Drop as a Function of Time

Since pressure drop is the criterion for filter life, it is useful to understand how it changes as a function of time. Darcy's law [2] is given in Equation (1):

$$\Delta P = \Delta P_f + \Delta P_c \tag{1}$$

where, ΔP is the total pressure drop across the filter medium and dust cake; ΔP_f is the pressure drop across the clean filter medium; and, ΔP_c is the pressure drop across the dust cake.

Darcy's law, which is valid for both flat and pleated filters, may be written as Equations (2)-(4):

$$\Delta P_f = K_1 V_f \tag{2}$$

$$\Delta P_c = K_2 V_f \frac{M}{A} \tag{3}$$

$$\Delta P = K_1 V_f + K_2 V_f \frac{M}{A} \tag{4}$$

where, K_1 is the filter resistance coefficient; K_2 is the dust cake resistance coefficient; V_f if the face velocity of air at the point of filter medium entry; M is the mass of dust deposited on the filter medium; and, A is the area of filter medium exposed to air flow.

The filter resistance coefficient depends on the physical characteristics of the filter medium, such as pore size, pore distribution, medium material, and medium thickness. The dust cake resistance coefficient depends on the packing efficiency of the dust cake, and dust particle size and distribution. Endo et al. [4] stated Equation (5):

$$\Delta P_c = 18 \mu V_f T \frac{(1-\alpha)\{\nu(\alpha)\}}{\alpha^2} \frac{\kappa}{d_{vg}^2 e^{4\ln^2 \sigma_g}} \tag{5}$$

where, T is the thickness of the dust cake; μ is the dynamic viscosity of the gas being filtered; $\nu(\alpha)$ is the void function; κ is the dynamic shape factor for the dust particles; α is the average porosity of the dust cake layer; d_{vg} is the volume equivalent diameter of the dust particles; and, σ_g is the standard deviation of the particle equivalent diameter of the dust particles.

The dynamic shape factor, κ, is set to unity for particles that are spherical in shape. The void function, $\nu(\alpha)$, accounts for dust cake agglomeration and acts as a modifier on the dynamic viscosity, μ, of the gas being filtered. Endo et al. [4] modified Darcy's law as Equations (6)-(8):

$$\nu(\alpha) = \frac{10(1-\alpha)}{\alpha} \tag{6}$$

$$\Delta P = K_1 V_f + 180 \mu V_f T \frac{(1-\alpha)^2}{\alpha^3} \frac{\kappa}{d_{vg}^2 e^{4\ln^2 \sigma_g}} \tag{7}$$

$$\alpha = 1 - \frac{M}{\rho T A} \tag{8}$$

where, ρ is the density of the individual dust particles.

In the formulation of Equation (4), mass is the only variable quantity if face velocity is held constant. In addition, mass is the only variable quantity in the formulation embodied by Equations (7) and (8). Thus, in either of the two formulations presented here, the total pressure drop across a filter that is loaded with dust is directly related to the mass of dust embedded in and agglomerated on the filter medium. It has been shown [3] that pleated filters typically exhibit three dust loading stages: depth filtration, in which dust particles lodge within the filter medium; cake filtration, in which a dust cake develops on the surface of the filter medium; and, a final dust cake build-up stage. As a result, the curve that depicts pressure drop as a function of time exhibits a discontinuity. The curve that corresponds to the first two dust loading stages tends to be linear while the curve that corresponds to the final dust loading stage tends to be exponential in form.

Experimental Design and Testing

Figure 1 shows a schematic of the test setup. Air enters the system through an ideal flow nozzle that promotes laminar flow. The air stream passes by a dust feeder, which dispenses dust at a metered rate into the air stream. The dust employed for the tests described here conformed to the ISO 5011 standard requirements for accelerated life testing. Pipes having an inside diameter of 4.500 inches were attached to the inlet and exit of the filter housing. Piezometer rings were incorporated into these pipes both upstream and downstream from the filter housing. Pressure sensors were attached to these piezometer rings, and the difference in reading between the upstream and downstream piezometer rings results in the pressure drop across the filter being tested. In addition, the pressure drop across the filter being tested was also monitored using a water-type U-tube manometer. The air stream velocity was measured using a fan-style

averaging anemometer as well as hot-wire anemometers. Ambient pressure, temperature, and relative humidity were also monitored using digital instruments. Data acquisition hardware and software was used to obtain data from the digital instruments.

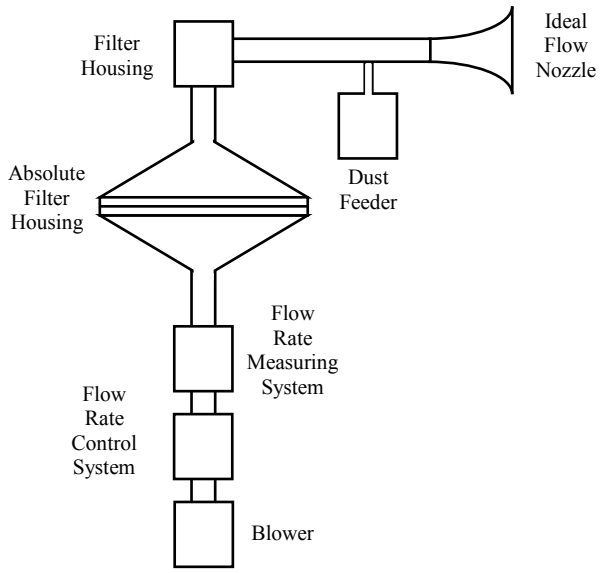

Figure 1. Schematic of the Filter Accelerated Test Setup

Coarse grade test dust was used to conduct the dust capacity tests. Coarse dust was fed at a rate of 0.025 grams per cubic foot of air. Volumetric flow rate, and therefore the dust feed rate, were altered according to the schedule specified in the ISO 5011 standard. Test parameters were changed at ten-minute intervals and were repeated once per hour of elapsed test time. Table 1 details the volumetric flow and dust feed rates during the dust capacity test.

Table 1. Volumetric Flow Rate Variation Cycle

Time Period (minutes)	Volumetric Flow Rate (cubic feet per minute)	Dust Feed Rate (grams per minute)
0	420	10.5
10	252	6.3
20	84	2.1
30	336	8.4
40	252	6.3
50	168	4.2

The volumetric flow rates detailed in Table 1 represent 100%, 60%, 20%, 80%, 60%, and 40% of the maximum rated volumetric flow rate of the filter, as specified by the ISO 5011 standard.

Data Analysis and Results

Data on eight heavy duty engine air filters with 100% cellulosic media were collected. These filters were pleated with an average pleat depth of 1.700 inches, and a 12-inch longitudinal height. Each filter incorporated 250 pleats, resulting in a face area of 72.2 ft^2. Twenty pressure drop readings (one reading per hour) were recorded for each volumetric flow rate. The 252 cfm volumetric flow rate was repeated twice each hour; however, each replication was considered separately. Eight filters were evaluated to statistically verify that those filters belonged to the same population. The behavior of each filter was analyzed individually and that behavior was compared with each of the other filters to confirm that all filters behaved similarly at each volumetric flow rate. Figure 2 depicts the pressure-drop versus time curves for all of the filters tested at a volumetric flow rate of 420 cfm. The pressure-drop curve exhibited by each of the filters was very similar to that of each of the other filters; however, random variations in filter media, pleat geometry, screen mesh geometry, changing ambient environmental conditions, and other random physical factors resulted in a varying initial pressure drop from one filter to the next.

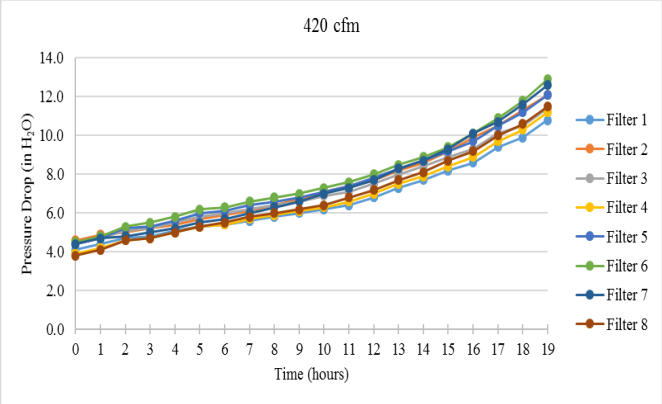

Figure 2. Pressure-Drop versus Time Curves for Filters at a Volumetric Flow Rate of 420 cfm

To eliminate the effects of varying initial pressure drop, the curves were translated so that the initial pressure drop was set to an ideal value of zero. This was a hypothetical case that represents perfect filter performance. Figure 3 represents the translated curves corresponding to those depicted in Figure 2. The translated data obtained from each filter were then compared with the data obtained from each of the other filters using paired t-tests with 95% confidence intervals [5]. In general, confidence intervals vary depending on specific applications [6, 7]. A total of 28 pairwise comparisons were conducted. The comparison results indicated that there were no statistical differences between filter performances at different volumetric flow rates, except for the

84 cfm volumetric flow rate, which was the lowest rate in the experiment. Based on the analysis, the hypothesis of pressure drops for filters having the same means could not be rejected for higher volumetric flow rates. However, the results were inconclusive for the lowest volumetric flow rate. The reason for varying results at 84 cfm was that the data for all tests were collected using electronic equipment. It was likely that some electromagnetic noise was present in the ambient environment during testing, which resulted in a small signal-to-noise ratio, due to the fact that the pressure drop at this very low volumetric flow rate was exceedingly small. Data collected at the larger flow rates were not susceptible to this electromagnetic noise. According to the ISO 5011 standard, all final reported pressure-drop determinations used to determine the end of filter life must be made at the maximum rated volumetric flow rate. As a result, the results of these initial analysis were considered acceptable.

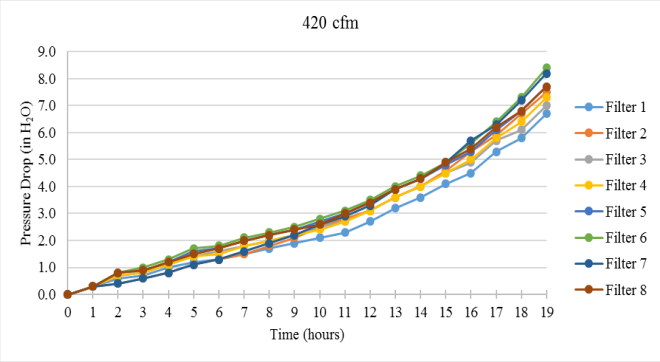

Figure 3. Pressure-Drop versus Time Curves after Translation

A polynomial regression analysis was performed using pressure-drop data for each filter [8]. Second- and third-order polynomial curves were formulated using the first i data points at each volumetric flow rate, where $i = 1 \ldots 20$. The independent variable was time and the dependent variable was the pressure drop measured in inches of water (in H_2O). Pressure-drop equations, as functions of time at each volumetric flow rate for each filter, were generated. The final data point (at a time of 19 hours) was predicted using the polynomial curves, and prediction errors were calculated. After this process, the earliest data were determined where the error rate was smaller than an acceptable tolerance.

When determining an acceptable tolerance, the prediction needed be no more accurate than the measurement uncertainty. In this case, the measurement uncertainty is essentially the resolution of the measurement instrument. An analog pressure transducer was employed and the signal from this electronic pressure transducer was monitored using a PC-based data acquisition card (DAC). The measuring system resolution was calculated as range/2^n, where n is the number of bits of memory dedicated to the DAC, and range is the range of measurement of the sensor. The pressure sensor had a range of 15 psia with an output of 0-5 VDC. The DAC allowed only bipolar ranges (in this case -5 VDC to +5 VDC). As a result, the resolution of the measuring instrument was (15 psia × 2)/2^{12} = 0.0073 psia.

Supported by the ANSI/NCSL Z540-1 standard, the 10:1 and 4:1 ratios are two test uncertainty ratios (TUR) commonly adopted and used in industry [9]. Therefore, these two ratios were used to calculate measurement uncertainty. According to the *TUR* rules, collective measurement uncertainty should not exceed 10% and 25% of the acceptable tolerance, respectively. These rules can be formulated as shown in Equation (9) [10]:

$$TUR = \frac{Acceptable\ Tolerance\ Rate}{2\left(Measurement\ Uncertainty\right)} \tag{9}$$

where, TUR = 10 for 10:1 and TUR = 4 for 4:1 ratios.

Acceptable tolerances were calculated for each *TUR* using the resolution of the measurement instrument as measurement uncertainty. For 10:1 *TUR* it was (10)(2)(0.0073) psia = 0.146 psia or 4.06 in H_20, and for 4:1 *TUR* it was (4)(2)(0.0073) psia = 0.0584 psia or 1.62 in H_2O. For example, the second-order polynomial curves for filter 1 at 420 cfm, using the first 14 data points, was determined to be $\Delta p = -0.0038t^2 + 0.1682t + 4.2457$, where t represents time expressed in hours and Δp represents pressure drop (in H_2O).

The end of test prediction (at 19 hours) was -0.0038(19^2) + 0.1682(19) + 4.2457 = 8.8308 in H_2O. The actual recorded data at 19 hours was 10.8 in H_2O; therefore, the error in the prediction was (10.8-8.8308) = 1.9692 in H_2O. This error is acceptable, based on 10:1 *TUR* (1.9692 < 4.0587) but not acceptable for 4:1 *TUR* (1.9692 > 1.6235). As a result, if a second-order polynomial curve, which is formulated using pressure-drop data recorded during the first 14 hours of testing, is employed to predict the pressure drop at 19 hours, the prediction will be acceptable for 10:1 *TUR*; therefore, testing can be stopped and predicted values can be used. This provides savings of six test hours. However, for 4:1 *TUR*, the test should be continued. It is clear that the prediction errors decrease as the number of data points used to generate the polynomial curves increase. However, the goal was to find the least number of data points that would result in an acceptable prediction. Additionally, third-order polynomial curves provided lower prediction errors. Figures 4 and 5 present the average number of saved test hours at each volumetric flow rate using second- and third-order polynomial curves for 10:1 *TUR* and 4:1 *TUR*.

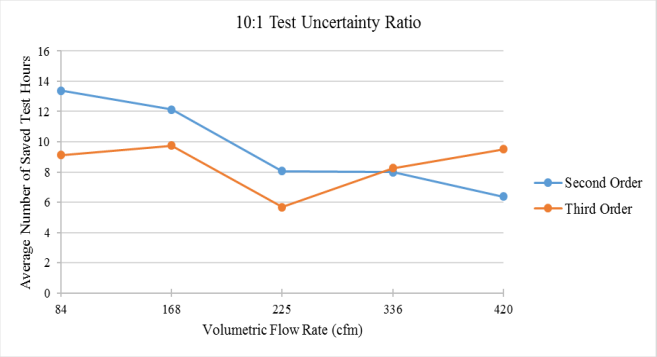

Figure 4. Average Number of Saved Hours for 10:1 *TUR*

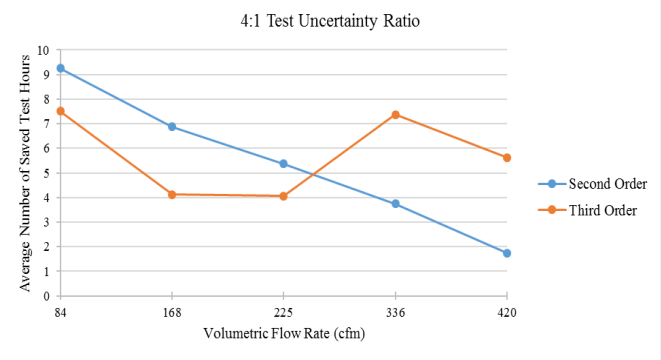

Figure 5. Average Number of Saved Hours for 4:1 *TUR*

As seen in these figures, and regardless of 10:1 *TUR* or 4:1 *TUR*, the number of saved test hours decreased as the volumetric flow rate increased, when second-order polynomial curves were used for flow prediction. These savings were as high as 13 hours, which is more than half of the test time at 84 cfm for 10:1 *TUR*. There is no apparent correlation between time savings and volumetric flow rate when third-order curves are used.

Conclusions

In this paper, the authors presented a method by which the results of accelerated air filter life tests can be predicted, based on a limited data set. Accelerated filter life tests are expensive and time consuming. Using the method described in this paper, the expense incurred to conduct these tests may be significantly reduced. In addition, the development cycle for new filter designs may be reduced as well. The major utility of the method presented here is for filter design testing, rather than for the testing of filters in production. The results of accelerated filter life tests may be predicted with sufficient certainty using third-order polynomials upon the collection of approximately 48% of the data required to perform the entire test at the maximum rated volumetric flow, when a test uncertainty ratio of 10:1 is required. If a test uncertainty ratio of 4:1 is required, a reduction of approximately 28% of data collection time may be achieved using third-order polynomials at the filter's maximum rated volumetric flow. The primary utility of the prediction method described in this paper lies in the area of new filter design. When performing process testing for production quality control purposes, it is likely that entire tests must be performed. When designing new filters, however, the primary goal is to ascertain whether one new design shows more promise than another. For these types of comparative purposes, the method described in this paper may be employed.

The method for modeling pressure drop as a function of time and dust loading rate, which has been presented in this paper, was validated using experimental data collected from heavy duty engine air filters. The method shows promise, however, with regard to other filtration applications, including high-efficiency particulate (HEPA) air filters such as those used in medical applications [3], which also dealt with the modeling of pressure drop as a function of time. There is evidence that the pressure-drop versus time function exhibits a discontinuity. At earlier data collection times, the curve tended to be linear, while at later data collection times, the curve tended to exhibit a polynomial relationship. Future research should be conducted that focuses on modeling the pressure-drop versus time curve at times later than the time at which the discontinuity occurs.

References

[1] International Organization for Standardization. Inlet air cleaning equipment for internal combustion engines and compressors -- Performance testing. (ISO 5011:2014). Retrieved from https://www.iso.org/standard/64762.html

[2] Cheng, Y. H., & Tsai, C. J. (1998). Factors influencing pressure drop through a dust cake during filtration. *Aerosol Science and Technology*, *29*(4), 315-328.

[3] Joubert, A., Laborde, J. C., Bouilloux, L., Chazelet, S., & Thomas, D. (2011). Modelling the Pressure Drop across HEPA Filters during Cake Filtration in the Presence of Humidity. *Chemical Engineering Journal*, *166*(2), 616-623.

[4] Endo, Y., Chen, D.-R., & Pui, D. Y. H. (1998). Effects of particle polydispersity and shape Factor during dust cake loading on air filters. *Powder Technology*, *98*(3), 241–249.

[5] Montgomery, D.C., & Runger, G. C. (2014). *Applied Statistics and Probability for Engineers*. Hoboken, NJ. Wiley and Sons.

[6] Mahfouz, T., & Jones, J. (2013). An ordered probability framework for assessing markup values for the

construction industry. *International Journal of Engineering Research and Innovation, 5*(1), 53-61.
[7] Thamma, R. (2010). Comparison of regression models to study the effect of turning parameters on surface roughness. *International Journal of Engineering Research and Innovation, 2*(2), 80-86.
[8] Montgomery, D.C., & Runger, G.C. (2014). *Applied Statistics and Probability for Engineers*. Hoboken, NJ. Wiley and Sons.
[9] Bennett, K., & Zion, H. (2005). Metrology concepts: understanding test uncertainty ratio (TUR), White paper for Transcat Calibration and Repair, Inc. Retrieved from http://www.transcat.com/media/pdf/TUR.pdf
[10] Hogan, R. (2014). How to calculate test uncertainty Ratio. Retrieved from http://www.isobudgets.com/calculate-test-uncertainty-ratio/

Biographies

KEVIN M. HUBBARD is an assistant professor of technology and construction management at Missouri State University. He earned his BS degree (Aerospace Engineering, 1991) from the University of Missouri–Rolla; MS (Engineering Management, 1993) from the University of Missouri–Rolla; and PhD from the University of Missouri–Rolla (Engineering Management, 1996). Dr. Hubbard is currently teaching at Missouri State University. His research interests include automation and device control, manufacturing systems, device design, and process optimization. Dr. Hubbard may be reached at KHubbard@MissouriState.edu

NEBIL BUYURGAN is an associate professor of technology and construction management at Missouri State University. He earned his BS degree (Industrial Engineering, 1998) from Istanbul Technical University, Turkey; MS (Engineering Management, 2000) from the University of Missouri–Rolla; and PhD from the University of Missouri–Rolla (Engineering Management, 2004). Dr. Buyurgan is currently teaching at Missouri State University. His research interests include optimization of logistics operations in manufacturing, healthcare, military and retail, and supply chain management. Dr. Buyurgan may be reached at NebilBuyurgan@MissouriState.edu

MARTIN P. JONES is an associate professor of technology and construction management at Missouri State University. He earned his BS degree (Physics, 1981) from the University of Maryland, Baltimore County; MS (Materials Science and Engineering, 1984) from the Johns Hopkins University; and PhD (Materials Science and Engineering, 1987) from the Johns Hopkins University. Dr. Jones is currently teaching at Missouri State University. His research interests include scanner technology, nondestructive evaluation, manufacturing processes, and quality assurance. Dr. Jones may be reached at MartinJones@MissouriState.edu

IDENTIFICATION AND CONTROL OF HIV DRUG THERAPY USING FUZZY SYSTEMS

Samir Talssi, University Hassan II; Noura Yousfi, University Hassan II

Abstract

In this paper, the authors present a tool for decision support based on fuzzy logic that can provide effective decision support in HIV infection treatment. The approach relies on modeling the changes of viral load and CD4+ T-cell counts during treatment in a fuzzy system. The obtained fuzzy system is used in treatment control. The therapy state can be presented by four parameters: uninfected cells (x), infected cells (y), infectious virus (vi), and noninfectious virus (vni). Two drugs are used in the HIV infection therapy: drug 1 is used to block new infections of CD4+ T-cells, while drug 2 is used to inhibit viral production. If $u1$ and $u2$ are, respectively, the quantities of drug 1 and drug 2 used, a question that summarizes the purpose and motivates the work presented in this paper is, How can the parameters $u1$ and $u2$ be adjusted in order to reduce the viral load for a given state (x, y, vi, and vni)? Practicing doctors use their expertise to answer that question. In this paper, the design of a fuzzy system and fuzzy identification of an HIV infection therapy is introduced. A clustering method was used to determine the basic parameters of the fuzzy system. The results of the simulation are also presented.

Introduction

In an antiviral drug treatment of HIV infection, the CD4+ T-cell count and viral load can be used as an indicator of success or failure of treatment. With regular monitoring of viral load, doctors can detect resistance to treatment and adapt the treatment protocol. The errors or accuracy in screening tests play a precious role in improving treatment protocols. Recently, automated screening tests have been created to monitor viral load in real time. Screening tests are able to detect a very low viral load in patients infected with AIDS, offer one of the highest degrees of sensitivity, and allow doctors to use their experience and expertise to make the right treatment decision. The current question is, How to make the exploitation of the massive information flow more effective? One solution is to introduce a calculation tool that takes into account the data processing and the doctor's knowledge. Fuzzy logic has much to offer in the realm of uncertainty and imprecision [1]. The therapy can by identified using a fuzzy system, and the obtained fuzzy system can be used to control the therapy with the control parameters $u1$ and $u2$.

The Fuzzy System

The HIV infection therapy can be presented by a MIMO system with six inputs, $X \in U \subset \mathbb{R}^6$, and four outputs, $Y \in V \subset \mathbb{R}^4$, where X = (x, y, vi, vni, $u1$, and $u2$) and Y = (x, y, vi, and vni). This MIMO system is described by a set of measured input/output data collected during treatment. Fuzzy modeling and identification from measured data are effective tools for approximating uncertain non-linear systems. Babuska et al. [2] identified the multiple-input, multiple-output (MIMO) systems by means of product-space fuzzy clustering with adaptive distance measures (the Gustafson-Kessel algorithm). The MIMO model is represented as a set of coupled input/output MISO models of the Takagi -Sugeno type. Usually, a fuzzy system, S, can be defined using Equation (1):

$$(S): U \subset \mathbb{R}^n \rightarrow \mathbb{R}^m \tag{1}$$

where, U is a compact in $\mathbb{R}^n$.

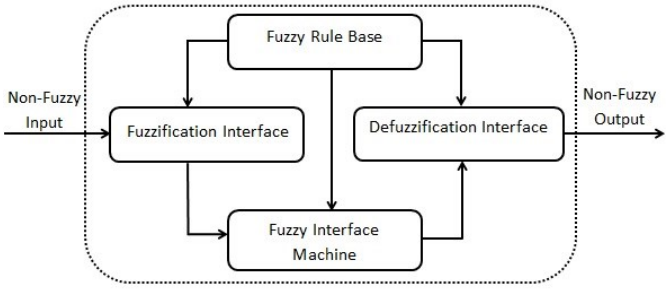

Figure 1. Basic Configuration of the Fuzzy System

Figure 1 presents a basic configuration of the fuzzy system. A fuzzy system typically consists of four elements: fuzzification interface, fuzzy rule base, fuzzy interface machine, and defuzzification interface. A fuzzification interface plant from an entries space, $U \subset \mathbb{R}^n$, is a fuzzy subsets space defined on U. Note that a fuzzy set A is defined on $U \subset \mathbb{R}^n$ by the membership function of Equation (2):

$$\mu_A : U \rightarrow [0,1] \tag{2}$$

The fuzzy rule base is a set of fuzzy rules R_j of type IF-THEN. The fuzzy IF-THEN rule is a conditional statement expressed by Equation (3):

$$R_j : \text{IF } x_1 \text{ is } A_1^j \text{ and } x_2 \text{ is } A_2^j \text{ and } \ldots \text{ and } x_n \text{ is } A_n^j \text{ then } y_1 \text{ is } B_1^j \text{ and } y_2 \text{ is } B_2^j \text{ and } \ldots \text{ and } y_m \text{ is } B_m^j \quad (3)$$

where, $j = 1, 2, \ldots, m$, and x_i ($i = 1, 2, \ldots, n$) is the i[th] component of the fuzzy system input vector; y_i ($i = 1, 2, \ldots, m$) is the i[th] component of the fuzzy system output vector; and, A_i^j and B_i^j and are fuzzy subsets characterized by the membership functions $\mu_{A_i^j}$ and $\mu_{B_i^j}$, respectively.

A fuzzy interface machine is the core of a fuzzy system, which combines the information obtained from the fuzzification interface with the rule base and conducts the fuzzy reasoning process. In the defuzzification interface, the output of the fuzzy system (a numerical decision) is computed [3].

Design of a Fuzzy System Using Data

Construction of fuzzy models involves selecting several parameters: the position, shape, and distribution of the membership functions; building the rules basis; selection of logical operations; and, the consequences of the rules. These may be estimated from data using different strategies, where the goal is to minimize the approximation error between the output values and the computed values using the fuzzy model. Several strategies have been proposed in the literature for designing a fuzzy system using data: Table Lookup Scheme [4], Gradient Descent [4, 5], Clustering method [6], and Evolutionary Strategies [7].

In this paper, a clustering strategy is used to determine fuzzy system parameters. The most commonly used fuzzy clustering methods include: fuzzy C—means method, Gustafson and Kessel algorithm [8], mountain clustering [9], and subtractive clustering [10]. The methods based on clustering are considered to be data-driven methods. The main idea of these methods is to identify structures (clusters) among the data according to their distribution in space and assimilate each cluster into a multidimensional fuzzy set representing a rule. The subtractive clustering method is an extension of the mountain clustering method that was introduced by Yager and Filev [9]. In the subtractive clustering method, there is no need to determine the number of clusters at the beginning.

Note that the input data are defined on $U \subset \mathbb{R}^n$, and the output data are defined on $\mathbb{R}^m$, as in Equation (1). Two steps were used here to construct a fuzzy system: The data were normalized and grouped using the subtractive clustering method. The fuzzy system explicit expression for a data couple (X,Y) is the weighted mean, as shown in Equation (4):

$$y_i = f(X) = \frac{\sum_{j=0}^{l} y_i^j \mu_{B_i^j}(X)}{\sum_{j=0}^{l} \mu_{B_i^j}(X)} \quad i = 1,2,\ldots,m \quad (4)$$

where, y_i^j is the center of the group B_i^j related to the values of variable Y_i (these groups were generated in the first step) and the integer l represents the number of rules.

The membership function, $\mu_{B_i^j}$ of B_i^j, is defined by Equations (5) and (6):

$$\mu_{B_i^j}(X) = \max_{i=1\ldots n}\left(\mu_{A_i^j}(X)\right)$$
$$\mu_{A_i^j}(X) = \sum_{i=0}^{i=n} e^{-\alpha\left\|X - X^i\right\|^2} \quad (5)$$

$$X^j = \left[x_1^j, x_2^j, \ldots, x_n^j\right] \quad (6)$$

where, x_i^j is the center of the group A_i^j ($i = 1, 2, \ldots, n$) related to the values of X (these groups were generated in the first step using the subtractive clustering method); the integer l is the number of groups A^j; and, the constant α is defined in the subtractive clustering method [10].

According to Oviedo et al. [11], the fuzzy systems of Equation (4) can approximate any function in a compact domain. The accuracy of the approximation depends on the maximum slope of the function and the distance between the centers of the fuzzy sets. Lee [12, 13] demonstrated that the fuzzy system presented in step 2 is a universal control tool.

Fuzzy Identification of HIV Infection Therapy

The HIV infection drug therapy can be described by an iterative MIMO system; the entries of this system at time k are the variables cited previously (x_k, y_k, vi_k, vni_k, $u1_k$, and $u2_k$)and the outputs are (x_{k+1}, y_{k+1}, vi_{k+1}, and vni_{k+1}). A mathematical model using the same variables was presented by Hattaf and Yousfi [14]. In that model, a semi-implicit finite difference method was used to reach the solutions. A fuzzy system describing this therapy can be defined using Equation (7):

$$F : X_i \in \mathbb{R}^6 \mapsto Y_i \in \mathbb{R}^4 \quad (7)$$

where, $X_i = (x_i, y_i, vi_i, vni_i, u1_i,$ and $u2_i)$ and $Y_i = F(X_i) = X_{i+1}$

Because of the unavailability of real data, the input-output data, or the couples (X_i,Y_i), needed to determine the fuzzy system parameters were generated using a semi-implicit finite difference method introduced by Hattaf and Yousfi [14]. Figure 2 shows a fuzzy system that can be used as an inverse fuzzy controller. It takes the next desired state (x_{i+1}, y_{i+1}, vi_{i+1}, and vni_{i+1}) as an input and calculates the decision ($u1_i$, $u2_i$) which allows for this state. In other words, given the current state of the infection (x_i, y_i, vi_i, and vni_i), the doctor's concern is to determine the values of $u1_i$, and $u2_i$, that lead to the next desired state (x_{i+1}, y_{i+1}, vi_{i+1}, and vni_{i+1}). The simulation results presented in the next section give more information about the construction of the fuzzy system and illustrate its applications.

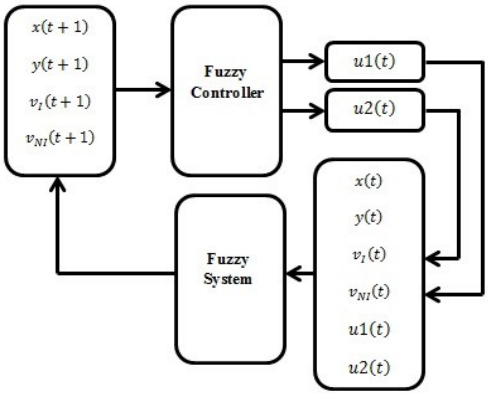

Figure 2. Fuzzy Inverse Controller

Simulation

In the first step, the semi-implicit finite difference method (SIFDM) [14] was implemented in order to generate a set of one hundred couples of data (X_i,Y_i). The data represent the behavior of the therapy presented by these data. The data were normalized using Equation (8) [15], which allows values between HI (= 0.9) and LO (=0.1).

$$x \leftarrow \big((x - min)/(max - min)\big) * (HI - LO) + LO \qquad (8)$$

In the second step, the normalized data were grouped using the subtractive clustering method. The clustering method resulted in the generation of 18 groups. Finally, the fuzzy system, described in Equation (4), was built according to the centers of these groups. Figures 3-11 represent a comparison between the results of the semi-implicit finite difference method and those of the obtained fuzzy system. It is clear from these figures that the fuzzy system reproduces the same behavior as that of SIFDM. Introducing a control parameter and using the least-squares method to remove the acceptable error that appears in these results will help increase the accuracy of results.

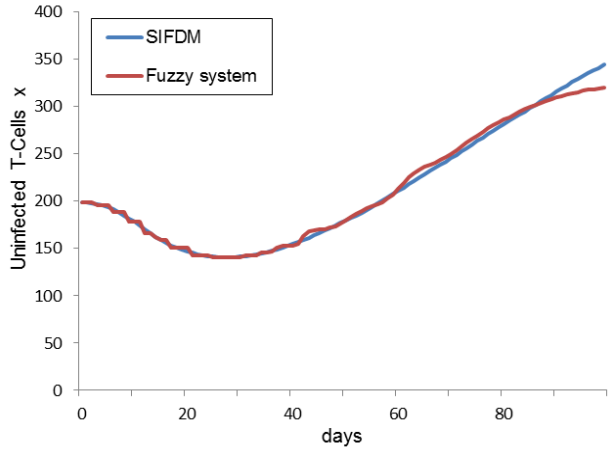

Figure 3. Changes in the Number of Non-infected Cells during Therapy

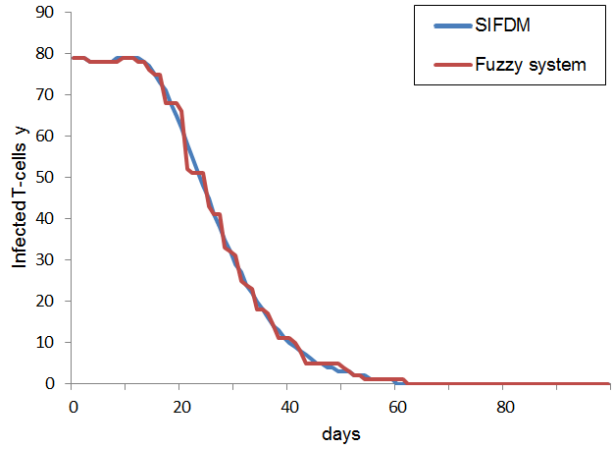

Figure 4. Changes in the Number of Infected Cells during Therapy

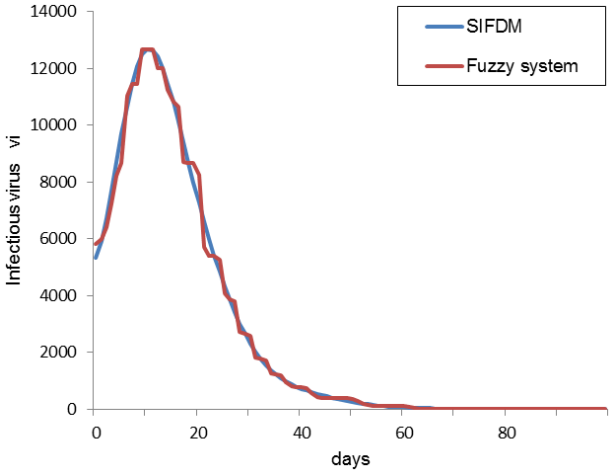

Figure 5. Changes in the Infectious Viral Load during Therapy

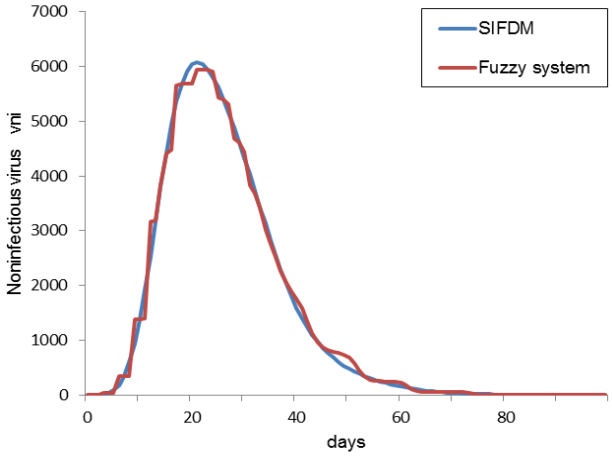

Figure 6. Changes in the Non-infectious Viral Load during Therapy

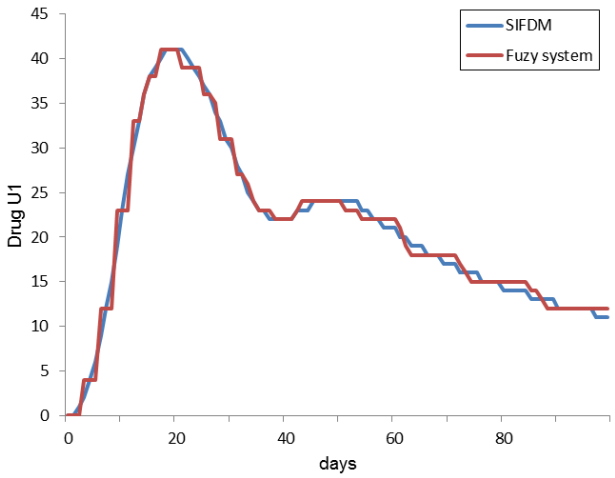

Figure 7. Changes in the Drug Quantity of *u*1 during Therapy

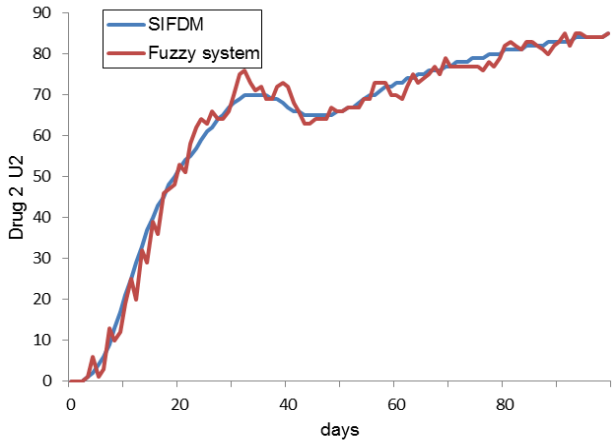

Figure 8. Changes in the Drug Quantity of *u*2 during Therapy

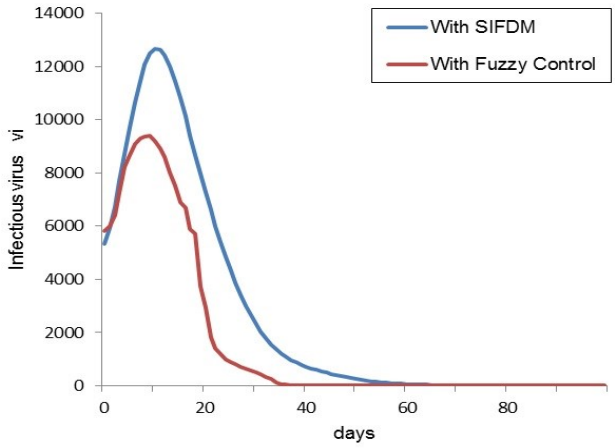

Figure 9. Changes in Infectious Viral Load during Therapy

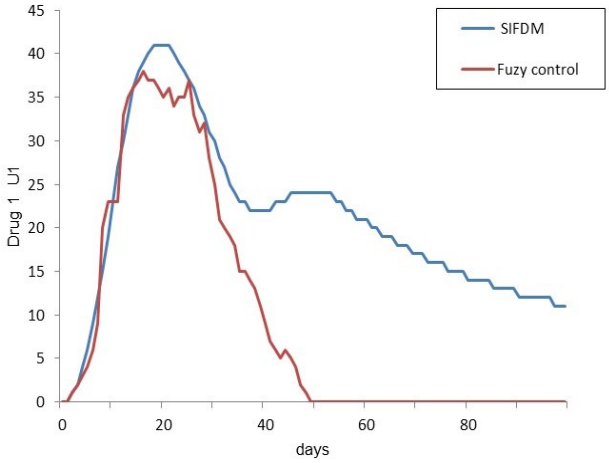

Figure 10. Changes in the Drug Quantity *u*1 during Therapy

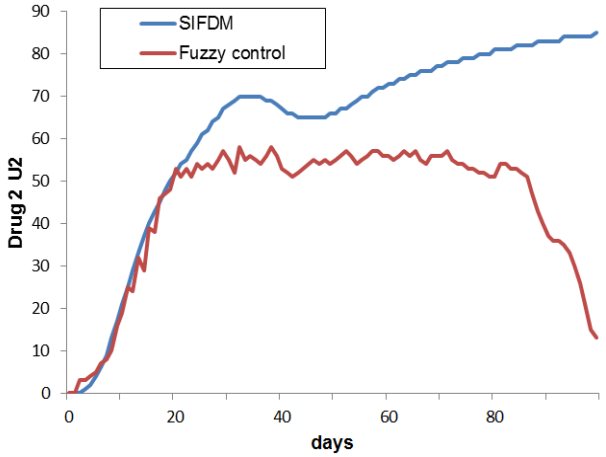

Figure 11. Changes in the Drug Quantity *u*2 during Therapy

Figure 9 shows a comparison between the controlled behavior of v_i and the one given by the SIFDM. The obtained control parameters are presented in Figures 10 and 11.

Conclusions

The introduction of new clinical decision support in the area of drug treatment of viral infections is currently is a requested feature. Fuzzy logic offers an outstanding method to intuitively manage complex systems. The input-output data collected during the treatment of this type of infection encapsulate the expertise of the doctor and behavior of the virus. The doctors' expertise is the set of decisions that were taken during treatment in different situations. From these data, a fuzzy system can identify the behavior of the virus infection against the drug treatment and, at the same time, identify the infection behavior related to the doctors' expertise. The simulation results motivate researchers to test this tool on real data processing different viral infections, and verify its applicability in real life.

References

[1] Celikyilmaz, A., & Turksen, I. B. (2009). Modeling uncertainty with fuzzy logic. *Studies in fuzziness and soft computing*, *240*.

[2] Babuska, R., Roubos, J. A., & Verbruggen, H. B. (1998, May). Identification of MIMO systems by input-output TS fuzzy models. *In Fuzzy Systems Proceedings, IEEE World Congress on Computational Intelligence*. The 1998 IEEE International Conference (v1, pp. 657-662).

[3] Cox, E., O'Hagan, M., Taber, R., & O'Hagen, M. (1998). *The Fuzzy Systems Handbook with Cdrom*. Academic Press, Inc.

[4] Wang, L. X. (1994). *Adaptive fuzzy systems and control: design and stability analysis*. Prentice-Hall, Inc.

[5] Jang, J. S. (1992). *Neuro-fuzzy modeling: architectures, analyses, and applications*. University of California, Berkeley.

[6] Gomez-Skarmeta, A. F., Delgado, M., & Vila, M. A. (1999). About the use of fuzzy clustering techniques for fuzzy model identification. *Fuzzy sets and systems, 106*(2), 179-188.

[7] Bodenhofer, U. (1996). *Tuning of fuzzy systems using genetic algorithms*. na.

[8] Krishnapuram, R., & Kim, J. (1999). A note on the Gustafson-Kessel and adaptive fuzzy clustering algorithms. *IEEE Transactions on Fuzzy Systems*, *7* (4), 453-461.

[9] Yager, R. R., & Filev, D. P. (1994). Generation of fuzzy rules by mountain clustering. *Journal of Intelligent and Fuzzy Systems, 2*(3), 209-219.

[10] Chiu, S. (1997). Extracting fuzzy rules from data for function approximation and pattern classification. *Fuzzy Information Engineering: A Guided Tour of Applications*. John Wiley & Sons.

[11] Oviedo, J. J. E., Vandewalle, J. P., & Wertz, V. (2006). *Fuzzy logic, identification and predictive control*. Springer Science & Business Media.

[12] Lee, C. C. (1990). Fuzzy logic in control systems: fuzzy logic controller. *IEEE Transactions on Systems, Man, and Cybernetics*, *20*(2), 419-435.

[13] Lee, C. C. (1990). Fuzzy logic in control systems: fuzzy logic controller. *IEEE Transactions on Systems, Man, and Cybernetics*, *20*(2), 419-435.

[14] Hattaf, K., & Yousfi, N. (2012). Two optimal treatments of HIV infection model. *World Journal of Modelling and Simulation*, *8*(1), 27-35.

[15] Talssi, S., & Yousfi, N. (2014). Optimality identification in epidemiology using neural networks. *Proceedings of the 2014 IAJC-ISAM International Conference*.

Biographies

SAMIR TALSSI is a professor at higher institutes of applied engineering IGA-Casablanca. His areas of interest include artificial intelligence and its applications in epidemiology. Talssi was a member of the High Council Education in Morocco and has over 10 years of experience as manager and educator. Professor Talssi may be reached at samirtalssi@gmail.com

NOURA YOUSFI is currently a professor in the Department of Mathematics and Computer Science in Mohammedia Hassan II University. She is the director of several doctoral student research projects. Dr. Yousfi has over 20 years' of experience as a scientist, manager, and teacher. She is also a biomathematics specialist. Dr. Yousfi may be reached at nourayousfi@hotmail.com

RFID-BASED HIGHWAY SIGN PREVENTIVE MAINTENANCE SYSTEM

Ghanshyam Bhutra, Texas A&M University College Station; Dr. Ben Zoghi, Texas A&M University College Station;
Dr. Paul Carlson, Texas A&M Transportation Institute

Abstract

Road sign maintenance is a critical job, typically executed by the state department of transportation. In the state of Texas alone the estimated economic loss of all motor vehicles between 2003 and 2015 amounts to $24.6 billion. Although not all motor accidents are related to road signs, their importance in maintaining traffic safety is not arguable. The maintenance of these signs is a manual- and labor-intensive task and is error prone. There is extensive use of radio frequency identification (RFID) technology in toll collection systems on highways. In a typical RFID system, the tags or transponders are mobile, and the reader is stationary. There are a few successful applications in the literature that use a portable reader and a fixed tag. In this current study, a system that assists the operator in checking the road signs was developed. The system uses GPS to predict the incoming road sign, and combined with RFID detection, verify the presence of a road sign at a particular geo-location. This work leverages the concept of the Internet of things to provide an all-around connected system of individual components working harmoniously to achieve a goal.

Introduction

The concept of RFID has been around for several decades [1]. Highway toll collection, ID cards, asset tracking in retail and departmental stores, and countless other applications have this technology at their core. With new technological paradigms like ubiquitous computing, the Internet of things, and cloud computing, this technology is evolving to generate better and better-connected new applications to make our lives easier.

The foundational premise of RFID is communication using reflected power or modulated backscatter. The RFID reader transmits an unmodulated radio signal from the connected antenna; this signal powers up the transponder or tag circuitry and sends back a radio signal modulated with the information stored in its memory. Figure 1 shows a typical setup with two parts to an RFID system. One part is the RFID reader connected to a power source along with a processor and an antenna. The other part is a radio frequency transponder, also known as a tag, which serves as the information source.

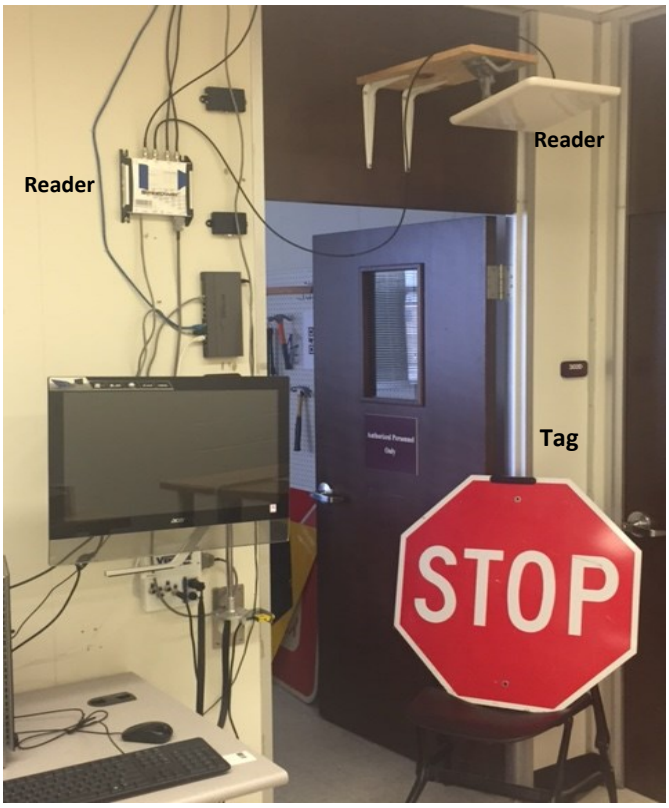

Figure 1. A Typical RFID System

Modern manufacturing techniques have reduced the size of RFID tags considerably, resulting in a significant drop in production costs. And, as the jacket around the circuitry can be designed to suit the environment, its operational life is extended substantially. One of the most useful aspects of an RFID system is that it requires little to no maintenance, as the tags themselves are passive, meaning that they do not require a power source. In most RFID systems, the reader is stationary, but there are studies in the literature that explore a portable reader and stationary transponder design. Lee et al. [2] showed the design considerations of installing an omnidirectional antenna on a moving vehicle. They demonstrated that the tags could be detected well above highway speeds. Ning et al. [3] used an RFID system with the reader on a vehicle to locate the vehicle in real-time by integrating RFID, GPS, and GPRS technologies. This work also used a system in which the tags or transponders were stationary, and the reader was in motion inside a vehicle.

The intended use of this current study was to outfit road maintenance vehicles with an intelligent system that would automatically track, monitor, and log the condition of road signs, as the support car drives along, through the use of an RFID-based system. The system also utilizes GPS to verify and predict incoming signs. The system continuously checks for road signs in a circular area centered at the real-time coordinate of the vehicle. Using the present and some past coordinates of the vehicle, the system evaluates the orientation of the vehicle and predicts an incoming sign. As the vehicle approaches a given sign, the RFID system detects the tag attached to the sign and gives the operator confirmation if the tag was successfully read. If the system does not detect the RFID tag attached to the sign, at the particular coordinate, the system prompts the user about the missing or damaged sign in real-time. The software logs a list of tags that were successfully read, as well as missing or damaged ones, into a report at the end of a maintenance run. This allows the maintenance worker to drive along the road without having to manually record any data or stop and get out of the vehicle, considerably reducing the time required to complete a job. The reports are synchronized into the cloud to allow tracing of the maintenance cycles and perform analytics for optimization.

Road Signs and Maintenance

Motor vehicle safety is of paramount importance. In a recent report by the World Health Organization [4], road injuries killed 1.3 million people in 2015. In the state of Texas alone, the average estimated economic loss of all motor vehicle crashes between 2003 and 2015 is $24.6 billion [5]. According to the 2015 annual report by the Texas Department of Transportation [6], there is a fatality every 2 hours and 29 minutes; an injury every 2 minutes and 8 seconds; and a reportable crash occurring every 61 seconds, due to motor vehicle accidents. These staggering numbers clearly show the critical nature of road safety to human lives.

Road signs are located at specific locations to maintain smooth traffic flow without bottlenecks or mishaps. Although not all motor accidents are related to road signs, their importance in the maintenance of road safety is not arguable. There are different types of road signs, which vary depending on their significance, shape, and size. All road signs have to legally adhere to regulations published by the department of transportation. These regulations proscribe the relative placement of the signs on the road, taking into account factors like size and occlusion of other signs. The objective of such rules is to ensure visibility of signs from a distance. It would make sense to have larger signs near the road, as they would be visible from the farthest point, but making them too large would be impractical and probably distracting as well. Normally, signs are less than 30 feet from the edge of the road and roughly a uniform height (~15 feet) from the ground to maintain consistent visibility.

The state department of transportation executes several maintenance activities to ensure road safety. Among these, traffic sign maintenance is probably one of the most critical. An incorrectly located sign or an absent or not visually accessible sign can lead to catastrophes on any road, especially on major highways. Although a lot of effort goes into designing and installing such signs, they are not immune to damage. There are several factors that contribute to the loss or diminishing utility of a road sign—like traffic accidents, weather, mechanical failure, etc. The aggregation of these factors over time can make the sign entirely useless.

In a traditional maintenance run for road signs, the operator uses a logbook and manually checks all of the signs following the logbook. There are two significant limitations to this approach. First, the operator must follow a pre-planned route; otherwise, the sequence of signs will not follow the logbook. And, there is a possibility that the path from the logbook may not be accessible at any given time. Second, the operator has to inspect the sign and verify its location manually. Manually matching qualitative descriptions such as an address to a particular geo-spatial location is difficult and prone to errors, and demands a high degree of familiarity with the geography of the region. A challenging aspect of maintenance of road signs is their sheer number. A six-mile stretch of an interstate highway (I-47) has just over 110 road signs; and with over 600,000 miles of road in the state of Texas, this leads to over a million road signs. With the problems mentioned above, this becomes a very labor-intensive, error-prone, and monotonic task for the maintenance operators. This current study, then, attempts to address these problems and make the maintenance of road signs more efficient and robust.

Methodology

A divide-and-conquer approach was used to address the two problems mentioned above. Individual solutions were implemented that later were integrated into a viable solution. A road-sign prediction system eliminates the first issue of following a logbook, which defines the maintenance route that the operator has to take in the maintenance run. This prediction system uses the real-time GPS coordinate of the vehicle to locate the road signs in an adjustable circular area centered on the real-time location of the vehicle. It also uses the last two coordinates to estimate the direction of the vehicle. Combining the location and the direction of the maintenance vehicle, the system predicts the incoming road

signs with a high degree of certainty. As the system knows which sign to look for at any given location, the maintenance operator does not have to follow a pre-defined route, as long as the entire area is covered. The problem of matching the road sign to a GPS coordinate is a simple step of recording the GPS coordinates of the vehicle simultaneously with the detection of the RFID tag attached to the road sign, and then matching the recorded coordinate of the vehicle to the pre-recorded coordinate sign. If the recorded coordinates match, the road sign is marked as verified, otherwise the display prompts the user about a missing sign.

Hardware

As the objective was to implement a practical and cost-effective solution to serve as a proof-of-concept for the idea, open source and easily accessible hardware with open source libraries were used to accelerate the prototyping. The entire setup is mounted in the vehicle and powered by the vehicle's battery. Figure 2 shows the high-level connections and communication protocols. The hardware configuration can be divided into six major components, as follows:

- Processing unit: Raspberry Pi 3 Model-B
- RFID reader: Impinj Speedway Reader
- Antenna: Linearly polarized Yagi antenna
- GPS: GPS module for relaying GPS information (frequency 10Hz)
- RFID Transponder or Tag: Tags' max pause time of 62.5 ms
- Interface: 7-inch capacitive touch with 800x480 full-color output and digital serial interface (DSI) port to connect to the Raspberry Pi 3

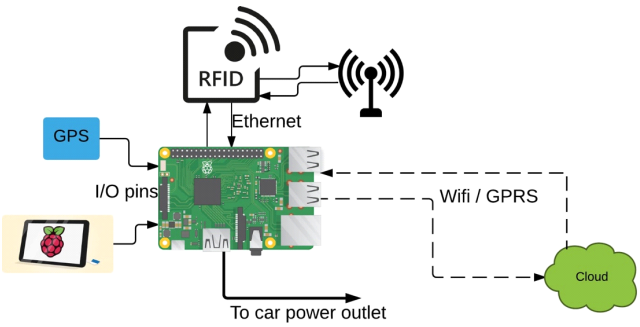

Figure 2. The Hardware Setup of the System on the Vehicle

Processing Unit

The Raspberry Pi 3 [7] board is a credit-card-sized computer with networking adapters. It houses a quad-core ARMv8 processor operating at 1.24 GHz with 1 GB of RAM, 40 general purpose I/O (GPIO) pins, Ethernet adapter, and onboard Wi-Fi module. One of the main reasons for choosing the Raspberry Pi 3 model B was the built-in networking features. Most commercial RFID readers, including the one used in this study, communicate using LLRP (low-level reader protocol) via Ethernet. With the Raspberry Pi's networking modules, which include an Ethernet adapter, it is convenient to interface the reader. Another advantage of using the Raspberry Pi is the easily configurable interface. The Raspberry Pi Foundation released a 7-inch display for the Raspberry Pi processors that uses a DSI port to interface and does not occupy the USB ports. Although this setup has a display unit, the software design is such that it is not mandatory. One of the design goals was that the system should be able to use any accessible display for its purposes; for example, a cell phone display or a tablet. This feature helps in adjusting the readability at the hardware level and also allows multiple operators to work with the system at the same time. The RFID reader had a USB output to power the Raspberry Pi 3 unit with 5 volts.

RFID Reader

There are several types of RFID readers available on the market. The most important design parameter in choosing an RFID reader is the operating frequency. The operating frequency of an RFID system affects the range of detection and the cost of the RFID transponders. As this system was intended to be used on a highway with RFID tags mechanically attached to every sign, the cost of individual transponders had to be as low as possible for commercial viability.

Apart from the technical constraints, using certain frequencies is not permitted by some governments, which also needs to be taken into consideration. These restrictions make ultra-high frequency (UHF) the only practical choice. The system uses the Impinj Speedway R420 reader [8], and operates in the UHF frequency range with a read rate of 1100 tags/second. It provides four antenna ports with a maximum sensitivity of -84 dBm and transmits power between +10 and +30 dBm, consuming 15W at +30 dBm. The reader also has an Ethernet port connected to the Raspberry Pi.

Antenna

The antenna in an RFID system is the most sensitive design factor. It determines the range of detection and the overall reliability of the scheme. Depending on their polarization, there are several types of antennas available, with the two most common being linear- and circular-polarized. The polarization of the antenna determines the radiation pattern and effective read range. Linear-polarized antennas

[9] radiating linear electric fields have long ranges and high levels of power that enable their signals to penetrate through different materials to read tags. Conversely, circular-polarized antennas radiate circular fields. One disadvantage of using linear-polarized antennas is that they are sensitive to tag orientation, unlike the circular-polarized antennas.

For the system in this study, the desired read range was between 5 and 30 feet; hence, a linear-polarized antenna and a five-element Yagi-Uda antenna was used. Yagi-Uda antennas are directional antennas and widely used as high-gain antennas in the UHF frequency band [10]. Figure 3(a) shows the radiation pattern for a five-element Yagi-Uda antenna—similar to the one used for the system in this study; Figure 3(b) shows the representation of beam width on a horizontal plane [11].

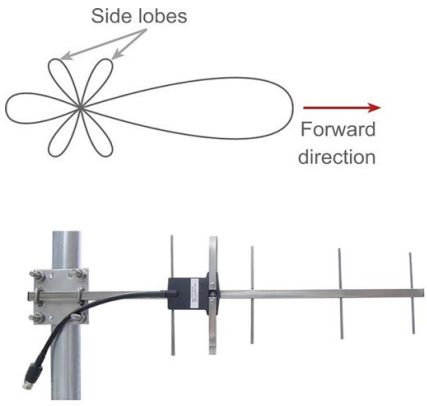

(a) Antenna Beam Width—Horizontal Plane

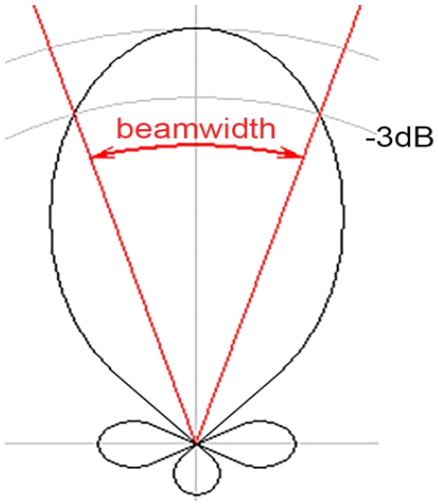

(b) Representation of Beam Width

Figure 3. Yagi-Uda Antenna

As seen in the diagram, this antenna has higher read range in a particular direction. The YA9-9 Yagi antenna [12, 13] used in the system has an operational frequency of 860-960 MHz and a beam width of 53 degrees. To increase the reliability of the system, two such antennas were mounted on the vehicle. Two antennas cover more area, which improves the chance of detection at high speeds. Both antennas are connected to the RFID reader and operate simultaneously.

GPS Module

The GPS module feeds real-time GPS information about the vehicle to the Raspberry Pi. The frequency of operation of the GPS module is set at 10Hz. At a highway speed of 70 mph (or 31.29 m/s), the maximum error in the GPS information is approximately ±3.5 meters. This error margin is used as an adjustment when the recorded GPS coordinate is matched to the preset GPS coordinate of the sign in the database.

RFID Transponder

The RFID transponders, or tags, are attached to the road signs and have unique serial numbers, or electronic product codes (EPC), electronically stored in them. Every tag is associated with a unique sign. The selection of the tags was made based on the following factors:

1. Memory size or EPC length
2. Operational frequency
3. Read range
4. Read time
5. Jacket
6. Cost

Over the years, the EPC length of commercially available RFID tags has grown from a single bit to 96 bits. An EPC length of 96 bits allows encoding of 2^{96} signs, which is more than sufficient for the current application. Highway road signs are typically 5-30 feet from the shoulder of the road. Lee et al. [2] shows the calculation of the read rate for a circular polarized antenna. A similar methodology is used to calculate the required read rate of the tags using the beam width of the linear polarized antenna. Assuming that the antenna is at the same height as the tag on the sign, and the highway speed is 70 mph, the minimum read area would be when the sign is closest to the road sign (i.e., 5 feet).

Speed of the vehicle: s = 70 mph or 103 fps
Distance from the road: d = 5 feet
Beamwidth = 53 degrees

$$\text{read distance} = \frac{2\pi * \text{beamwidth}}{360} \times \text{d} = 4.7 \text{ feet}$$

$$\text{read time} = \frac{\text{read distance}}{s} = 0.046 \text{ sec}$$

The tags chosen for this project housed an Alien Higgs 3 [14] integrated circuit. It is a single-chip UHF RFID tag that conforms to EPCglobal [15] Class 1 Gen 2 specifications. As mentioned previously, this tag works in the UHF range, 96 bits of EPC length, and a 10m read range and a read rate of 30 times a second (i.e., read time = 0.033 sec). This circuit meets all of the aforementioned criteria with a higher read range (10m > than 5–30 feet ~ 9.2m) and a lower read time (0.03 sec) than the calculated read time of 0.046 sec.

The primary purpose of the jacket in an RFID tag is the protection of the Higgs 3 integrated circuit. The solid waterproof form factor that can withstand temperature and humidity variations on the road is required. Commercially available tags come with several kinds of jackets that operate in far harsher conditions than the one in consideration. The tags used in this system were manufactured by Technologies ROI (www.troirfid.com). For an application that intends to tag all existing road signs, the cost of an individual tag is important to consider. Several factors contribute to the cost of a tag: frequency of operation the jacket; form factor; and the scale of production. The cost of a single tag is the aggregation of all these factors. Generating an approximate cost for tagging all signs in a given location has a lot of other variables to consider and is beyond the scope of this paper.

Software

From a software perspective, the bifurcation of the system into two subsystems for prediction and detection is based on their respective inputs. The input for the prediction system is the data from the GPS module. The GPS module gives positional data to the processing unit at a given frequency. Using time-series positional data, the processor evaluates the position and orientation of the vehicle and finally the incoming road sign(s). The input for the detection system is a combination of the signal from the RFID reader and GPS module. Using this information, the system makes an assessment of the correctness of the asset (road sign + tag) location and presence on the road.

The Prediction Subsystem

The main objective of the prediction system is to accurately predict the incoming road sign. In dynamic prediction, it is important for the system to be aware of the orientation of the vehicle on the road and the incoming sign, along with the distance between the vehicle and the road sign. The information from the GPS reader is read at a frequency of 10 Hz. The stream of data has the raw format for latitude and longitudinal information. The GPS reader thread keeps track of the two coordinate values—the present and the previous value. It reads this information and passes it to the controller, if there is a significant change in coordinates.

The controller thread generates the prediction in two steps. First, the information from the GPS reader thread and a user-defined GPS range is used to generate a query to the database that returns all of the signs in the area defined by the GPS range. The next phase is filtering the result from the previous query based on orientation. Then the controller calculates the angle between the line drawn by the present and old coordinates and the current coordinate and the coordinates of the sign. From all of the angles, the one with the shortest angle is sent to the view for display. To calculate the distance between two spherical coordinates, the latitude and longitude from the GPS module, the great circle distance expression of Equation (1) is used. The equation takes the latitude and longitude information from the GPS module as radial coordinates. First, the angle subtended by the two points (α_1, β_1) and (α_2, β_2) on the surface, known as the haversine angle [16] from the law of spherical trigonometry, is calculated and then the sine inverse of that angle multiplied with the approximate radius of earth gives the distance.

$$d = 2r \sin^{-1}\left(\sqrt{\sin^2\left(\frac{\Delta\alpha}{2}\right) + \cos(\alpha_1)\cos(\alpha_2)\sin^2\left(\frac{\Delta\beta}{2}\right)}\right) \quad (1)$$

where, α is latitude and $\Delta\alpha$ is the difference between latitudes; β is longitude and $\Delta\beta$ is the difference between longitudes; d is the distance between the points; and, r is the approximate radius of the earth (≈6371 km).

The result of this calculation is not exact, as the shape of the earth is not a sphere. But from experimental observation, it was found that it gives a reasonable approximation. For orientation of the car with respect to the incoming sign, the bearing of the car was calculated and from the bearing between the car and signs at a certain distance. The sign with the difference in bearing less than a threshold minimum and the smallest among other signs is selected as the predicted sign. To calculate the bearing of the maintenance vehicle, the two latest GPS locations from the maintenance vehicle are used in Equation (2). Equation (3) converts the output from Equation (2) to a range between 0 and 2π. Assuming that the maintenance vehicle is moving from point A (α_a, β_a) to point B (α_b, β_b), then the bearing is calculated as follows:

$$\theta = a\tan 2\begin{pmatrix} (\cos(\alpha_a)\sin(\alpha_b) \\ -\sin(\alpha_a)\cos(\alpha_b)\cos(\Delta\beta)) \\ ,sin(\Delta\beta)cos(\beta_b) \end{pmatrix} \quad (2)$$

where, α_x is latitude; β_x is longitude; and, $\Delta\beta$ is the difference between longitudes $\equiv \beta_b - \beta_a$.

$$\theta = 2\Pi + \theta \text{ for all } \theta < 0 \quad (3)$$

since, $\theta \subseteq (-\Pi, \Pi)$ and for the range to be $(0, 2\Pi)$.

The Detection Subsystem

The input from the RFID reader to the controller thread initiates the search of the detected EPC value for the predicted tags. If found, the present coordinate of the system is logged with the report generator class and the view is updated to show that the sign has been detected. At the end of the maintenance run, the operator saves the log and can print a report detailing the correct and missing road signs. Figure 4 shows the sequence diagram of the information flow of the detection subsystem.

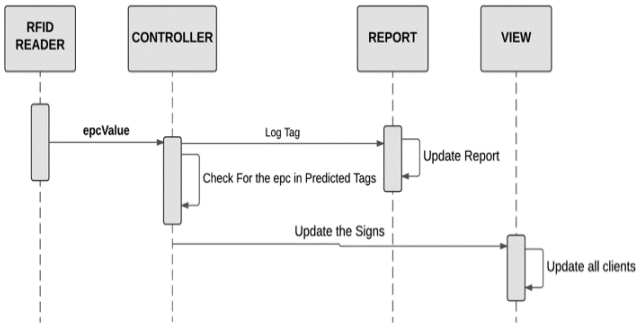

Figure 4. The Sequence Diagram for the Sign Detection System

Experimental Results

The test vehicle was set up similarly to the depiction in Figure 5, with a few changes for testing and diagnostic purposes. The primary objective of the experiment was to find the relationship between the speed of the vehicle and the placement of the tags for the number of tags read. The desired outcome would be for the system to read all tags at all speeds and at all tag placements. The system was tested on a series of roads that were set up in a similar fashion to a residential neighborhood, including intersections with multiple signs attached to a single pole. The purpose of these experiments was to establish a relationship between the placement of the tags, the speed of the vehicle, and the readability of the tags. Additionally, these experiments also verified the predictive functionality of the system.

All of the tests were done on-site at the Texas A&M Riverside campus, where 50 RFID tags were fixed to existing signs around the campus. There are 25 established locations and a total of 50 RFID tags; multiple tags were present at 15 of the locations. The database was prepared of those 50 tags with the corresponding road sign information (latitude, longitude, and sign type). Figure 6 shows all of the tag locations for the test at the campus. The tests consisted of driving through the tagged areas of the test site at varying speeds and distances from the signs, while monitoring the user interface of the device. The main observation from the experiment was the relationship between tag placement and readability. With respect to different placements of the tags on the signs, the location of the tag did significantly affect readability.

Having a vertical orientation offers the best read rate, but for the tag to be read effectively, the sign cannot stand between the Yagi antenna and the tag being read. This was

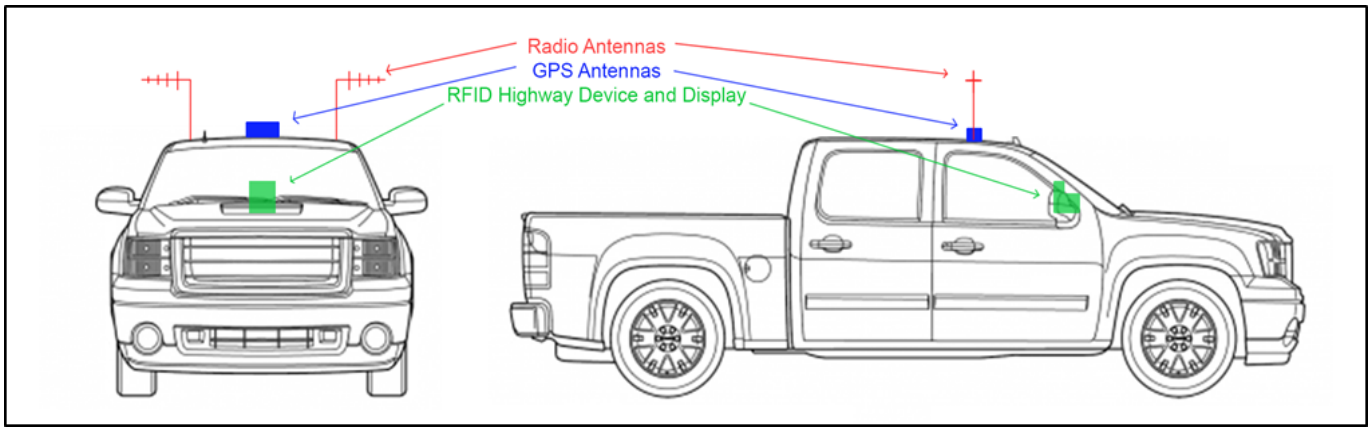

Figure 5. The Hardware Setup of the System on the Vehicle

done by placing the tag on the side of a sign that is closest to the intersection of the main road. In the left picture of Figure 7, one can see, from the truck's perspective, how the sign being tracked will block the RFID tag being read. The sign will cause interference for the Yagi antenna and the tag will not be read. However, if you change the placement of the tag so that it faces the intersection (see the image on the right side of Figure 7), the tag will always be read by the Yagi antenna, regardless of the direction of the vehicle.

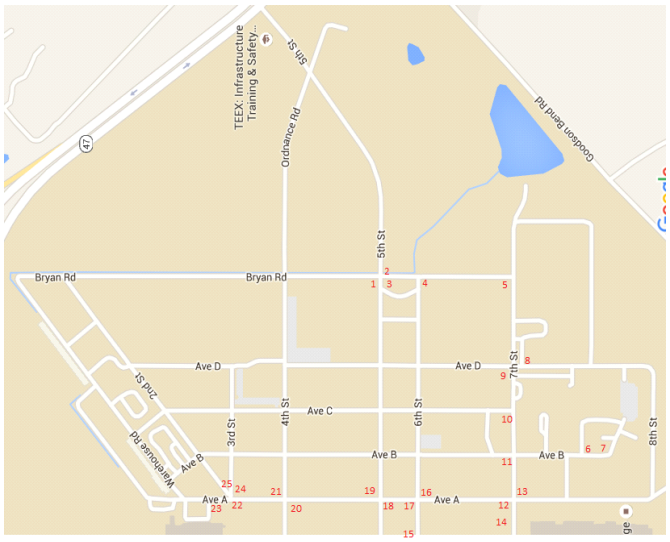

Figure 6. Map of the Tagged Signs at the Texas A&M Riverside Campus

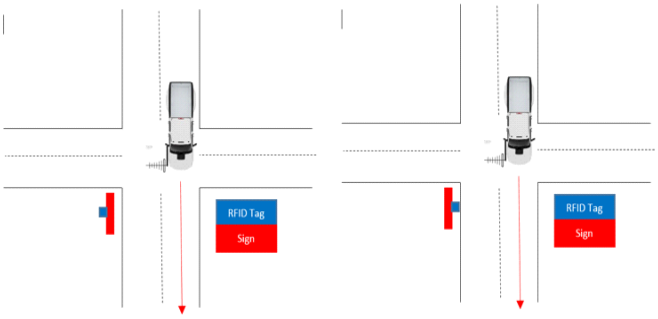

Figure 7. The Sign Blocks the Radio Waves (left-hand side of the figure), and Ideal Tag Placement (right-hand side of the figure)

The speed of the vehicle did not notably affect the read rate. Observations were consistent between 10 mph and 50 mph (maximum possible). If the tag was in sight of the Yagi antenna (i.e., a read range of up to 40 feet), it would be detected. As long as the tag was within the read range of the antenna, and was not obscured by the sign, the system was able to read the tags 100% of the time.

Conclusion

The results from the experiments done on the Texas A&M Riverside campus proved the utility of the system in a full-fledged deployment. Key challenges in a full-scale deployment would be the correct placement of the tags; but this would have to be done only once. The predictive system assists the operator to quickly verify, visually, the presence of a sign. The GPS system ensures the efficient, quick, and precise location verification without manual intervention. Cloud integration provides easy access to the reports and inventory system as well.

Acknowledgements

This work was supported by the Texas A&M Transportation Institute. Special thanks to Austin Munns, William Ellison, and Akash Sahoo for their support in the completion of this work.

References

[1] Landt, J. (2005). The history of RFID. *IEEE potentials*, *24*(4), 8-11.

[2] Lee, E. K., Yoo, Y. M., Park, C. G., Kim, M., & Gerla, M. (2009, September). Installation and evaluation of RFID readers on moving vehicles. *Proceedings of the sixth ACM international workshop on VehiculAr InterNETworking* (pp. 99-108). ACM.

[3] Ning, Y., Zhong-qin, W., Malekian, R., Ru-chuan, W., & Abdullah, A. H. (2013). Design of accurate vehicle location system using RFID. *Elektronika ir Elektrotechnika*, *19*(8), 105-110.

[4] World Health Organization The top 10 causes of death. (n.d.). Retrieved from http://www.who.int/mediacentre/factsheets/fs310/en/.

[5] Texas Department of Transportation. (2015). *Comparison of Motor Vehicle Traffic Deaths, Vehicle Miles, Death Rates, And Economic Loss 2003 - 2015*. Texas Peace Officer's Crash Reports (CR-3).

[6] Texas Department of Transportation. (2015). *Texas Motor Vehicle Traffic Crash Facts Calendar Year 2015*. Texas Peace Officer's Crash Reports (CR-3).

[7] Raspberry Pi 3 Model B. (n.d.). Retrieved from https://www.raspberrypi.org/products/raspberry-pi-3-model-b/

[8] Speedway Revolution Readers. (n.d.). Retrieved from http://www.impinj.com/products/readers/speedway-revolution/

[9] Yagi-Uda. (2008, April 12). *Yagi-Uda antenna*. Retrieved http://yagi-uda.com/yagi-uda_basics.php

[10] Fasching, D. F. (n.d.). Dr. Franz Fasching Information — Telecommunications — Technology Products — Services — Solutions. Retrieved from https://drfasching.com/products/gnss/raspignss.html
[11] Yagi-Uda antenna. (2017, April 13). Retrieved from https://en.wikipedia.org/wiki/Yagi%E2%80%93Uda_antenna
[12] Bevelacqua, P. (n.d.). Yagi-Uda Antenna. Retrieved from http://www.antenna-theory.com/antennas/travelling/yagi.php
[13] E. (n.d.). Yagi Antenna / Yagi-Uda Aerial. Retrieved from https://www.electronics-notes.com/articles/antennas-propagation/yagi-uda-antenna-aerial/basics-overview.php
[14] Alien. (n.d.). *HiggsTM 3 EPC Class 1 Gen 2 RFID Tag IC* [Brochure]. Author. Retrieved from http://www.alientechnology.com/wp-content/uploads/Alien-Technology-Higgs-3-ALC-360.pdf
[15] EPCglobal. (2016, December 30). Retrieved from https://en.wikipedia.org/wiki/EPCglobal
[16] Haversine formula. (2017, February 22). In *Wikipedia, the Free Encyclopedia*. Retrieved from https://en.wikipedia.org/w/index.php?title=Haversine_formula&oldid=766899354

Biographies

GHANSHYAM BHUTRA is a graduate student in the Computer Science Department of Texas A&M University. He earned his BS from the Institute of Technical Education and Research, Odisha, India. His interests include RFID systems and virtual and augmented reality applications. Mr. Bhutra may be reached at gbhutra@tamu.edu

BEN ZOGHI is the Victor H. Thompson chair professor of Electronics System Engineering Technology at Texas A&M. He currently directs the RFID/Sensor Lab and the new online professional Master of Engineering in Technical Management. A member of the Texas A&M University faculty for 30 years, he has distinguished himself as a teacher, writer, and researcher, and has been honored for his teaching excellence by the College and the Texas A&M University Association of Former Students. Ben's academic and professional degrees are from Texas A&M (PhD), The Ohio State University (MSEE), and Seattle University (BSEE). Dr. Zoghi may be reached at zoghi@tamu.edu

PAUL CARLSON has been with TTI since 1995 and is currently the Division Head of the Operations and Roadway Safety Division at Texas Transportation Institute. Paul got his PhD in civil engineering from Texas A&M University. Paul has over 20 years of experience associated with highway safety, traffic control devices, visibility, and identifying driver needs. While he has authored or co-author over 100 technical papers or research reports, his ultimate drive is to move research findings from reports to practice. Paul is nationally recognized for his work on visibility, retroreflectivity, and traffic control devices. Dr. Carlson may be reached at Paul-Carlson@tamu.edu

USING THE DESIGN OF EXPERIMENTS METHOD TO ELUCIDATE THE ROLE OF MATERIAL THERMAL DIFFUSIVITY IN THE WARPAGE OF INJECTION-MOLDED PLASTIC PARTS

Rex Kanu, Purdue Polytechnic Institute

Abstract

Injection molding is a versatile processing technique employed in the manufacture of plastic parts. The process consists of sequential steps, which, in their entirety, comprise process cycle time. These steps include mold closing, injection of molten plastic into a closed mold, cooling of the molten plastic, mold opening, and ejecting of molded parts. Injection molding cycle time is a very important manufacturing variable, because it can be used to estimate the time it would take to achieve a desired production quantity. Of these processing steps, the cooling event makes up 75% of the injection molding cycle time. For this reason, many studies have been undertaken to illuminate the cooling event with the goal of optimizing it and, consequently, the injection molding cycle time. To elucidate the influence of coolant flow regimes on the cooling event, the authors considered a thermal property of the plastics material—its thermal diffusivity—which consists of the material's specific heat capacity, thermal conductivity, and density. The authors chose this material's property because it measures how fast thermal energy travels through materials and, thus, affects the rate of thermal energy (heat transfer) removal during the cooling process.

Furthermore, it appears that the thermal diffusivity of a plastic material may play a crucial role in the cooling process, given that the ratio of the thermal diffusivities of the material generally involved in the cooling process is 1:1.6:50 (plastics: water: steel). This implies that the thermal diffusivity of plastic may be the controlling or limiting variable in the cooling process. Therefore, by using the design of experiments (DOE) method, the author examined the roles that processing and material variables play in the cooling process and in plastic part warpage. These variables include plastic thermal diffusivity, coolant flow rates, cooling time, coolant temperature, and injection back pressure.

Introduction

Injection molding is a useful processing technique employed in the manufacture of plastic parts. The process consists of sequential steps, which, in their entirety, comprise process cycle time. These steps include mold closing, injection of molten plastic into a closed mold, cooling of the molten plastic, mold opening, and ejecting of molded parts. Of these steps, the cooling process seems to play a critical role in a successful injection molding process, because it alone generally accounts for about 75 percent of the cycle time [1]. Furthermore, the cooling process has a large influence on plastic part quality [2]. In a previous study [3], one of the authors examined the influence of coolant flow regimes on the cooling event. Rosato et al. [4] expressed the overall heat-transfer coefficient, U, of the cooling process by Equation (1):

$$\frac{1}{U} = \frac{1}{KS} + \frac{1}{\pi D h_i} \tag{1}$$

where, U is the overall heat-transfer coefficient, W/m^2-°C or Btu/ft^2-hr-°F; K is the thermal conductivity of mold material (metal), W/m-°C or Btu/ft-hr-°F; S is the conduction shape factor of the cooling channels; D is the diameter of the cooling channel, m or ft; and, h_i is the inner (inside of cooling channel) convective heat-transfer coefficient, W/m2-°C or Btu/ft2-hr-°F.

As Equation (1) suggests, the cooling process is primarily influenced by the mold material through its thermal conductivity, K, the cooling channel shape factor, S, and the inner convective heat-transfer coefficient, h_i. Equation (2) relates h_i to the coolant properties and coolant flow rate [5] and is valid for a Reynolds number, N_{RE}, greater than or equal to 6000. It is important to note that in another study [3], the authors examined the influence of coolant flow regimes on warpage of injection-molded plastic parts; however, the study did not consider the thermal properties of plastic materials.

In this current study, then, it seemed appropriate to consider the thermal diffusivity of plastics among the variables to be studied. This is because the thermal properties of the plastic materials being injection molded are missing from Equations (1) and (2), which are the primary equations that describe the cooling process of the injection-molding process:

$$\frac{h_i}{c_p G}\left(\frac{c_p \mu}{k}\right)^{\frac{2}{3}}\left(\frac{\mu_w}{\mu}\right)^{0.14} = \frac{0.023}{\left(DG/\mu\right)^{0.2}} \quad (2)$$

where, c_p is the specific heat capacity of the coolant at constant pressure, J/g-°C or Btu/lb-°F; D is the diameter, m or ft; G is the mass velocity, kg/m^2-s or lb/ft^2 –s ($G = V\rho$); h_i is the inner (inside of cooling channel) convective heat-transfer coefficient, W/m^2-°C or Btu/ft^2-hr-°F; k is the thermal conductivity of coolant, W/m-°C or Btu/ft-hr-°F; V is the average velocity, m/s or ft/s; ρ is the density of coolant, kg/m^3 or lb/ft^3; μ is the viscosity of coolant, kg/m-s or lb/ft-s; and, μ_w is the viscosity of coolant at wall temperature.

As Figure 1 shows, the cooling process consists of a series of heat transfer processes from the plastic to the mold and to the coolant. Several studies have examined different aspects of this process and how it could impact plastics parts warpage. For example, Zhil'tsova et al. [6], Song et al [7], and Park and Ahn [8] studied the effects of processing parameters on the quality of injection-molded parts. Other researchers [9, 10] investigated the impact of mold properties on the quality of injection-molded parts, while others [11-14] focused their efforts on elucidating the factors that cause warpage in injection-molded parts. Huszar et al. [15] studied the influence of flow and thermal properties on injection pressure and cooling time prediction. In this work, the authors examined the influence of processing variables and material property—namely, coolant flow rates, coolant temperature, cooling time, back pressure, and thermal diffusivity—on warpage of injection-molded plastic parts using DOE.

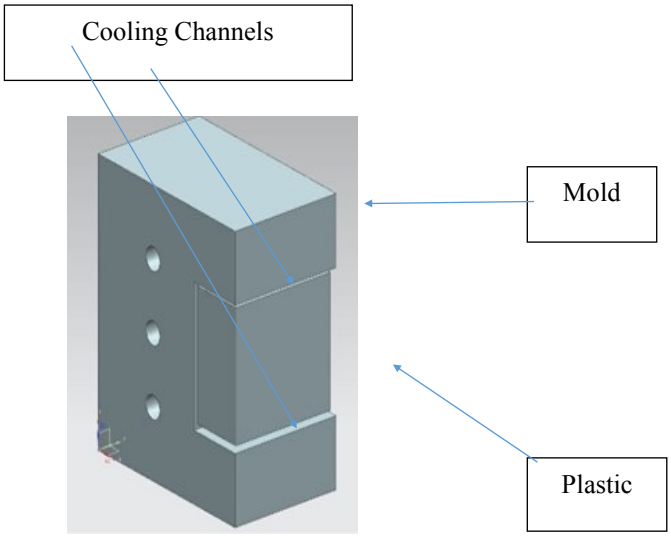

Figure 1. Plastics in Mold with Cooling Channels

Definitions

Thermal diffusivity, α, is defined as the rate at which thermal energy diffuses through a substance. It is expressed using Equation (3):

$$\alpha = \frac{k}{c_p \rho} \quad (3)$$

where, α is the thermal diffusivity, mm^2/s or ft^2/hr; k is the thermal conductivity of plastics, W/m-°C or Btu/ft-hr-°F; c_p is the specific heat capacity of plastics at constant pressure, J/g-°C or Btu/lb-°F; and, ρ is the density of the plastic, kg/m^3 or lb/ft^3.

The author acknowledges that thermal transfer properties of plastics are a function of temperature [1], and Zhang and Fujii [16] had shown that the thermal diffusivity for a polypropylene homopolymer decreased by 52% (5.58x10^{-3} ft^2/hr to 2.65x10^{-3} ft^2/hr), as the temperature increased from 104ºF to 482ºF. The effect of this change in thermal diffusivities of the materials as a function of the process temperature is captured in the experimental work of this current study, due to the comparative aspect of the DOE method. Warpage is defined as "a distortion where the surfaces of the molded part do not follow the intended shape of the design. Part warpage results from molded-in residual stresses, which, in turn, is caused by differential shrinkage of material in the molded part" [18].

Experimental Materials

Two grades of polypropylene (PP) materials, supplied by the RTP company, were used in this study. These materials were selected, because the ratio of their thermal diffusivities was 1:3.8, while their physical and processing parameters were similar, as shown in Table 1. Except for drying the materials, they were used as received.

Equipment

A Sandretto 60-ton injection molding machine was used to mold tensile test specimens, according to ASTM D-638. A Conair Mold Temperature Controller (MTC), model TCI-DI, was used to control coolant temperature and supply the mold with coolant. The inlet and outlet temperatures of the coolant (water) were measured with two CEN-TECH P3777 digital thermocouples, which were inserted into the hoses carrying the coolant. These temperatures were used to determine the mold temperature and to determine steady state conditions, which were achieved when the temperature readings were constant. Two Omega flow meters, model FL-2300ABR, and ball valves, shown in Figure 2, were used to

control the coolant flow rate to the mold. A Thermolyne digital pyrometer was used to measure the plastics' melt temperature. A Conair dehumidifying dryer, model CD-30, was used for drying the materials.

Table 1. Polypropylene-Based Material Properties and Processing Parameters

Property	RTP Compounds 199 X 104849 A (PP)	RTP Compounds 199 X 91020 A Z (PP)
Feature	Thermally Conductive	Thermally Conductive
Density	1.50 g/cm^3	2.00 g/cm^3
Thermal Conductivity	12 Btu-in/hr-ft^2-°F	4.2 Btu-in/hr-ft^2-°F
Specific Heat Capacity	0.445 Btu/lb-°F	0.445 Btu/lb-°F
Calculated Thermal Diffusivity, α	0.023 ft^2/hr	0.006 ft^2/hr
Drying Temperature	175 °F	175 °F
Drying Time	2.0 hr	2.0 hr
Processing (melt) Temperature	375 – 450 °F	375 – 450 °F
Mold Temperature	90 – 150 °F	90 – 150 °F
Injection Pressure	10000 – 15000 psi	10000 – 15000 psi
Back Pressure	50 – 100 psi	50 – 100 psi
Fill Speed	2 – 3 in/s	2 – 3 in/s
Screw Speed	60 – 90 rpm	60 – 90 rpm

Figure 2. Omega Flow Meters

Procedure

Two sets of experiments were conducted in this study. The first, shown in Table 2, was a 2^4 factorial design with two replicates, resulting in 32 experimental runs. For each run, about ten specimens were produced after state steady conditions were attained. The specimens were allowed to equilibrate to room temperature (~72–74°F) for 48 hours; part warpage was then measured using a bench steel block from the Smith Tool and Engineering Company and a spring gage on five randomly selected test specimens produced for each run, as shown in Figure 3. The run order was randomly generated using Minitab. Minitab is a statistical application software. The variables considered in this set of experiments were coolant flow rate, mold temperature, cooling time, and PP thermal diffusivity.

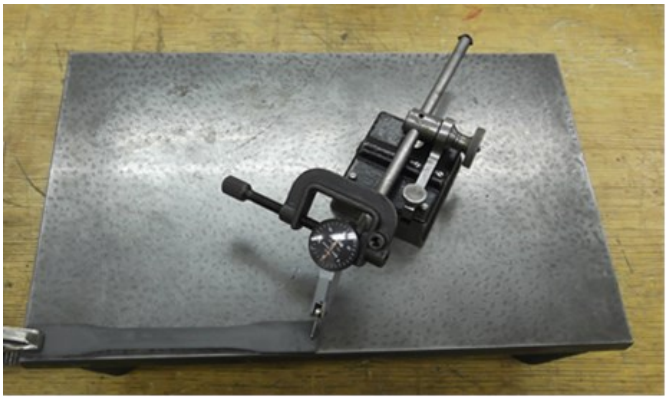

Figure 3. Tensile Test Specimen Being Examined for Warpage on a Steel Block

In Table 2, the mold temperature is in °F; cooling time is in seconds; coolant flow rate is in gallons per minute (gpm); and thermal diffusivity, alpha (α), high = 0.023 ft^2/hr and low = 0.006 ft^2/hr. The second set of experiments, shown in Table 3, was a 2^2 factorial design with two replicates, resulting in eight experimental runs. The experimental procedure was similar to the first set of experiments, but the variables for these experiments were PP thermal diffusivity and injection molding back pressure. In Table 3, injection back pressure is in lb/in^2 (psi). Table 4 contains processing variables that were kept constant during the second set of experiments.

Results

Figure 4 shows that, for the first set of experiments, the variable that was found statistically significant to influence part warpage was PP thermal diffusivity. The same results are represented numerically in Table 5. Figure 5 shows the relative effects of the variables on part warpage. For mold

Table 2. 2^4 Factorial Design with 2 Replicates

Standard order	Run order	Center point	Blocks	Mold temp (°F)	Coolant flow rate (gpm)	Thermal diffusivity (α)	Cooling time (sec)
32	1	1	1	160	1.4	High	40
30	2	1	1	160	0.5	High	40
28	3	1	1	160	1.4	Low	40
11	4	1	1	80	1.4	Low	40
2	5	1	1	160	0.5	Low	10
27	6	1	1	80	1.4	Low	40
4	7	1	1	160	1.4	Low	10
25	8	1	1	80	0.5	Low	40
24	9	1	1	160	1.4	High	10
20	10	1	1	160	1.4	Low	10
14	11	1	1	160	0.5	High	40
15	12	1	1	80	1.4	High	40
26	13	1	1	160	0.5	Low	40
6	14	1	1	160	0.5	High	10
12	15	1	1	160	1.4	Low	40
21	16	1	1	80	0.5	High	10
16	17	1	1	160	1.4	High	40
18	18	1	1	160	0.5	Low	10
31	19	1	1	80	1.4	High	40
10	20	1	1	160	0.5	Low	40
8	21	1	1	160	1.4	High	10
1	22	1	1	80	0.5	Low	10
5	23	1	1	80	0.5	High	10
23	24	1	1	80	1.4	High	10
29	25	1	1	80	0.5	High	40
13	26	1	1	80	0.5	High	40
22	27	1	1	160	0.5	High	10
19	28	1	1	80	1.4	Low	10
9	29	1	1	80	0.5	Low	40
17	30	1	1	80	0.5	Low	10
3	31	1	1	80	1.4	White	10
7	32	1	1	80	1.4	Black	10

Table 3. 2^2 Factorial Design with 2 Replicates

Standard Order	Run Order	Center Point	Blocks	Thermal Diffusivity (α)	Back Pressure (psi)
2	1	1	1	High	75
8	2	1	1	High	150
5	3	1	1	Low	75
3	4	1	1	Low	150
1	5	1	1	Low	75
7	6	1	1	Low	150
4	7	1	1	High	150
6	8	1	1	High	75

Table 4. Injection Molding Processing Parameters

Processing Parameter	Values used during the experiment
Injection Speed	1.4 in/s
Screw Speed	75 rpm
Materials' Drying Temperature	175 °F
Drying Time	2 hours
Nozzle temperature	450 °F
Front barrel temperature	450 °F
Middle barrel temperature	430 °F
Rear barrel temperature	400 °F
Estimated melt temperature	423 – 445 °F
Mold temperature for 2nd experiments	120 °F
Injection pressure	1500 psi
Packing pressure	400 psi
Holding pressure	200 psi
Coolant flow rate for 2nd experiment	1.4 gpm

temperature, Figure 5 shows that it (mold temperature) had some influence on part warpage, even though it was statistically insignificant. However, it shows that part warpage increased slightly with increases in mold temperatures. For coolant flow rate and cooling time, it shows that both variables slightly reduced part warpage as these variables were increased. For thermal diffusivity (alpha, α), its impact on part warpage was significantly higher than other variables. Statistically, its *p*-value of 0.014 was less than 0.05. Of all the variables considered in this study, it was the only variable whose *p*-value was less than 0.05 in the first set of experiments shown in Table 2.

In the second set of experiments, the variables considered were PP thermal diffusivity and back pressure, since cooling time, coolant flow rate, and mold temperature were found to be statistically insignificant in influencing part warpage. For this set of experiments, Figure 6 shows that PP thermal diffusivity and back pressure were statistically significant in affecting part warpage, while the interaction effects of both variables on part warpage were not significant. The same results are presented in Table 6. The results in Figure 6 and Table 5 suggest that, although both variables had significant impacts on part warpage, the effect of thermal diffusivity (*p*-value = 0.005) was slightly higher than that of injection back pressure (*p*-value = 0.009), indicating the importance of the plastic materials' thermal diffusivity in controlling warpage in injection-molded plastics parts.

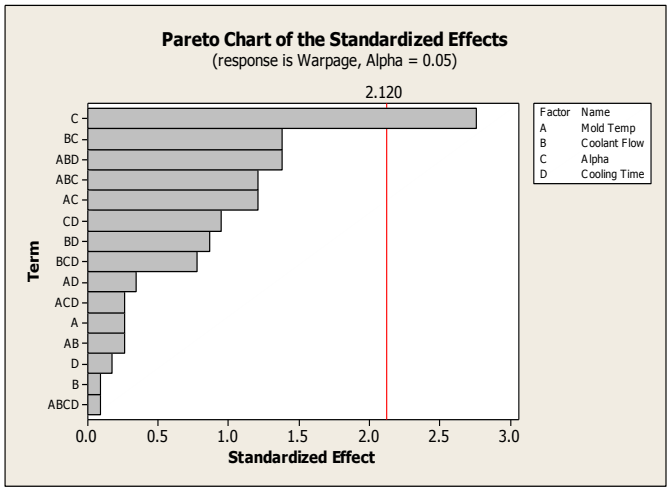

Figure 4. Alpha (α) is Statistically Significant in Affecting Part Warpage

Figure 7 shows the relative effects of PP thermal diffusivity and injection molding back pressure on part warpage. It shows that high values of PP thermal diffusivity (alpha, α) had the least effect on part warpage, while low back pressures had the least effect on part warpage. For these variables, these results suggest a preference for selecting a material with comparatively higher thermal diffusivity and processing the material at the lowest possible back pressure to minimize the occurrences of part warpage.

Table 5. Factorial Fit: Warpage versus Mold Temp, Coolant Flow, Cooling Time, Thermal Diffusivity

Estimated Effects and Coefficients for Warpage					
Variable	Effect	Coefficient	SE Coefficient	*T*	*P*-value (significant if < 0.05)
Constant		0.007938	0.000725	10.95	0.000
Mold Temperature	0.000375	0.000188	0.000725	0.26	0.799
Coolant Flow	-0.000125	-0.000063	0.000725	-0.09	0.932
Thermal Diffusivity (α)	-0.004000	-0.002000	0.000725	-2.76	0.014 (significant)
Cooling Time	-0.000250	-0.000125	0.000725	-0.17	0.865
Mold Temp*Coolant Flow	0.000375	0.000187	0.000725	0.26	0.799
Mold Temp*Thermal Diffusivity (α)	0.001750	0.000875	0.000725	1.21	0.245
Mold Temp*Cooling Time	0.000500	0.000250	0.000725	0.34	0.735
Coolant Flow*Thermal Diffusivity (α)	-0.002000	-0.001000	0.000725	-1.38	0.187
Coolant Flow*Cooling Time	-0.001250	-0.000625	0.000725	-0.86	0.401
Thermal Diffusivity, α*Cooling Time	0.001375	0.000688	0.000725	0.95	0.357
Mold Temp*Coolant*Thermal Diffusivity (α)	-0.001750	-0.000875	0.000725	-1.21	0.245
Mold Temp*Coolant Flow*Cooling Time	-0.002000	-0.001000	0.000725	-1.38	0.187
Mold Temp*Thermal Diffusivity, α*Cooling Time	0.000375	0.000188	0.000725	0.26	0.799
Coolant Flow*Thermal Diffusivity, α*Cooling Time	-0.001125	-0.000563	0.000725	-0.78	0.499
Mold Temp*Coolant Flow*Thermal Diffusivity, α*Cooling Time	-0.000125	-0.000062	0.000725	-0.09	0.932

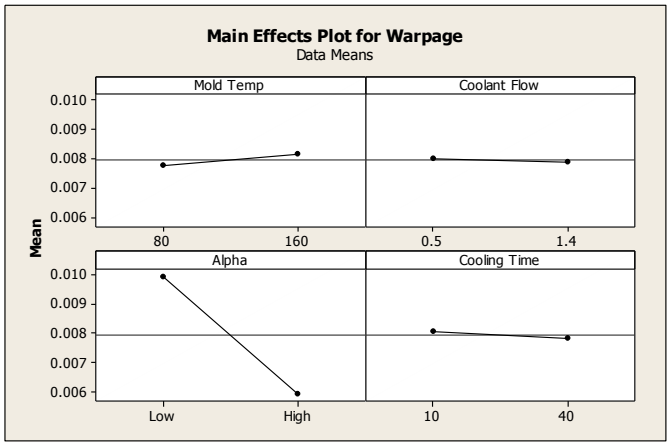

Figure 5. The Relative Effects of the Variables on Part Warpage

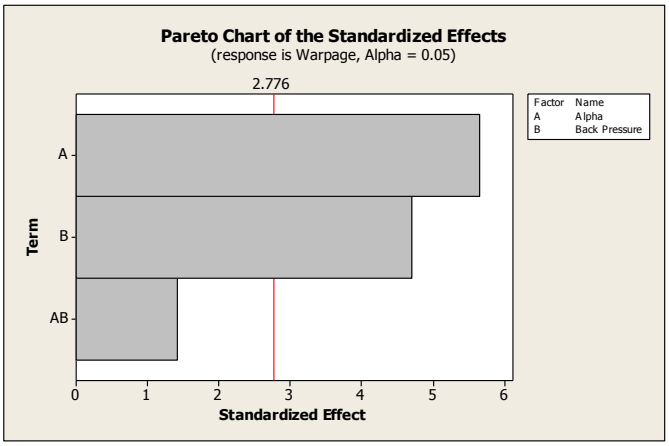

Figure 6. Alpha and Back Pressure are Statistically Significant in Affecting Part Warpage

Table 6. Factorial Fit: Warpage versus Alpha, Back Pressure

Estimated Effects and Coefficients for Warpage					
Variable	Effect	Coefficient	Standard Error (SE) Coefficient	*T*	*P*-Value (significant if < 0.05)
Constant		0.008750	0,000530	16.50	0.000
Thermal Diffusivity (α)	-0.006000	-0.003000	0.000530	-5.66	0.005 Significant
Back Pressure	0.005000	0.002500	0.000530	4.71	0.009 Significant
Thermal Diffusivity, α*Back Pressure	-0.001500	-0.000750	0.000530	-1.41	0.230

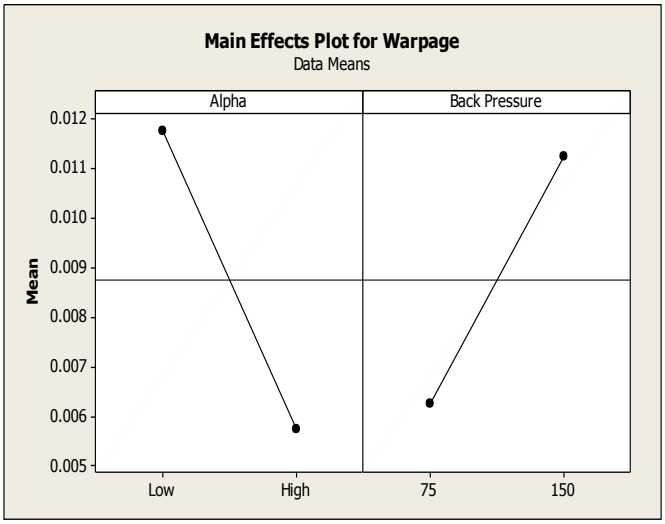

Figure 7. The Relative Effects of PP Thermal Diffusivity and Back Pressure on Part Warpage

Conclusions

The findings of this study suggest that only the materials' (PP) thermal diffusivity and injection molding back pressure had a statistically significant influence on part warpage. These findings are important for custom injection molders, who process a variety of plastic materials for their clients. Unlike dedicated injection processors that process one or only a few plastic materials, custom injection molders are at the mercy of their clients, as far as the spectrum of plastic materials they can process. For these injection processors, the frequent changing of plastic materials presents unique problems, because different plastics have varying properties that affect machine settings. Achieving optimal machine settings requires considerable operator experience and time, and time is money.

This study suggests that an understanding of the role plastic thermal diffusivity plays in part quality may help reduce setup time and facilitate problem troubleshooting associated with part warpage. These findings are limited to the plastic material, polypropylene, used in this study, since the extent to which a materials' thermal diffusivity affects injection molded part warpage will depend on the magnitude of a material's thermal diffusivity.

Acknowledgments

References

[1] Kimerling, T. (2002). Injection molding cooling time reduction and thermal stress analysis. Retrieved from http://www.ecs.umass.edu/mie/labs/mda/fea/fealib/Tom%20Kimerling/TKimerling_injection_molding.pdf

[2] Taghizadeh, S., Ozdemir, A., & Uluer, O. (2013). Warpage prediction in plastic injection molded part using artificial neural network. *IJST, Transaction of Mechanical Engineering, 37*(M2), 149-160.

[3] Kanu, R. C., & Marsh, N. (2013). The influence of liquid coolant flows regimes on the quality of injection molded plastic parts. *International Journal of Modern Engineering, 14*(1), 58-64.

[4] Rosato, D. V., Rosato, D. V., & Rosato, M. G. (2000). *Injection Molding Handbook*. The Netherlands: Kluwer Academic.

[5] Smith, W. L., Smith, J. C., & Harriott, P. (1993). *Unit Operations of Chemical Engineering*. New York: McGraw-Hill.

[6] Zhil'tsova, T. V., Oliveira, M. S., & Ferreira, J. A. (2009). Relative influence of injection molding processing conditions on HDPE Acetabular cups dimensional stability. *Journal of Materials Processing Technology, 209*, 3894-3904.

[7] Song, M. S., Liu, Z., Wang, M. J., Yu, T. M., & Zhao, D. Y. (2007). Research on effects of injection process parameters on the molding process for ultra-thin wall plastic parts. *Journal of Materials Processing Technology, 187-188*, 668-671.

[8] Park, K., & Ahn, J. H. (2004). Design of experiment considering two interactions and its application to the injection molding processes with numerical analysis. *Journal of Materials Processing Technology, 146*, 221-227.

[9] Postawa, P., Kwiatkowski, D., & Bociaga, E. (2008). Influence of the method of heating/cooling moulds on the properties of injection molding parts. *Archives of Materials Science and Engineering, 31*(2), 121-124.

[10] Kovacs, J. G., & Bercsey, T. (2005). Influence of mold properties on the quality of injection molded parts. *Periodica Polytechnica Mechanical Engineering, 49*(2), 115-122.

[11] Shuaib, N. A., Ghazali, M. F., Shayfull, Z., Zain, M. Z., & Nasir, S. M. (2011). Warpage factors effectiveness of a thin shallow injection-molded part using Taguchi method. *International Journal of Engineering & Technology, 11*(1), 182-187.

[12] Tang, S. H., Tan, Y. J., Sapuan, S. M., Sulaiman, S., Ismail, N., & Samin, R. (2007). The use of Taguchi method in the design of plastic injection mould for

reducing warpage. *Journal of Materials Processing Technology, 182*, 418-426.
[13] Kramschuster, A., Cavitt, R., Ermer, D., Chen, Z., & Turng, L. S. (2005). Quantitative study of shrinkage and warpage behavior for microcellular and conventional injection molding. *Polymer Engineering and Science,* 1408-1418.
[14] Sanchez, R., Aisa, J., Martinez, A., & Mercado, D. (2012). On the relationship between cooling setup and warpage in injection molding. *Measurement, 45*, 1051-1056.
[15] Huszar, M., Belblidia, F., Alston, S., Wlodarski, P., Arnold, C., Bould, D., et al. (2016). The influence of flow and thermal properties on injection pressure and cooling time prediction. *Applied Mathematical Modelling, 40*, 7001-7011.
[16] Zhang, X., & Fujii, M. (2003). Measurements of the thermal conductivity and thermal diffusivity of polymers. *Polymer Engineering and Science, 43*(11), 1755-1764.
[17] Shrinkage and Warpage. (n.d.). Retrieved from http://www.dc.engr.scu.edu/cmdoc/dg_doc/develop/process/physics/b35000001.htm
[18] Restrepo, J., Lopez, I. D., & Naranjo, A. (2013). Simulation of cooling using a new model for the determination of the thermal diffusivity in injection molding by means of the radial function method. *SPE ANTEC,* 1608-1612.

Biographies

REX C. KANU is an assistant professor of mechanical engineering technology at Purdue Polytechnic Institute. He earned his BS in chemical engineering from Northeastern University, MS in chemical engineering from the University of Connecticut, SM in management science from the Massachusetts Institute of Technology, and his PhD in polymer science from University of Connecticut. Dr. Kanu is currently teaching at Purdue Polytechnic Institute. His research interests include polymer nanocomposites, polymer blends, and plastics processing. Dr. Kanu may be reached at rkanu@purdue.edu

PSEUDO LINKAGES FOR KINEMATIC MODELING OF INDUSTRIAL ROBOTS

Alamgir Choudhury, Western Michigan University; Jorge Rodriguez, Western Michigan University;
Mitch Keil, Western Michigan University

Abstract

Robots in manufacturing applications often go through kinematic transformations, due to the adaption of manufacturing tools. Motion planning and control of such a system requires the ability for fast reconfiguration of the kinematic model in an automated manufacturing environment. The computational complexity and lack of flexibility of methods for modeling a changing geometric configuration present a challenge for the online usage of these models. A modified Eulerian angle-based scheme for kinematic modeling of a robotic system is presented here. To reduce computational burden, instead of using the traditional single-degree-of-freedom kinematic links, this method represents a physical system utilizing multi-degree-of-freedom kinematic linkages. The scheme was applied to generate a kinematic model and simulate the motion of a PUMA 560 laboratory robot and a Fanuc S110 industrial robot, resulting in a significant reduction of computation. The model was applied in motion planning of a four-link redundant system by solving the inverse kinematic problem. The generalized nature and reduced computation makes this scheme suitable for tasks requiring frequent reconfiguration of the mathematical models.

Introduction

Beyond traditional pick-and-place operations, modern industrial robots are used to perform a variety of tasks in manufacturing industries. For performing these tasks, the integration of tools to the robot end effector changes the kinematics and dynamics of the system significantly. Simulating robot motion along with additional tools is essential in order to ensure flawless execution of a planned task. The high level cognitive function for reasoning, action, and perceived changes in an unknown environment requires both qualitative and quantitative models [1, 2] of a geometry-based system. Lin and Lewis [3] used a qualitative approach for representation of planar robot kinematics. Lin and Lewis [4] also generated kinematic equations qualitative geometry primitives. The development of a general approach for a qualitative representation of the system is still an open problem. While qualitative models are necessary in high-level decision-making processes involving external data, quantitative models are suitable for localized functions (e.g., path planning, motion analysis, design, and control of the robotic system). Combined models utilizing both qualitative and quantitative behavior of a system may serve as a basis for general application of a complex system. Steinbaur and Wotawa [5] proposed the use of a combined framework of both quantitative and qualitative models for the fault detection of a mobile robotic system.

For a quantitative model, various methods of kinematic and dynamics modeling of open-chain mechanical systems have been proposed. Among them, most notably, Denavit and Hartenberg [6] utilized one-degree-of-freedom (translation or rotation) links for modeling a serial chain as interconnected rigid bodies with lower pair joints. Paul [7] and Whitney and Lozinski [8] adapted this notation for modeling and simulation of early robotic system. The basis of this method was a 4x4 homogeneous transformation matrix for each link. In an automated manufacturing environment, switching the end-effector tools requires one to incorporate time-consuming steps in the model. Wang et al. [9] used topological diagrams for representing serial and parallel manipulators. Their goal was efficient synthesis of kinematic structures, based on specific joint constraints. Valsamos et al. [10] proposed pseudo joints in metamorphic links of different classes of mechanisms. Though this treatment addresses the specific kinematic requirement of a serial manipulator, the general motion problem remains to be addressed.

In this paper, the authors propose the use of pseudo linkages for a quantitative kinematic scheme of serial manipulators with lower pair joints. A Eulerian angle-based formulation is utilized in which the system parameters can be manipulated to generate the mathematical model. Use of a Modified Eulerian Angle [11, 12] allows for degrees of freedom of each kinematic link up to the maximum possible six parameters. The kinematics of each link is defined by three translational and three rotational parameters. The resulting model is suitable for solving both forward and inverse kinematic problems (i.e., to predict the overall motion of a system and the end-effector based on the input motion of the actuators and vice versa). Generally, there is no unique solution to the inverse kinematic problem of a redundant robotic system. Therefore a solution method requires that appropriate constraints be imposed on the system prior to optimizing an objective function.

Kinematic Model

The kinematic model of an *n*-degree-of-freedom robot with only rotational motion, based on the modified Eulerian angle is presented below. It is assumed that the robot links are perfectly rigid and there is no mechanical compliance at the joints. The system consists of *m* links with 6*m* independent parameters, out of which *n* parameters are time-dependent generalized coordinates. The rest are physical constants defining the kinematic structure of the system. Figure 1 shows a representation of such a generalized system.

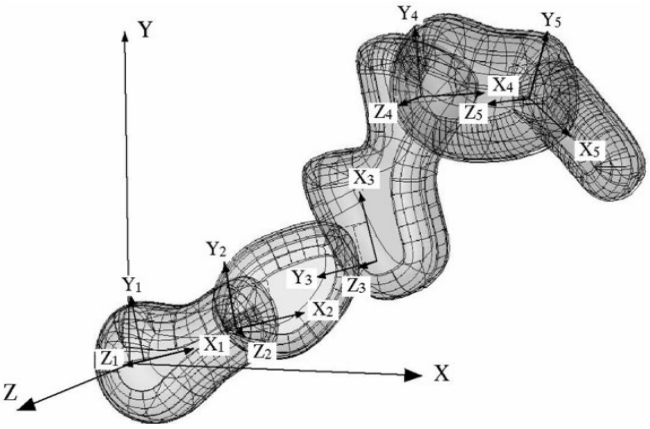

Figure 1. Generalized Representation of an Open-Chain Mechanism

In general, the *i*th link between the *i*th and (*i*+1)th joints is represented by the Cartesian joint coordinates L_{xi}, L_{yi}, and L_{zi}. The modified Eulerian angles θ_i, φ_i, and ψ_i (nutation, precession, and spin angles) of the *i*th reference frame with respect to the (*i*-1)th reference frame represent the orientation of the link. Mathematically, a vector, $\bar{e}_i$, corresponding to the *i*th reference frame is related to that of the (*i*-1)th reference frame by Equation (1):

$$\bar{e}_i = T_i \, \bar{e}_{i-1} \tag{1}$$

where, T_i is a 3x3 orthogonal matrix representing the transformation from the (*i*-1)th reference frame to the *i*th reference.

T_i, then, is given by Equation (2):

$$T_i = \begin{bmatrix} C_1C_{2-3} + S_2S_{2-3} & C_1S_2C_{2-3} - C_2S_{2-3} & -S_1C_{2-3} \\ C_1C_2S_{2-3} - S_2C_{2-3} & C_1S_2S_{2-3} + C_2C_{2-3} & -S_1S_{2-3} \\ S_1C_2 & S_1S_2 & -C_1 \end{bmatrix} \tag{2}$$

where, $C_1 = \cos(\theta_i)$, $S_2 = \sin(j\ \iota)$, $C_{2\text{-}3} = \cos(q_\iota - \varphi_i)$, etc.

Based on these transformation matrices, the position of the *i*th joint with respect to the fixed reference frame (XYZ) at the base of the robot is given by Equations (3) and (4):

$$[X_i\ Y_i\ Z_i]^T = \sum_{j=1}^{i} A_j [L_{xj}\ L_{yj}\ L_{zj}]^T \tag{3}$$

$$A_j = \prod_{j=1,i} T_j^T \tag{4}$$

Using elements of the transformation matrices in Equation (3), the orientation of the *i*th link with respect to the fixed inertial reference frame at the base of the robot is derived using Equations (5)-(8):

$$\theta_i = tan^{-1}\left[\frac{(A_i(1,3)^2 + A_i(2,3)^2)^{\frac{1}{2}}}{A_i(3,3)} \right] \tag{5}$$

$$\varphi_i = tan^{-1}\left[\frac{(A_i(3,2)}{A_i(3,1)} \right] - Atan\left[\frac{A_i(2,3)}{A_i(1,3)} \right] \tag{6}$$

$$\psi_i = tan^{-1}\left[\frac{(A_i(3,2)}{A_i(3,1)} \right] \tag{7}$$

If $\theta_i = 0$ or π, then the foregoing reduces to Equation (8):

$$\psi_i = tan^{-1}\left[\frac{(A_i(1,2)}{A_i(1,1)} \right] \tag{8}$$

Using i=m in the foregoing equations, the position and orientation of a robot end-effector or tool tip with a total of *m* links is determined. The linear velocity and acceleration of a joint are obtained using Equations (9) and (10):

$$[\dot{X}_i\ \dot{Y}_i\ \dot{Z}_i]^T = \sum_{j=1}^{i} \left(A_j [\dot{L}_{xj}\ \dot{L}_{yj}\ \dot{L}_{zj}]^T + \dot{A}_j [L_{xj}\ L_{yj}\ L_{zj}]^T \right) \tag{9}$$

$$\begin{aligned} [\ddot{X}_i\ \ddot{Y}_i\ \ddot{Z}_i]^T = \sum_{j=1}^{i} \Big(& \ddot{A}_j [L_{xj}\ L_{yj}\ L_{zj}]^T + A_j [\ddot{L}_{xj}\ \ddot{L}_{yj}\ \ddot{L}_{zj}]^T \\ & + 2\dot{A}_j [\dot{L}_{xj}\ \dot{L}_{yj}\ \dot{L}_{zj}]^T \Big) \end{aligned} \tag{10}$$

After identifying the pseudo linkage parameters, an industrial robot with the end-effector tool can be modeled using this method. The defining parameters of the system are L_{xi}, L_{yi}, L_{zi}, θ_i, φ_i, and ψ_i of each link that remains constant. In industrial applications, as the robot adds an end-effector tool, the mathematical model also needs to include all parameters of the tool. In the kinematic model of most indus-

trial robots, some of the pseudo link parameters are not utilized and specified as zero. An end-effector tool can be incorporated into the mathematical model either by redefining the unused parameters of the last pseudo link or by adding a new link with all of the tool parameters. Addition of a new link will subsequently increase the number of mathematical operations.

Kinematics of a PUMA 560 Robot

Based on the equations developed thus far, an industrial robot model can be quickly configured and used for task planning. A variety of robotic systems were simulated, based on this technique. For the PUMA 560 robot (see Figure 2), the kinematic model can be represented by four pseudo kinematic links (see Figure 3) with six independent joint angles. The geometric parameters of the system are identified as:

$\theta_1 = -q_1$	$\varphi_1 = \pi/2$	$\psi_1 = q_2$	$L_{x1} = 0$	$L_{y1} = a_2$	$L_{z1} = d_3$
$\theta_2 = -0$	$\varphi_2 = 0$	$\psi_2 = q_3$	$L_{x2} = -d_4$	$L_{y2} = -a_3$	$L_{z2} = 0$
$\theta_3 = -q_4$	$\varphi_3 = \pi/2$	$\psi_3 = 0$	$L_{x3} = 0$	$L_{y3} = 0$	$L_{z3} = 0$
$\theta_4 = -q_5$	$\varphi_4 = \pi$	$\psi_4 = q_6$	$L_{x4} = 0$	$L_{y4} = 0$	$L_{z4} = 0$

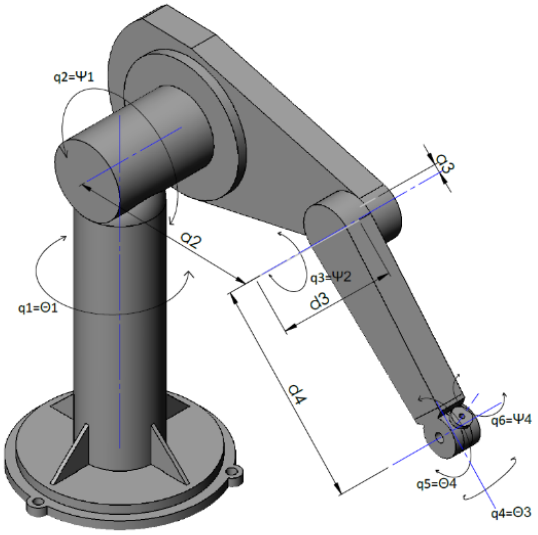

Figure 2. Geometric Parameters of the *PUMA 560* Robot Arm

Accordingly, the position of the robot end-effector is generated by a two-link system using only two transformation matrices:

$$T_2 = \begin{bmatrix} C_3 & -S_3 & 0 \\ S_3 & C_3 & 0 \\ 0 & 0 & 1 \end{bmatrix} \text{ and } T_1 = \begin{bmatrix} C_2 & -S_2 & 0 \\ C_1S_2 & C_1C_2 & -S_1 \\ S_1S_2 & S_1C_2 & C_1 \end{bmatrix}$$

The corresponding end-effector position is given by Equation (11):

$$\begin{bmatrix} X \\ Y \\ Z \end{bmatrix} = \begin{bmatrix} -S_2a_2 & -C_{23}d_4 - S_{23}a_3 \\ C_1C_2a_2 - S_1d_3 & -C_1S_{23}d_4 + C_1C_{23}a_3 \\ S_1C_2a_2 + C_1d_3 & -S_1S_{23}d_4 + S_1C_{23}a_3 \end{bmatrix} \quad (11)$$

where, $C_1 = \cos(q_1)$, $S_{23} = \sin(q_{2+}\, q_3)$, etc.

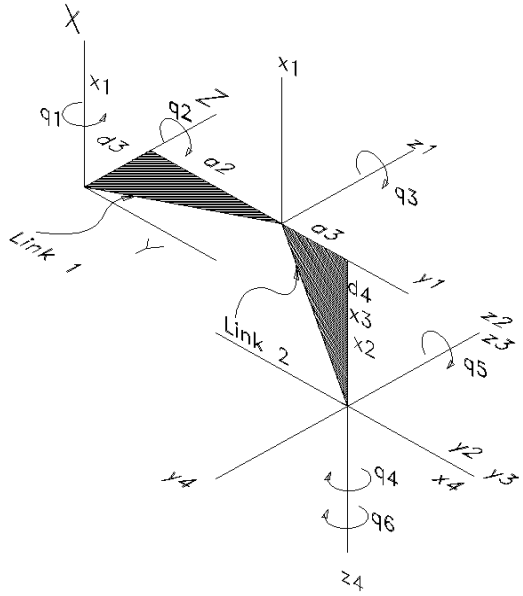

Figure 3. Pseudo Link Representation of the *PUMA 560* Robot

The number of multiplications and additions required in the forgoing development was only 45 and 48, respectively. The same position may be obtained by using the homogeneous transformation matrices of a six-degree-of-freedom serial chain with six links, using the Denavit-Hartenberg notation. This would require 128 additions and 128 multiplications to achieve the same end-effector equation. This amounts to a 63% reduction in computation, when the multi-degree-of-freedom pseudo links are used to represent the same system. Therefore, the procedure would allow for a faster robot response, when such a model is generated online in an automated industrial system.

Kinematics of a Six-Axis Robot

Next, the kinematics of a six-axis industrial robot (FANUC S110) is considered using Equations (1)-(8). After identifying the kinematic parameters of the system, the robot model is represented by four kinematic links with six independent joint angles. The parameters are:

$\theta_1 = -q_1$	$\varphi_1 = \pi/2$	$\psi_1 = q_2$	$L_{x1} = 0$	$L_{y1} = 750$	$L_{z1} = 0$
$\theta = 0$	$\varphi_2 = 0$	$\psi_2 = q_3$	$L_{x2} = -0$	$L_{y2} = 90$	$L_{z2} = 0$
$\theta_3 = q_4$	$\varphi_3 = \pi/2$	$\psi_3 = q_5$	$L_{x3} = 0$	$L_{y3} = 0$	$L_{z3} = 0$
$\theta_4 = \pi/2$	$\varphi_4 = 0$	$\psi_4 = q_6$	$L_{x4} = 0$	$L_{y4} = 10$	$L_{z4} = 100$

In this case, the rotational parameters in radians and translational parameters are in mm. Figures 4 and 5 show the physical system and its pseudo link representation, respectively.

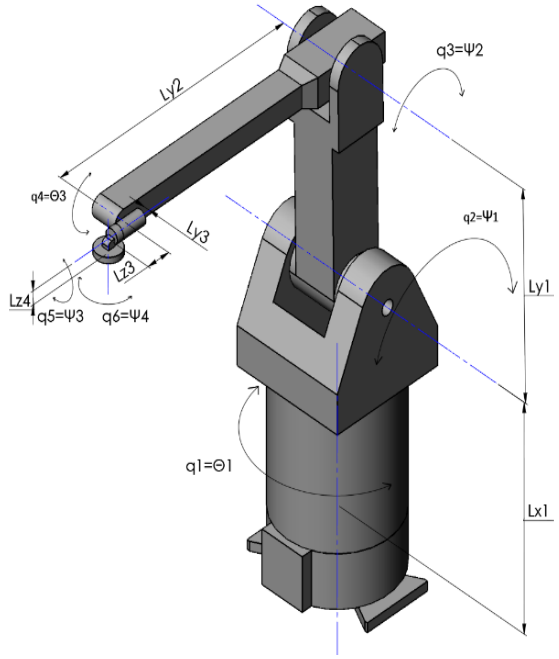

Figure 4. Six-Axis Industrial Robot Arm (FANUC S110)

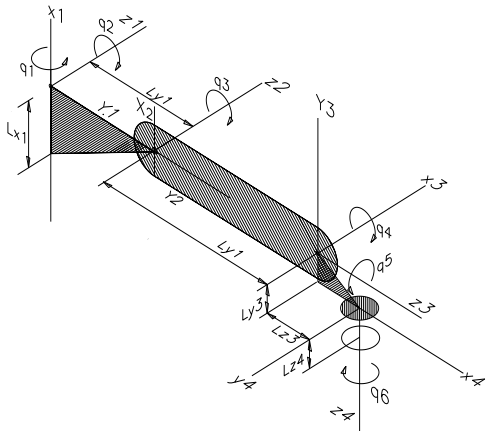

Figure 5. Pseudo Link Representation of the Six-Axis Robot

Using the parameters in Equation (2), the transformation matrices of the links are:

$$T_1 = \begin{bmatrix} C_2 & C_1S_2 & S_1S_2 \\ -S_2 & C_1C_2 & S_1C_2 \\ 0 & -S_1 & C_1 \end{bmatrix}$$

$$T_2 = \begin{bmatrix} C_3 & S_3 & 0 \\ -S_3 & C_3 & 0 \\ 0 & 0 & 1 \end{bmatrix}$$

$$T_3 = \begin{bmatrix} C_3 & C_1S_3 + C_1C_3 & -S_1S_3 \\ -S_3 & C_1C_3 & -S_1C_3 \\ 0 & S_4 & C_4 \end{bmatrix}$$

and

$$T_4 = \begin{bmatrix} 0 & -C_5 & -S_3 \\ 0 & S_5 & -C_3 \\ 1 & 0 & 0 \end{bmatrix}$$

Here, the six-degree-of-freedom system is represented by the four pseudo links. The number of multiplications and additions required for a single set of forward kinematic computations in this system is 117 and 126, respectively. Compared to the solution based on the Denavit-Hartenberg notation of the same problem, it would be a 62% reduction in computation for the robot end-effector position. In robot control, during multiplication of sparsely populated matrices, only the nonzero elements of the matrices are considered. Even under such circumstances, the computation requirement in this method is 45% less than the method using 4x4 homogeneous transformation matrices. Therefore, this kinematic scheme would allow for efficient computation and faster robot response, when such a model is used online in an automated manufacturing environment.

Simulation of Motion

For path planning and motion control of a robotic system, it is imperative that the mathematical model be utilized for the solution of both forward and inverse kinematic problems. In the case of nonlinear mathematical models, the convergence of numerical solutions to generate a smooth continual motion path can be challenging. The linearization of a nonlinear model is a common approach for the approximate solution of the problem. In the following, the kinematic notation is utilized for a solution of the forward and inverse kinematic problem of a system with four-link and twelve-degree-of-freedom system. For a unique solution of the inverse kinematic problem of a redundant system, the optimization of an objective function may be used, as shown by Equation (12). Here, the objective function is defined as the weighted sum of the joint displacements and joint angles.

$$f(q_1,q_2,...,q_n) = \sum_{i=1}^{m} w_i \Delta S_i + \sum_{j=1}^{n} v_j q_j \qquad (12)$$

where, w_i and v_i are the weighting functions for joint displacement ΔS_i and joint variable q_i, respectively.

For an industrial robotic system, the user needs to identify the kinematic constraint and weighting functions prior to a motion planning or simulation task. Table 1 presents the XYZ coordinates and nutation, precession, and spin angles [11] of the end-effector and defines its path as a continuous trajectory. Corresponding joint angles are determined by solving the inverse kinematic problem and presented in Table 2. The goal state of the four-link twelve-degree-of-freedom system in Table 1 was recalculated using the joint angles presented in Table 2. Absolute error in the end-effector position and orientation compared to the numerical solution of the inverse kinematics problem is less than 0.0001%. In spite of the nonlinear nature of the kinematic scheme, a numerical solution produces a continuously variable smooth trajectory for the given end-effector position and orientation. The method can also be used to generate a kinematic model of an existing system and solve the inverse kinematic problem for path planning or motion control. Similarly, the method can be adapted to generate a kinematic model of a more complex mechanical chain with constraints between the joints of the chain.

Conclusions

The kinematic model of an industrial robotic system was developed by using multi-degree-of-freedom pseudo kinematic linkages and modified Eulerian angle parameters. A solution of the forward kinematic problem based on this notation is computationally more efficient compared to existing methods. In a manufacturing environment, where the kinematic structure of a robot may change frequently, due to the adoption of different types of end-effector tools, this method will reduce the computational burden of the system and allow for faster motion planning, simulation, analysis, and control. To demonstrate the versatility of this method, the inverse kinematic problem of a redundant system was also solved. Using the kinematic model, an optimization process solves the inverse kinematic problem and generates a smooth trajectory of a joint and end-effector motion path.

References

[1] Cohn, A., & Hazarika, S. (2001). Qualitative Spatial Representation and Reasoning: An Overview. *Fundamenta Informaticae, 46*(1-2), 1-29.

[2] Liu, H., & Coghill, G. (2005). Fuzzy qualitative trigonometry. *Proceedings of the IEEE International Conference on Systems, Man and Cybernetics*, (pp.1291-1296). Hawaii, USA.

Table 1. Initial and Goal State of a Four-Links System

Inst.	X	Y	Z	Nutation	Precession	Spin
Initial state of the end-effector (in meters and degrees)						
0	2.382	2.43	1.1459	53.6856	7.4579	70.900
Goal state of the end-effector						
1	2.465	2.297	1.0776	49.8102	12.1252	77.636
2	2.512	2.123	0.9869	46.5735	15.8337	82.694
3	2.531	1.923	0.8332	43.8337	18.7821	86.421
4	2.531	1.715	0.7759	41.4401	21.2422	89.294
5	2.524	1.515	0.6738	39.1482	23.534	91.873
6	2.524	1.334	0.5825	36.7441	25.994	94.745
7	2.542	1.178	0.5048	34.0145	28.9424	98.473
8	2.587	1.050	0.4411	30.778	32.6513	103.53
9	2.667	0.947	0.3902	26.9026	37.3186	110.27
10	2.787	0.867	0.3502	22.319	43.0481	118.86

Table 2. Initial and Goal States of the Four-Links System with Twelve Degrees of Freedom

Instant	θ1	ϕ1	ψ1	θ2	ϕ2	ψ2
Initial joint variables (in degrees)						
0	60	45	-60	-30	-25.71	45
Joint variables in goal states						
1	56.43	37.42	-63.64	-37.35	-28.63	45.91
2	53.21	30.01	-66.84	-44.14	-31.57	46.73
3	50.39	23.54	-69.8	-50.23	-34.96	47.3
4	48.16	18.66	-72.88	-55.13	-38.54	47.76
5	47	14.95	-76.1	-58.74	-41.95	48.05
6	47.06	12.58	-79.47	-60.97	-45.09	47.97
7	48.61	10.82	-82.98	-61.56	-47.97	47.49
8	52.19	8.31	-86.44	-60.04	-50.08	46.28
9	57.71	6.52	-90.05	-56.14	-51.65	44.88
10	66.78	5.18	-92.87	-47.2	-52.4	43.43

Instant	θ3	ϕ3	ψ3	θ4	ϕ4	ψ4
Initial joint variables (in degrees)						
0	20	22.5	-45	60	-25.71	-18
Joint variables in goal states						
1	26.5	25.75	-47.34	63.61	-35.99	-10.47
2	33.46	28.07	-49.07	70.63	-44.21	-4.29
3	40.08	28.88	-49.94	79.09	-50.4	1.02
4	45.63	29.09	-49.84	87.87	-55.28	5.71
5	49.39	28.88	-49.51	96.2	-59.3	9.74
6	50.96	27.93	-48.88	103.31	-62.98	13.59
7	49.86	26.64	-48.54	108.9	-66.54	17.05
8	46.05	25.4	-49.12	112.67	-70.1	19.72
9	38.77	23.06	-49.44	113.67	-73.82	23.13
10	28.51	20.53	-49.95	111.72	-77.81	27.18

[3] Lin, J., & Lewis, F. (2007). Qualitative kinematics of planar robots: Intelligent connection. *International Journal of Approximate Reasoning, 46*(3), 525-541.
[4] Lin, J., & Lewis, A. (1994). Symbolic Formulation of Dynamic Equations for a Manipulator with Rigid and Flexible Links. *International Journal of Robotics Research, 13*(5), 454-466.
[5] Steinbauer, G., & Wotawa, F. (2007). Combining Quantitative and Qualitative Models with Active Observations for better Diagnoses of Autonomous Mobile Robots. IEEE Fifth Workshop on Intelligent Solutions in Embedded Systems, 216-226.
[6] Denavit, J., & Hartenberg, S. (1955). A Kinematic Notation for Lower-Pair Mechanisms Based on Matrices. *Journal of Applied Mechanics, 77*(2), 215-221.
[7] Paul, P. (1981). *Robot Manipulators: Mathematics, Programming and Control*. The MIT Press, Cambridge, MA, USA.
[8] Whitney, E., & Lozinski, A. (1984). Industrial Robot Calibration Methods and Results. *Proceedings of the International Computers in Engineering Conference,* (pp.92-100). ASME, New York.
[9] Wang, X., Baron, L., & Cloutier, G. (2008) Topology of Serial and parallel manipulators and topological diagrams. *Mechanism and Machine Theory, 43*(6), 754-770.
[10] Valsamos, C., Moulianitis, V., & Aspragathos, N. (2014). Kinematic Synthesis of Structures for Metamorphic Serial Manipulators. *Journal of Mechanism and Robotics*, *6*(4), 1-29.
[11] Choudhury, A., & Genin, J. (1989). Kinematics of an n-degree-of-freedom multi-link robotic system. *International Journal of Robotic Research, 8*(6), 132-140.
[12] Choudhury, A., Rodriguez, J., Keil, M., & Ramrattan, S. (2002). Efficient Reconfiguration of Industrial Robots for Casting Operation. *Proceedings of the 7th Annual International Conference on Industrial Engineering – Theory, Applications, and Practice*, Pusan, Korea.

Biographies

ALAMGIR CHOUDHURY completed his MS (1985) and PhD (1990) in mechanical engineering from New Mexico State University. He received the BS in mechanical engineering from Bangladesh University of Engineering and Technology, Dhaka, Bangladesh, in 1977. He is an associate professor of engineering design, manufacturing and management systems at Western Michigan University. His industrial experience includes mechanical engineer in a power plant and design engineer in a natural gas transmission and distribution company. His research interests include energy efficiency in product and system design, computer applications in curriculum, mechanics, fluid power, and instrumentation and control. He has over 75 articles published in journals and conference proceedings. Dr. Choudhury may be reached at alamgir.choudhury@wmich.edu

JORGE RODRIGUEZ is an associate professor in the Department of Engineering Design, Manufacturing, and Management Systems (EDMMS) at Western Michigan University's College of Engineering and Applied Sciences. He is the co-director of the Center for Integrated Design, and Research Associate of the Human Performance Institute. He received his PhD in mechanical engineering design from the University of Wisconsin-Madison and MBA from Rutgers University. He teaches courses in CAD/CAE, mechanical design, finite element methods and optimization. His research interests include product development, topology optimization, additive manufacturing, and biomechanics. He also worked as design engineer and project engineer in the steelmaking industry, and consults on product re-engineering and computer-based analysis. Dr. Rodriguez may be reached at jorge.rodriguez@wmich.edu

MITCHEL KEIL is a professor in the Department of Engineering Design, Manufacturing, and Management Systems. He has 21 years of experience teaching over 20 graduate and undergraduate courses. He has more than 70 publications as journal articles, conference papers, and technical reports, and holds eight patents—three in the United States and five international. He has obtained more than $5 million in research and educational funding from government agencies and private companies, including Chrysler, the National Transportation Research Center, the Society of Manufacturing Engineers, and Litton Industries (now Moog). He is a registered professional engineer in the State of Florida and has 15 years of industrial experience at Bethlehem Steel, Motorola, and Litton Industries. Dr. Keil may be reached at mitchel.keil@wmich.edu

DEMAND-SIDE MANAGEMENT OF 33KV FEEDERS IN A 132KV INJECTION SUBSTATION USING AN INTERRUPTIBLE DIRECT LOAD APPROACH

Thomas Olabode Ale, Federal University of Technology, Nigeria;
Agbeniyi Adebusuyi James, Obafemi Awolowo University Teaching Hospital Complex, Nigeria

Abstract

Inconsistency in the delivery of electrical energy is at a critical stage in Nigeria, which could be as a result of many factors, including the electrical energy management scheme employed by the utility supplier. An electronic-based demand-side management scheme is a better alternative to the current management scheme. In this paper, the authors focus on managing the electrical energy supplied to consumers on six 33kV feeders in a 132kV injection substation. The intelligent system integrates the bulk power (50MVA) from the national control center with the six feeder links in the injection substation, while allocating electrical power to the feeders with respect to energy demand by the consumer. The study reshaped the load and energy demand curve by cycling customer loads, while prioritizing customer preferences. Data from power utilities were gathered and analyzed using tools to generate waveform patterns for energy consumption. This energy management scheme was executed in the Simulink environment with the implementation of a genetic algorithm as the optimization tool.

Introduction

The instability of the supply of electrical energy to consumers in Nigeria is increasing geometrically with respect to technological and societal development. The effects of societal and technological growth diversity have had a great impact on electrical energy supply, due to an increase in demand. Economically, the present load demand on the Nigerian power supply system could be attributed to power shortages and, thus, account for higher costs. These factors could contribute to the inconsistency in power delivery. Although, the lack of knowledge of electric load management by the end users (customers) could also be a contributing factor in power supply efficiency, as a result of increasing the energy demand. To evaluate the power system, there is a need to study the efficiency of the national grid (transmission and distribution). To do so, one must take into cognisance the estimated total generating capacity of the Nigerian electrical energy generating stations, the total distributed energy to the consumers, and energy loss on transmission lines. The efficiency parameter serves as a guide for effective management of energy indices of consumption with varying loads, which could be a major factor in the overall energy loss at the distribution end [1]. The ability to efficiently coordinate available electrical energy generated in order to meet standard requirements from the demand side is referred to as Demand Side Management. Demand side management is a technical move to reduce utility consumption by modifying the energy pattern, such as interruptible load rescheduling [1]. Load management is the process of scheduling the loads to reduce electric energy consumption and/or maximum demand [2]. Controllable loads are often isolated during peak periods on respective feeders in order to clip the peak periods, while the uncontrollable loads remains on to fill the valley periods.

Knowledge Management Transformation Technology

The direct load control management technique is a program designed to interrupt consumer loads during peak hours by directly controlling consumers' individual appliances [3]. And while it is highly economical from a supply side point of view by saving generating capacity, its effect on the demand side is manifested in occasional blackouts, without preference to the consumers' needs. The blackouts are often attributed to feeder failures as a result of feeder overloading on consumer premises. Direct load control is implemented using two approaches: interruptible load control and time-of-use tariff.

Both approaches are characterized by intermittent switching-off of feeders by the utility supplier, which is reflected as a blackout on the consumer premises, unlike demand-side management, as introduced in this study, which is implemented by turning off only scheduled loads on consumer premises, thus eliminating blackouts. Embedded system technology is introduced as a control interface on the loads using PID controllers for data acquisition and command execution on consumer premises, while serving to support monitoring and command issuance at the utility with the implementation of a genetic algorithm. The microcontroller was coded with MATLAB and simulated on Simulink. A radio frequency transceiver was incorporated onto the em-

bedded controller switch to receive commands from the control unit and also to send acquired data to the main control unit for appropriate instructions.

Operating Principle and Knowledge Creation

Due to a lack of proper implementation of an electrical energy management scheme for Nigeria's power system end users, the authors of this study designed an intelligent system that comparatively samples energy consumption wave patterns of different areas on a feeder (intra-feeder supply) or consumption rate on different feeders (inter-feeder supply) with respect to allocated power on the substation. An embedded control unit was sited at the substation to monitor the quantity of energy demand by consumers on the feeders, in comparison with available energy from the substation by the national control center. A subsidiary embedded control device was implemented on the consumer side to control the ON and OFF timing of the controllable loads, as agreed upon by the end users. Communications between the embedded systems were established with radio frequency signals. Figure 1 shows the block diagram of the simulation.

33kV Injection Substation

Figure 2 shows the load profile for individual feeders acquired from previous data recorded at the substation were fed into the embedded system on the 33kV feeders in the injection substation to analyze the behavioral characteristics of the feeders in reaction to the load demand. A three-phase measuring device was implemented to measure instantaneous V-I at the substation using Equations (1)-(4):

$$V_{abc}\left(pu\right) = \frac{V_{phase\ to\ phase}\left(V\right)}{V_{base}\left(V\right)} \tag{1}$$

$$V_{base} = V_{nom}\left(V_{rms}\right) \cdot \sqrt{2} \tag{2}$$

$$I_{abc}\left(pu\right) = \frac{I_{abc}\left(A\right)}{I_{base}\left(A\right)} \tag{3}$$

$$I_{base} = \frac{P_{base}}{V_{nom}} \times \frac{\sqrt{2}}{\sqrt{3}} \tag{4}$$

where, V_{abc} and I_{abc} are the phase-phase voltages and currents in *pu*, respectively.

Computation of true root mean square values of input signals from the 132kV substation was implemented using an rms calculator by executing Equation (5) on the substation:

$$rms, y_{(t)} = \sqrt{\frac{1}{T}\int_{t-T}^{t} y_{(t)}^{2}} \tag{5}$$

where, $y_{(t)}$ is the function of the input signal and $\frac{1}{T}$ is the fundamental frequency (50Hz).

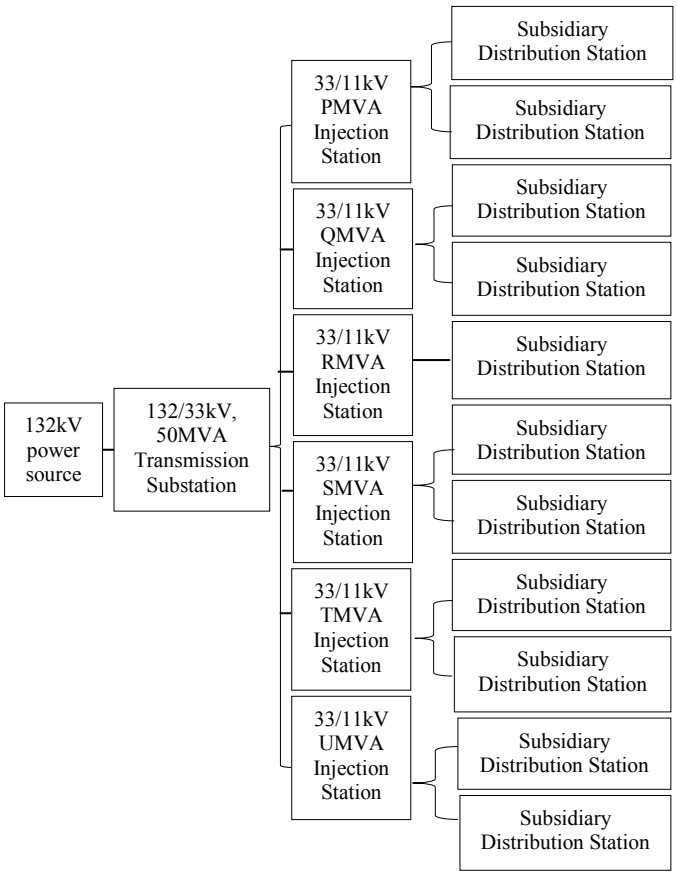

Figure 1. Block Diagram of Simulink Implementation of Interruptible Direct Load Scheme

Appendix 1 shows that the commands from the injection station were executed by the implementation of a genetic algorithm on the PID controller.

Implementation of the Substation Algorithm

The genetic algorithm schedules the controllable loads filling the valley periods that often result from feeder collapse in response to feeder state. The algorithm executes implementation beginning with a set of solutions [4] that is represented as the data acquired from the feeders in the form of a feeder load profile. Codes were generated from the function parameters [5] that included optimization state (ON), profiled power, input power, switch state, power de-

mand (MVA), and allocated power (MVA). The initial population for the load profile was created using Equations (6) and (7):

$$S_p = \sqrt{P^2 + jQ^2} \tag{6}$$

$$diff.,\delta = \frac{(P_o - P)}{P_o} \tag{7}$$

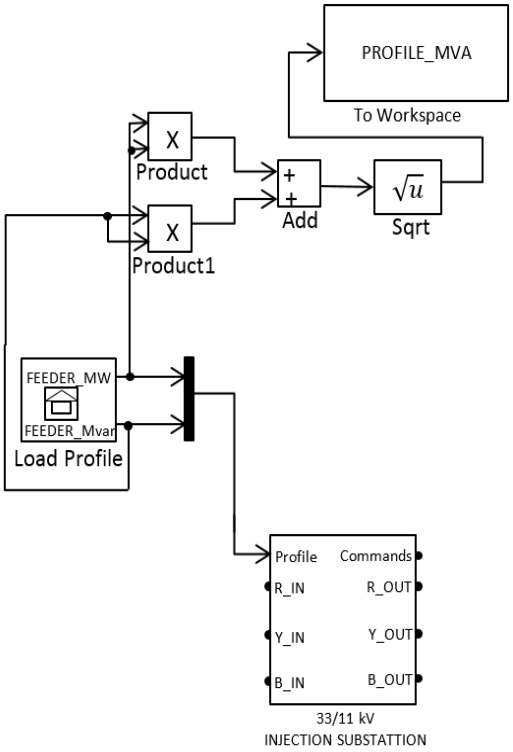

Figure 2. Load Profile

Fitness parameters for differential reference power were executed using Equations (8) and (9), such that if $\delta > t$ and abs.(δ) > t then:

$$S_p = P_o(1-t) \tag{8}$$

and if $\delta > t$ and abs.(δ) > t then:

$$S_p = P_o(1+t) \tag{9}$$

where, S_p is the total power demand in MVA; P and Q are profiled real and reactive power, respectively; P_o is initial profiled power; δ is the differential ratio of reference power; and, t is the time constant (0.08).

Figure 3 shows the flowchart of the algorithm implemented by the centralized coordinator.

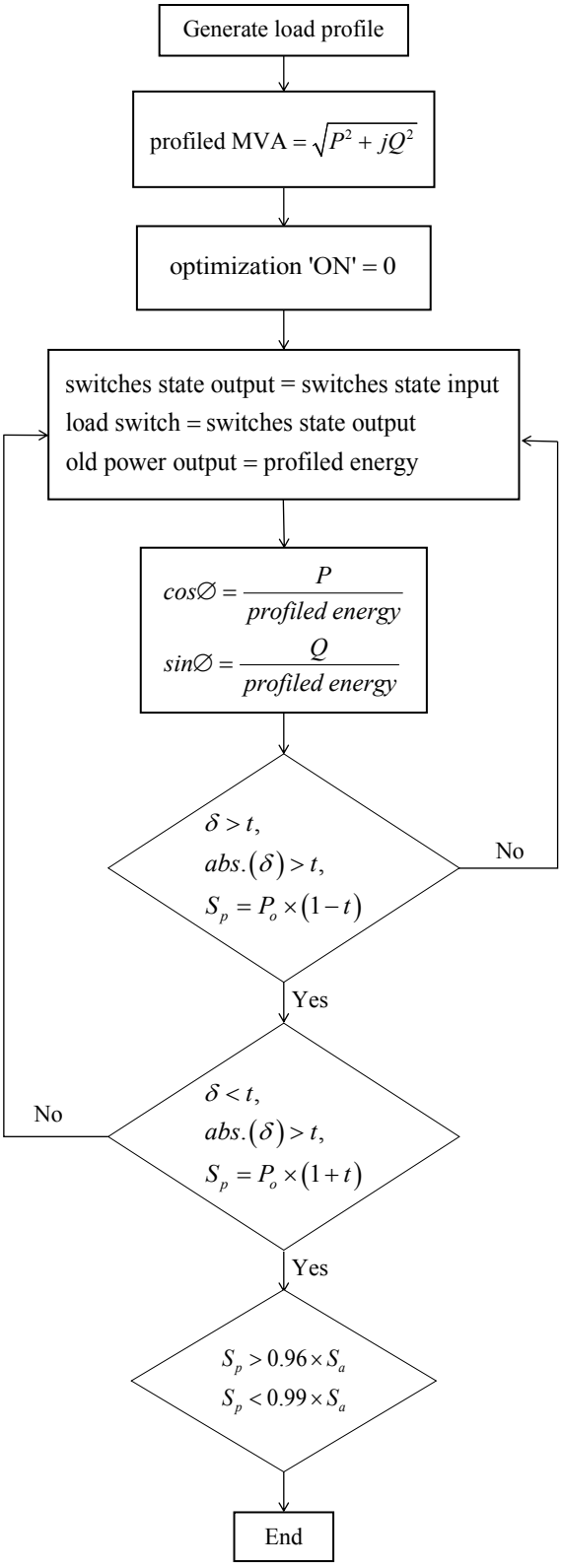

Figure 3. Flowchart of Central Coordinator Algorithm

Consumer Load Control Units

Individual addresses are allocated to consumer loads with respect to load addresses allocated to address identifiers implemented on the embedded system at the injection substation. Commands from the injection substation are executed on the loads to isolate identified loads during peak periods in order to clip the peak and turn ON other loads during valley periods in order to fill the valley of the load profile. Appendix 2 describes the algorithm for the implementation of consumer load control using the Simulink connections of Figure 4. The active and reactive power of the three-phase loads vary as a function of positive sequence voltage, on the assumption that the load currents are even in an unbalanced situation. Variations in the active and reactive power during simulation were implemented using Equations (10) and (11), when load impedance is constant at a lower voltage value compared to the terminal voltage:

$$P_{(s)} = P_o\left(\frac{V}{V_o}\right)^{n_p} \cdot \frac{1+T_{p1s}}{1+T_{p2s}} \tag{10}$$

$$Q_{(s)} = Q_o\left(\frac{V}{V_o}\right)^{n_q} \cdot \frac{1+T_{q1s}}{1+T_{q2s}} \tag{11}$$

where, V_o is the initial positive sequence voltage; P_o and Q_o are the initial active and reactive powers, respectively, at the initial voltage, V_o; V is the positive sequence voltage; n_p and n_q are exponents (ranging between 1 and 3) controlling the nature of the load; T_{p1} and T_{p2} are time constants controlling the dynamics of the active power, P; and, T_{q1} and T_{q2} are time constants controlling the dynamics of the reactive power.

Implementation of the Load Control Algorithm

Figure 5 shows the individual load profiles of each feeder as they are updated at each iteration implemented by the algorithm with respect to the control signal broadcast by the centralized coordinator. Although direct load control instructions are executed by algorithms implemented on consumer premises [6-9], the centralized algorithm primarily coordinates the decisions of the feeders [10-13]. Equations (12) and (13) determine the commands broadcast to loads at the consumer premises.

For a schedulable load to be ON:

$$S_p < 0.99 \times S_a \tag{12}$$

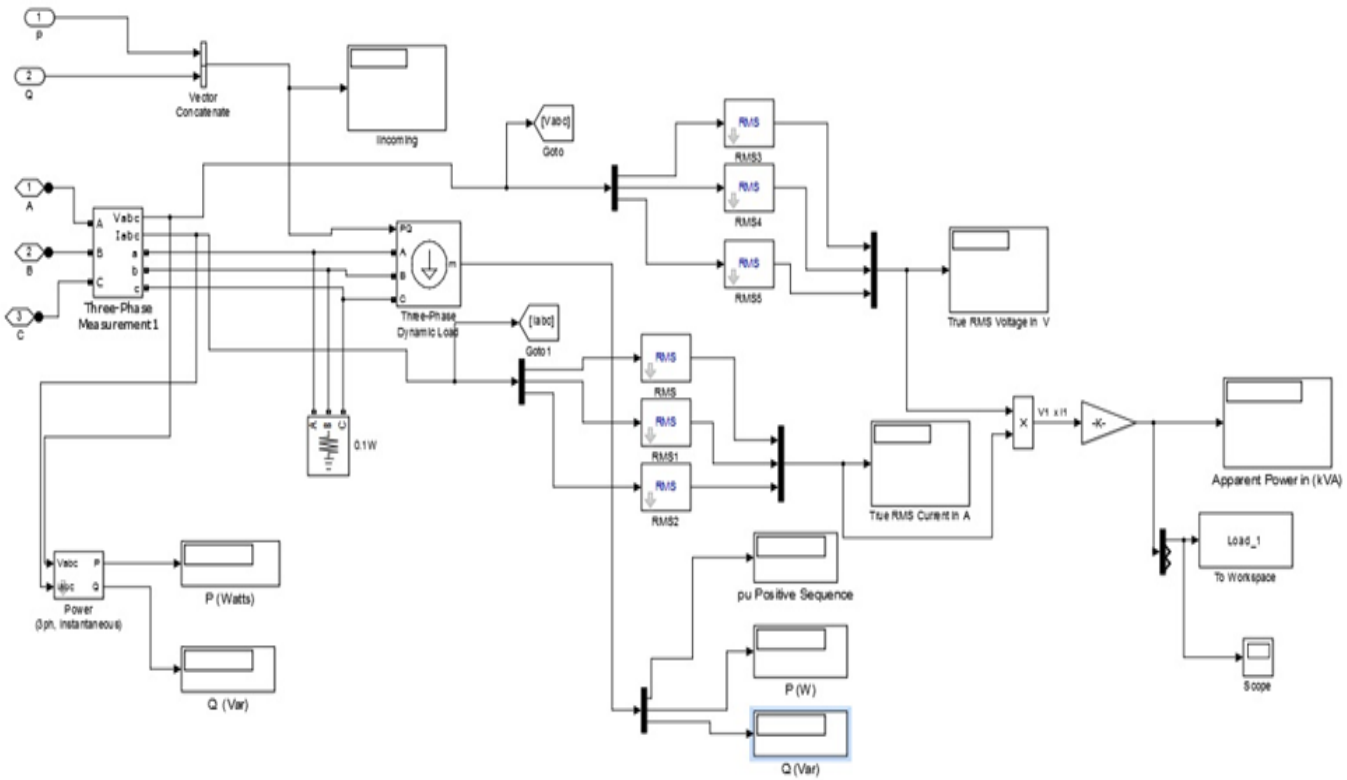

Figure 4. Consumer Load Control Unit

For a schedulable load to be OFF:

$$S_p > 0.96 \times S_a \quad (13)$$

where, S_a is feeder allocated power in MVA.

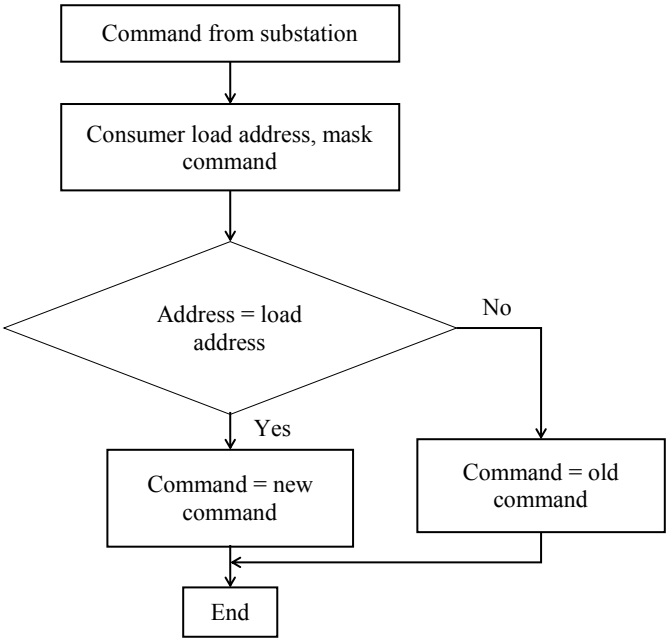

Figure 5. Flowchart of the Load Control Algorithm

Results

It was observed from the pattern revealed in Figure 4 that total blackouts were experienced shortly after the feeder approaches the peak period on the non-optimized outputs. This could be as a result of the stress on the feeders at peak periods [14]. This anomalous behavior was corrected by the compensation rendered through clipping and filling of the sharp peak and valley periods, respectively. The management scheme intelligently senses a rise in energy demand on each feeder and the concurrent decline in energy demand on subsequent feeders and, thus, isolates the controllable loads on peak feeders, while reshaping the expected sharp peak period to compensate for the sharp decline experienced on subsequent feeders. Figure 6 shows the displayed optimization results for the six feeders in the 132kV injection substation with allocated power of 3.7 MVA, 8 MVA, 7 MVA, 6.5 MVA, 8 MVA, and 4.5 MVA in Figures 6(a)-(f), respectively. The un-optimized path is the standard load profile without optimization that often results in blackouts on consumer premises as a result of area load shedding. The optimized paths eradicated blackouts and possible brownouts through interruptible direct load control on consumer premises.

Conclusions

A load management scheme that catered to consumers was established, while ensuring high-power quality by the total eradication of blackouts as shown from the data. The system can be implemented on any substation regardless of the energy supply or demand on the substation. The maximum tolerable voltage and minimum expected voltage for each feeder would be factored into the system parameters. From the results of this project, it was established that one major cause of the unstable power supply in Nigeria can be attributed to poor or ineffective electrical energy management schemes, among other factors. Implementation of the system developed in this study will reduce the epileptic electric power supply to a minimum. This strategy has been proposed to balance the power use over time, while technically adjusting the cost of energy so that both the utility company and the end user may benefit. Inefficiency in the electrical energy supply and waste can best be minimized through energy diversification and an effective approach to load management [15]. The idea that electrical energy instability experienced in Nigeria is due to poor management is not a far-fetched concept. So, considering the advantages of the technology presented here, the overall power system and its adaptability can be optimized.

References

[1] Bhatia, B. E. (2012). *Power factor in electrical energy management.* Manuscript submitted for publication.

[2] Eissa, M. M., Wasfy, S. M., & Sallam, M. M. (2012). *Load management system using intelligent monitoring and control system for commercial and industrial sectors.* Unpublished manuscript, Helwan Department of Electrical Engineering, Helwan university, Cairo, Egypt.

[3] Benergee, R. (1998). Load management in the Indian power sector using US experience. *Energy, 23*(11), 961-972.

[4] Chakraborty, R. C. (2010). Fundamentals of genetic algorithms. [AI course lecture 39-40, notes, slides]. Retrieved from www.myreaders.info/html/artificial_intelligence.html

[5] Prasanth, B. V., & Kumar, S. V. (2008). *Load frequency control for a two area interconnected power system using robust genetic algorithm controller*. Manuscript submitted for publication.

[6] Caramanis, M., & Foster, J. M. (2009). Management of electric vehicle charging to mitigate renewable generation intermittency and distribution network

congestion. *IEEE Conference on Decision and Control*, (pp. 4717–4722).

[7] Gan, L., Topcu, U., & Low, S. (2013). Optimal decentralized protocol for electric vehicle charging. *IEEE Transactions on Power Systems, 28*(2), 940–951.

[8] Ma, Z., Callaway, D. S., & Hiskens, I. A. (2013). Decentralized charging control of large populations of plug-in electric vehicles. *IEEE Transactions on Control Systems Technology, 21*(1), 67–78.

[9] Rotering, N., & Ilic, M. (2011). Optimal charge control of plug-in hybrid electric vehicles in deregulated electricity markets. *IEEE Transactions on Power Systems, 26*(3), 1021–1029.

[10] Qian, K., Zhou, C., Allan, M., & Yuan, Y. (2011). Modeling of load demand due to electric vehicle battery charging in distribution systems. *IEEE Transactions on Power Systems, 26*(2), 802–810.

[11] Richardson, P., Flynn, D., & Keane, A. (2012). Optimal charging of electric vehicles in low-voltage distribution systems. *IEEE Transactions on Power Systems, 27*(1), 268–279.

[12] Sundstrom, O., & Binding, C. (2010). Planning electric-drive vehicle charging under constrained grid Conditions. *International Conference on Power System Technology.*

[13] Verzijlbergh, R. A., Grond, M. O., Lukszo, Z., Slootweg, J. G., & Ilic, M. D. (2012). Network impacts and cost savings of controlled electric vehicle charging. *IEEE Transactions on Smart Grid, 3*(3), 1203–1212.

[14] Wu, L., Anderson, R., Boulanger, A., Rudin, C., & Kaiser, G. (2012). *Failure Analysis of the New York City Power Grid.* Manuscript submitted for publication.

[15] Oyedepo, S. O. (2012). Energy sustainability and development in Nigeria. *Energy sustainability and society.* Retrieved from http://www.energysustainsoc.com/

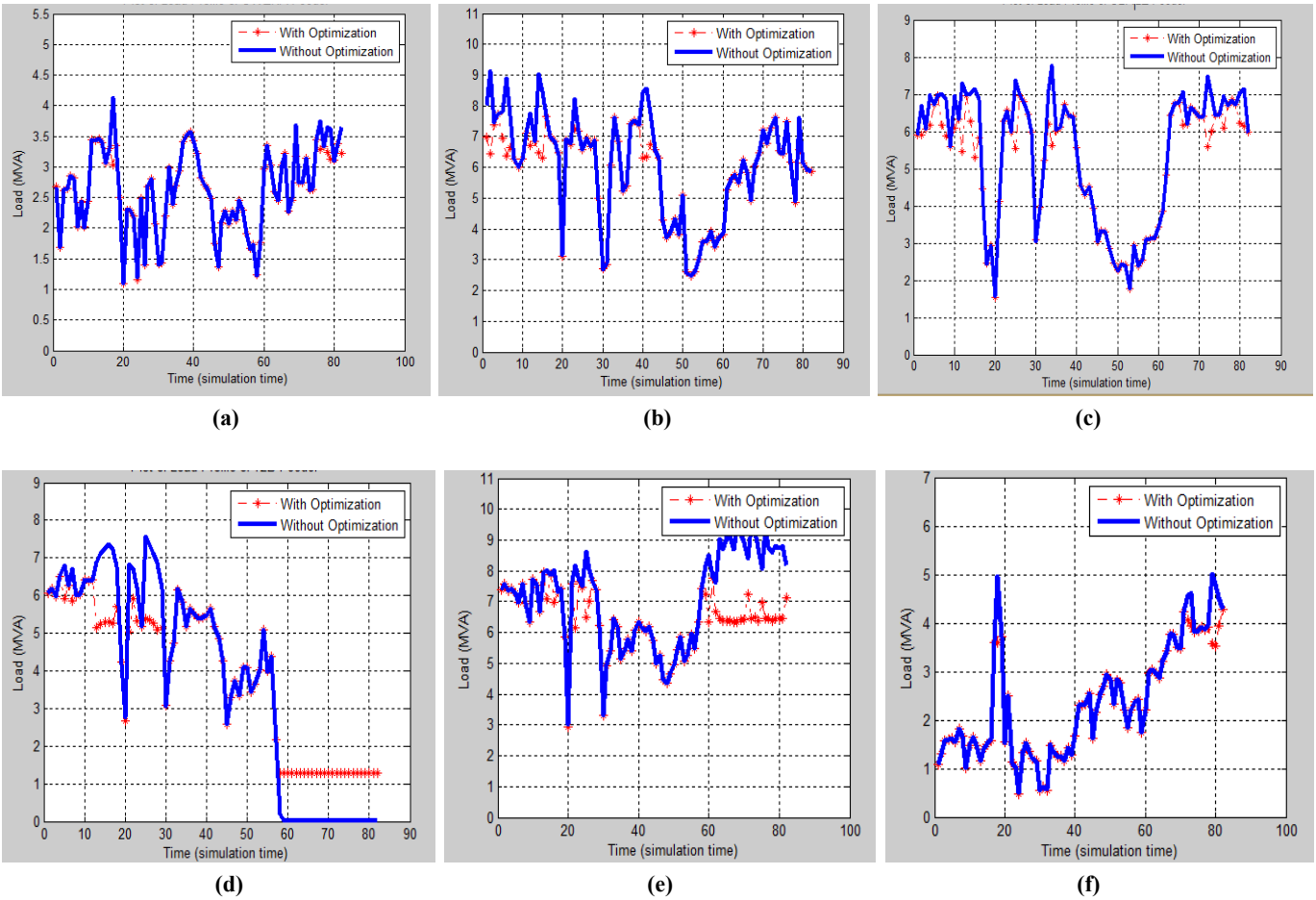

Figure 6. Load Profiles of Feeders under Study

Appendix 1

Implementation of a genetic algorithm on an embedded PID controller.

```
function[Comand,Old_Power_OUT, Switches_State_out]=fcn
(Optimi-
zatn_ON,Profiled_power,Old_Power_IN,Switches_State_in,Power
_Demand_in_MVA,allocated_Power_in_MVA;
%#codegen
Comand = zeros(3,1, 'double');
CONSUMER_ADDRESS = uint16(65280);
%0xFF00%Broadcast Address
Profiled_MVA=sqrt(Profiled_power(1,1)^2 + Profiled_power(2,1)
^2);
if(Optimizatn_ON~=0
if(Profiled_MVA==0)
S=Old_Power_IN(11;
P=Old_Power_IN(2,1);
Q=sqrt(S^2-P^2);
Profiled_power(1,1)=P; Profiled_power(2,1)=Q;
Profiled_MVA=S;
end
end
if(Optimizatn_ON=0)Switches_State_out=Switches_State_in;
Appliances_to_Switch=unit16(Switches_State_out);
Cmd=uint16(bitor
(CONSUMER_ADDRESS,Appliances_to_Switch));
Cmd=double(Cmd);
Comand=[Profiled_power;Cmd];
cosPhi=0.8;
% not really needed.
Old_Power_OUT=[Profiled_MVA;Profiled_MVA*cosPhi];
return;
end
if (Profiled_MVA ~= 0)
cosPhi=Profiled_power(1,1)/Profiled_MVA;
sinPhi=Profiled_power(2,1)/Profiled_MVA;
else
cosPhi=1.0;
sinPhi=1.0;
end
tol=0.08;
old_P=Old_Power_IN(1,1);
if (old_P~=0)
diff=(old_P-Profiled_MVA)/old_P;
if ((diff > tol)&(abs(diff)>tol))
 Profiled_MVA=old_P*(1-tol);
elseif((diff<tol)&(abs(diff)>tol))Profiled_MVA = old_P*(1 + tol);
end
end
if((Profiled_MVA>0.96*allocated_Power_in_MVA)&
(Profiled_MVA<0.99*allocated_Power_in_MVA))
Switches_State_out = uint8(255);
%Switches_State_out=Switches_State_in;
Appliances_to_Switch=unit16(Switches_State_out);
Cmd=unit16(bitor
(CONSUMER_ADDRESS,Appliances_to_Switch));
Cmd=double(Cmd);
Comand=[Profiled_power;Cmd];
Old_Power_OUT=[Profiled_MVA;Profiled_MVA*cosPhi];
return
end
%end
%x>1
%Switches_State_out=Switches_State_in;
%Appliances_to_Switch=unit16(Switches_State_out);
%x=unit16(bitor
(CONSUMER_ADDRESS,Appliances_to_Switch));
%unit16
%Comand(1:3,:)=[0;1;2]; %Profiled_power;
%[Profiled_power;y];
%Comand(3,:)=y;
%Old_Power_OUT=45;
%Profiled_MVA;
%Cmd=unit16(bitor(CONSUMER_ADDRESS,uint16
(Appliances_to_Switch)));
%Cmd=double(Cmd);
%Comand=[Profiled_power;Cmd];
%return;
Power_Demand_in_MVA=Profiled_MVA;
%Implement Binary Genetic Algorithm Control Here
%step 1 Setup the GA
%fit_func=@Select_Switch_Genetically; %objective function
fit_func='Select_Switch_Genetically'; %objective function
npar=1;
%number of optimization variables
%step 2 Stopping criteria
maxit=20;
%max number of iterations
mincost=0.0000;
%minimum cost
%step 3 GA parameters
population_size=16;
%set population size
mutation_rate=.15;
%set mutation rate
selection=0.5;
%fraction of population kept
nbits=8;
%number of bits in each
%parameter
 Nt=nbits*npar;
%total number of bits in a chormosome
keep=floor(selection*population_size);
%#population members that survive
%variable declaration
temporary_Pop=zeros(population_size, 'double');
minc=zeros(maxit, 'double');
meanc=zeros(maxit, 'double');
cost=zeros(population_size,1,'double');
%step 4 Create the initial population
iga=0;
%generation counter initialized
population=round(rand(population_size,Nt));
```

```
%random population of 1s and 0s
%cost=feval
(fit_func,population,Power_Demand_in_MVA,allocated_Power_i
n_MVA);
%calculates population cost using fit_func
cost=Select_Switch_Genetically
(popula-
tion,Power_Demand_in_MVA,allocated_Power_in_MVA);
%calculates population cost using fit_func
[cost,ind]=sort(cost);
% min cost in element 1
%par=par(ind,:);
temporary_Pop = ind;
%populatn = population(ind,:);
population= population(temporary_Pop,:);
% sorts population with lowest cost first
minc(1)=min(cost);
% minc contains min of population
meanc(1)=mean(cost);
% meanc contains mean of population
% step 5 Iterate through generations
while iga<maxit
iga=iga+1;
% increments generation counter
% Pair and mate
M=ceil((population_size-keep)/2);
% number of matings
prob=flipud([1:keep]'/sum([1:keep]));
% weights chromosomes based upon position in list
odds=[0 cumsum(prob(1:keep))'];
% probability distribution function
pick1=rand(1,M);
% mate #1
pick2=rand(1,M);
% mate #2
%mama and papa contain the indicies of the chromosomes that
will mate
ic=1;
%ma = zeros(M);
pa = zeros(M);
mama = zeros(1, M, 'double');
papa = zeros(1, M, 'double');
while ic<=M
for id=2:keep+1
if pick1(ic)<=odds(id) && pick1(ic)>odds(id-1)
mama(ic)=id-1;
end
% if
if pick2(ic)<=odds(id) && pick2(ic)>odds(id-1)
papa(ic)=id-1;
end
% if
end
% id
ic=ic+1;
end
% while
% Performs mating using single point crossover
ix=1:2:keep;
% index of mate #1
xp=ceil(rand(1,M)*(Nt-1));
% crossover point
sub_pop = size(mama, 2);
% no of cols
allele = xp(1);
% first element determines
mama_genes = zeros(sub_pop,allele,'double');
papa_genes2 = zeros(sub_pop,allele,'double');
papa_genes = zeros(sub_pop,Nt-allele,'double');
mama_genes2 = zeros(sub_pop,Nt-allele,'double');
for indexp = 1:allele
mama_genes(:,indexp) = population(mama,indexp);
papa_genes2(:,indexp) = population(papa,indexp);
end
indexm = 1;
for indexp = (allele+1):Nt
papa_genes(:,indexm) = population(papa,indexp);
mama_genes2(:,indexm) = population(mama,indexp);
indexm = indexm + 1;
end
population(keep+ix,:)=[mama_genes papa_genes];
% first offspring
population(keep+ix+1,:)=[papa_genes2 mama_genes2]; % second
offspring
%population(keep+ix,:)=[population(mama,1:xp) population
(papa,xp+1:Nt)]; % first offspring
%population(keep+ix+1,:)=[population(papa,1:xp) population
(mama,xp+1:Nt)]; % second offspring
% Mutate the population
nmut=ceil((population_size-1)*Nt*mutation_rate);
% total number of mutations
mrow=ceil(rand(1,nmut)*(population_size-1))+1;
% row to mutate
mcol=ceil(rand(1,nmut)*Nt);
% column to mutate
for ii=1:nmut
population(mrow(ii),mcol(ii))=abs(population(mrow(ii),mcol(ii))-
1);
% toggles bits
end
% ii
% The population is being re-evaluated for cost
cost(2:population_size,1)=...Select_Switch_Genetically(population
(2:population_size,:),Power_Demand_in_MVA,allocated_Power_i
n_MVA);
 % Sort the costs and associated parameters
[cost,ind]=sort(cost);
population=population(ind,:);
%perform statistics for a single nonaveraging run
minc(iga+1)=min(cost);
meanc(iga+1)=mean(cost);
%Stopping criteria
if iga>maxit || cost(1)<mincost
break
end
[iga cost(1)];
end
%iga
```

```
%step 6 Get Switches_State_out from binary value of population
(1) with minimum cost
selected_state = population(1,:);
Switch_Values=selected_state(1)*2^7+selected_state(2)
*2^6+selected_state(3)*2^5+selected_state(4)
*2^4+...+selected_state(5)*2^3+selected_state(6)
*2^2+selected_state(7)*2^1 + selected_state(8)*2^0;
Switches_State_out = uint8(Switch_Values);
% bug
Appliances_to_Switch = Switches_State_out;
%----------work here
k8 = 0.25; k7 = 0.18; k6 = 0.15; k5 = 0.12; k4 = 0.1; k3 = 0.1; k2 =
0.05; k1 = 0.05;
allowed_power_MVA=Power_Demand_in_MVA*(selected_state
(1)*k8+selected_state(2)*k7+selected_state(3)*k6+selected_state
(4)*k5+...selected_state(5)*k4+selected_state(6)
*k3+selected_state(7)*k2+selected_state(8)*k1);
Old_Power_OUT=
[allowed_power_MVA;allowed_power_MVA*cosPhi];
% decouple into P and Q
power = zeros(2,1, 'double');
power(1,1)=allowed_power_MVA * cosPhi;
power(2,1) = allowed_power_MVA * sinPhi;
Cmd=unit16(bitor(CONSUMER_ADDRESS,uint16
(Appliances_to_Switch)));
Cmd = double(Cmd);
Comand = [power; Cmd/1000];
if (isnan(power(1,1)) ||isnan(power(2,1)))x = 4;
end
function
cost=Select_Switch_Genetically
(Populatn,Demanded_MVA,Allocated_MVA)population_size=
size(Populatn, 1);
% no of rows
new_MVA = zeros(population_size,1);
k8 = 0.25; k7 = 0.18; k6 = 0.15; k5 = 0.12; k4 = 0.1; k3 = 0.1; k2 =
0.05; k1 = 0.05;
%new_MVA(:,1)= Demanded_MVA*(Populatn(:,8)*k8 +Populatn
(:,7)*k7 +Populatn(:,6)*k6 +Populatn(:,5)*k5 +...
%Populatn(:,4)*k4+Populatn(:,3)*k3+Populatn(:,2)*k2 +Populatn
(:,1)*k1);
new_MVA(:,1)=Demanded_MVA*(Populatn(:,1)*k8+Populatn
(:,2)*k7+Populatn(:,3)*k6+Populatn(:,4)*k5+..Populatn(:,5)
*k4+Populatn(:,6)*k3+Populatn(:,7)*k2+Populatn(:,8)*k1);
%new_MVA=sqrt(new_MVAr^2+Demanded_MWatt^2);
cost=double(abs(0.97*Allocated_MVA - new_MVA));
return;
end
```

Appendix 2

Load control algorithm on consumer premises.

```
function
[Ctrl_1,Ctrl_2,Ctrl_3,Ctrl_4,Ctrl_5,Ctrl_6,Ctrl_7,Ctrl_8,new_Cmd
] = fcn(Cmd_From_Substation, old_Cmd);
%#codegen
CONSUMER_ADDRESS = 65280;
% 0xFF00 % to be changed later
Mask = uint16(65280);
% 0xFF00
Command = uint16(Cmd_From_Substation*1000);
address = bitand(Command, Mask);
%Command = Command
% address = address
if (address ~= CONSUMER_ADDRESS)
% use the last command
Command = old_Cmd;
% read previous command from memory
else
%new_Cmd=Command;
%write new command to memory
end
 new_Cmd=Command;
% write new command to memory
%interprete the command issued in Command_From_Substation
Ctrl_1=0; Ctrl_2 = 0; Ctrl_3 = 0; Ctrl_4 = 0; Ctrl_5 = 0;
Ctrl_6 = 0; Ctrl_7 = 0; Ctrl_8 = 0;
bit = bitget(Command,1);
if (bit = 1) Ctrl_1 = 1;
% at
end
bit = bitget(Command,2);
if (bit == 1) Ctrl_2 = 1;
% at
end
bit = bitget(Command,3);
if (bit == 1)
Ctrl_3 = 1;
% at
end
bit = bitget(Command,4);
if (bit == 1) Ctrl_4 = 1;
% at
end
bit = bitget(Command,5);
if (bit == 1) Ctrl_5 = 1;
% at
end
bit = bitget(Command,6);
if (bit = 1) Ctrl_6 = 1;
% at
end
bit = bitget(Command,7);
if (bit = 1) Ctrl_7 = 1;
% at
end
bit = bitget(Command,8);
if (bit == 1) Ctrl_8 = 1;
% at
end
%display=[Ctrl_1 Ctrl_2 Ctrl_3 Ctrl_4 Ctrl_5 Ctrl_6 Ctrl_7
Ctrl_8]
new_Cmd = unit16(new_Cmd);
%Command = Command % dislay it
```

Biographies

THOMAS OLABODE ALE completed his tertiary education at the Federal University of Technology, Akure, Nigeria, with Second Class Upper Division in Electrical and Electronics Engineering in 1999. He received his Master of Engineering in Electrical and Electronics Engineering degree (Power Option) in 2003, and holds a PhD in power system engineering. Dr. Ale is a corporate member of the Nigerian Society of Engineers, and a registered member of the Council for the Regulation of Engineering in Nigeria (COREN). He is currently a lecturer at the Federal University of Technology, Akure, Nigeria. He has published papers, conference proceedings, and research findings in both undergraduate and postgraduate programs. Dr. Ale may be reached at aleto04@yahoo.com

AGBENIYI ADEBUSUYI JAMES holds a master's degree (M.Eng) in electrical power systems from the Federal University of Technology, Akure (FUTA), Nigeria. He is a registered/licensed engineer with the Council for the Regulation of Engineering in Nigeria (COREN) and a corporate member of the Nigeria Society of Engineers (NSE). Engr. Agbeniyi is currently the mechanical/autotronics unit head of the Electrical/Mechanical Department at the Obafemi Awolowo University Teaching Hospital. His field of interest is electrical power systems and automotive mechatronics. Dr. James may be reached at busuyistalking12@gmail.com

INSTRUCTIONS FOR AUTHORS: MANUSCRIPT REQUIREMENTS

The INTERNATIONAL JOURNAL OF MODERN ENGINEERING is an online/print publication designed for Engineering, Engineering Technology, and Industrial Technology professionals. All submissions to this journal, submission of manuscripts, peer-reviews of submitted documents, requested editing changes, notification of acceptance or rejection, and final publication of accepted manuscripts will be handled electronically. The only exception is the submission of separate high-quality image files that are too large to send electronically.

All manuscript submissions must be prepared in Microsoft Word (.doc or .docx) and contain all figures, images, and/or pictures embedded where you want them and appropriately captioned. Also, for all accepted manuscripts, each figure, image, or picture that was imported into your Word document must be saved individually as a **300dpi or higher JPEG (.jpg)** file and submitted separately; your manuscript and figure numbers must be used in the title of the file (e.g., **M12-S-18 Figure 4**); that means one additional file for each image imported into your manuscript. These 300dpi images do NOT need to be embedded in your manuscript. For tables or graphs created directly in Word, you do not need to submit them as separate files.

Included below is a summary of the formatting instructions. You should, however, review the sample Word document on our website for details on how to correctly format your manuscript. The editorial staff reserves the right to edit and reformat any submitted document in order to meet publication standards of the journal.

The references included in the References section of your manuscript must follow APA-formatting guidelines. In order to help you, the sample Word document also includes numerous examples of how to format a variety of scenarios. Keep in mind that an incorrectly formatted manuscript will be returned to you, a delay that may cause it (if accepted) to be moved to a subsequent issue of the journal.

1. **Word Document Page Setup**: Two columns with ¼" spacing between columns; Top of page = ¾"; Bottom of page = 1" (from the top of the footer to bottom of page); Left margin = ¾"; Right margin = ¾".

2. **Paper Title**: Centered at the top of the first page with a 22-point Times New Roman (Bold), Small-Caps font.

3. **Page Breaks**: Do not use page breaks.

4. **Body Fonts**: Use 10-point Times New Roman (TNR) for body text throughout (1/8" paragraph indention); 9-point TNR for author names/affiliations under the paper title; 16-point TNR for major section titles; 14-point TNR for minor section titles; 9-point TNR BOLD for caption titles for tables and figures; other font sizes as noted in the sample document.

5. **In-text Referencing**: List and number each reference when referring to them in the body of your document (e.g., [1]). The first entry must be [1] followed by [2], [3], etc., continuing in numerical order to the final entry in your References section. Again, see the sample Word document for specifics. Do not use the End-Page Reference utility in Microsoft Word. You must manually place references in the body of the text.

6. **Tables and Figures**: Center all tables and figures. Captions for tables must be above the table, while captions for figures are below; all captions are left-justified.

7. **Page Limit**: Manuscripts should not be more than 15 pages (single-spaced, 2-column format).

8. **Page Numbering**: Do not use page numbers.

9. **Publication Charges:** Manuscripts accepted for publication are subject to mandatory publication charges.

10. **Copyright Agreement:** Review the **copyright transfer agreement**.

11. **Submissions:** All manuscripts and associated files must be submitted electronically; the only exception would be if you wish to submit a CD with the individual files for your high-quality images, as noted above.

    MANUSCRIPTS should be submitted to Dr. Philip D. Weinsier, manuscript editor, at philipw@bgsu.edu along with a copy to editor@ijme.us.

    FILES containing your high-quality images should ONLY be submitted to philipw@bgsu.edu.

CUTTING EDGE JOURNAL OF RESEARCH AND INNOVATION IN ENGINEERING

Print ISSN: 2152-4157
Online ISSN: 2152-4165

www.ijeri.org

www.iajc.org

INTERNATIONAL JOURNAL OF ENGINEERING RESEARCH AND INNOVATION

ABOUT IJERI:

- IJERI is the second official journal of the International Association of Journals and Conferences (IAJC).
- IJERI is a high-quality, independent journal steered by a distinguished board of directors and supported by an international review board representing many well-known universities, colleges, and corporations in the U.S. and abroad.
- IJERI has an impact factor of **1.58**, placing it among an elite group of most-cited engineering journals worldwide.

OTHER IAJC JOURNALS:

- The International Journal of Modern Engineering (IJME) For more information visit www.ijme.us
- The Technology Interface International Journal (TIIJ) For more information visit www.tiij.org

IJERI SUBMISSIONS:

- Manuscripts should be sent electronically to the manuscript editor, Dr. Philip Weinsier, at philipw@bgsu.edu.

  For submission guidelines visit www.ijeri.org/submissions

TO JOIN THE REVIEW BOARD:

- Contact the chair of the International Review Board, Dr. Philip Weinsier, at philipw@bgsu.edu.

  For more information visit www.ijeri.org/editorial

INDEXING ORGANIZATIONS:

- IJERI is currently indexed by 16 agencies. For a complete listing, please visit us at www.ijeri.org.

Contact us:

Mark Rajai, Ph.D.

Editor-in-Chief
California State University-Northridge
College of Engineering and Computer Science
Room: JD 4510
Northridge, CA 91330
Office: (818) 677-5003
Email: mrajai@csun.edu

www.tiij.org

www.ijme.us

THE LEADING JOURNAL OF ENGINEERING, APPLIED SCIENCE AND TECHNOLOGY

The latest impact factor (IF) calculation (Google Scholar method) for IJME of 3.0 moves it even higher in its march towards the top 10 engineering journals.

IJME IS THE OFFICAL AND FLAGSHIP JOURNAL OF THE INTERNATIONAL ASSOCATION OF JOURNALS AND CONFERENCE (IAJC)
www.iajc.org

The International Journal of Modern Engineering (IJME) is a highly-selective, peer-reviewed journal covering topics that appeal to a broad readership of various branches of engineering and related technologies. IJME is steered by the IAJC distinguished board of directors and is supported by an international review board consisting of prominent individuals representing many well-known universities, colleges, and corporations in the United States and abroad.

IJME Contact Information

General questions or inquiries about sponsorship of the journal should be directed to:

Mark Rajai, Ph.D.
Editor-in-Chief
Office: (818) 677-5003
Email: editor@ijme.us
Department of Manufacturing Systems Engineering & Management
California State University-Northridge
18111 Nordhoff St.
Northridge, CA 91330